



Delft University of Technology

## Smart Electrosurgical Knife For Real-Time Intraoperative Tissue Detection

Azizian Amiri, S.

**DOI**

[10.4233/uuid:f45b4f87-cbcc-4de5-b2a8-115777e4df9a](https://doi.org/10.4233/uuid:f45b4f87-cbcc-4de5-b2a8-115777e4df9a)

**Publication date**

2025

**Document Version**

Final published version

**Citation (APA)**

Azizian Amiri, S. (2025). *Smart Electrosurgical Knife For Real-Time Intraoperative Tissue Detection*. [Dissertation (TU Delft), Delft University of Technology]. <https://doi.org/10.4233/uuid:f45b4f87-cbcc-4de5-b2a8-115777e4df9a>

**Important note**

To cite this publication, please use the final published version (if applicable).  
Please check the document version above.

**Copyright**

Other than for strictly personal use, it is not permitted to download, forward or distribute the text or part of it, without the consent of the author(s) and/or copyright holder(s), unless the work is under an open content license such as Creative Commons.

**Takedown policy**

Please contact us and provide details if you believe this document breaches copyrights.  
We will remove access to the work immediately and investigate your claim.

# Smart Electrosurgical Knife

## For Real-Time Intraoperative Tissue Detection

Sara Azizian Amiri

# Smart Electrosurgical Knife

For Real-Time Intraoperative Tissue Detection



# **Smart Electrosurgical Knife**

## For Real-Time Intraoperative Tissue Detection

### **Proefschrift**

ter verkrijging van de graad van doctor  
aan de Technische Universiteit Delft,  
op gezag van de Rector Magnificus, Prof.dr.ir. T.H.J.J. van der Hagen,  
voorzitter van het College voor Promoties,  
in het openbaar te verdedigen op  
Dinsdag 27 mei 2025 om 12:30 uur

door

**Sara AZIZIAN AMIRI**

Master of Science in Biomedical Engineering,  
Tehran Polytechnic, Iran,  
geboren te Teheran, Iran.

Dit proefschrift is goedgekeurd door de promotoren.

Samenstelling promotiecommissie bestaat uit:

Rector magnificus,	Voorzitter
Prof. dr. J. Dankelman	Technische Universiteit Delft, promotor
Prof. dr. B. H. W. Hendriks,	Technische Universiteit Delft, promotor

*Onafhankelijke leden:*

Prof. dr. J. J. van den Doppelsteen	Technische Universiteit Delft
Prof. dr. T. J. M. Ruers	Nederlands Kanker Instituut
Dr. N. Bhattacharya	Technische Universiteit Delft
Prof. dr. S. Manohar	Universiteit Twente
Prof. dr. T. G. J. M. van Leeuwen	Amsterdam Universitair Medische Centra

*Reserve lid:*

Prof. dr. ir. P. Breedveld	Technische Universiteit Delft
----------------------------	-------------------------------



The research leading to these results has received funding from The Netherlands Organization for Health Research and Development (ZonMw) under Grant no. [104006002]

*Keywords:* Smart electrosurgical knife, margin assessment, diffuse reflectance spectroscopy, real-time tissue detection, tissue optics

*Printed by:* Gildeprint.

Copyright © 2024 by S. Azizian Amiri

ISBN 978-94-6518-056-4

An electronic version of this dissertation is available at <http://repository.tudelft.nl/>

*To the cherished memory of Parisa Joon and all those who bravely fought and lost their lives to cancer. Your strength, courage, and legacy remain in our hearts, inspiring us to pursue a cure and carry the light of hope into the future.*



# Summary

Breast cancer is the most common cancer in women globally, and breast-conserving surgery (BCS), or lumpectomy, is the primary treatment for early-stage patients. However, achieving clear margins—when the tumor is fully removed—remains a challenge, often requiring re-excision surgeries or additional treatments. Surgeons rely on preoperative images and palpation to estimate the tumor's borders, but these methods are not always accurate, with incomplete resections occurring in 10% to 50% of cases.

In this thesis, we explore the integration of Diffuse Reflectance Spectroscopy (DRS), an optical tissue-sensing technology, into an electrosurgical knife to create a smart electrosurgical knife that addresses this issue. DRS helps to distinguish between cancerous and healthy tissues in real-time by analyzing optical properties, offering a potential solution to ensure clear margins during surgery. Researchers have shown that DRS can differentiate tissues based on their unique optical fingerprints, such as the Fat/Water-ratio, which helps determine tumor borders.

We began by identifying the main challenges in combining DRS with an electrosurgical knife. Initial tests on porcine tissue examined the impact of electrosurgery on the optical fibers and their ability to distinguish between tissues (Chapter 2). Microscopic analyses revealed changes in the optical fibers and the formation of debris during electrosurgery, which could interfere with accurate tissue sensing. The chapter concludes with an assessment of the fibers' performance in delivering light and capturing DRS readouts before and after electrosurgery, highlighting the complexities of using this technology in a surgical environment and the need for design modifications to protect the optical fibers from the effects of electrosurgery.

To further investigate design iterations and verify the technology, we describe in Chapter 3 the developed tissue-mimicking phantom materials that replicate the optical properties of human breast tissue. Since breast tissue consists of multiple layers with varying optical characteristics, simulating these complexities was crucial to test the smart electrosurgical knife. These phantom materials mimic both healthy and cancerous tissues, providing a controlled environment to evaluate the knife's ability to differentiate between

tissue types. The results from this chapter helped refine both the design and testing methodology of the knife.

In Chapter 4, we focus on the continued development of the smart electrosurgical knife to ensure it can withstand the demands of prolonged surgery. Several designs were tested on porcine tissue to identify the most effective configuration for integrating DRS. These designs were evaluated for their ability to maintain accurate DRS readings while performing electrosurgery, which involves high temperatures and tissue coagulation. Further experiments using tissue-mimicking materials demonstrated the knife's ability to identify distinct tissue layers in real-time during electrosurgery.

In Chapter 5, we continued to enhance the design process by incorporating feedback from clinicians. In the first part, the best-performing design from previous experiments was refined based on suggestions from surgeons who tested the device. Various design concepts were produced to optimize the knife's electrosurgical and cutting performance while ensuring the integration of DRS technology. In the second part, the knife's performance was evaluated during a simulated lumpectomy on a tumor-containing phantom. Surgeons performed the surgery four times—twice with a traditional electrosurgical knife relying on preoperative images, and twice with the smart electrosurgical knife providing real-time tissue sensing. The results showed that using the smart knife led to better surgical outcomes, highlighting its potential as an intraoperative tool for margin assessment and its promise for improving the precision and safety of breast cancer surgeries.

In Chapter 6, we focus on simplifying the technology for broader surgical use. We proposed using LEDs and photodetectors instead of wide-band light sources and spectrometers, creating a compact, console-free design. An electronic board was developed to identify optimal wavelengths for breast tissue, and a proof-of-concept showed that this system could distinguish tissue-mimicking materials. We envision a handheld device integrating DRS into the electrosurgical knife, removing the need for bulky equipment and paving the way for a more accessible, user-friendly tool in clinical settings.

Finally, Chapter 7 reviews the key findings from the research and presents concluding remarks. The thesis demonstrates the potential of integrating DRS into surgical tools for real-time tissue identification, offering a valuable solution to the problem of incomplete tumor resection.

# Samenvatting

Borstkanker is wereldwijd de meest voorkomende vorm van kanker bij vrouwen, en borstsparende chirurgie (BCS), of lumpectomie, is de primaire behandeling voor patiënten in een vroeg stadium. Het bereiken van schone marges—waarbij de tumor volledig wordt verwijderd—blijft echter een uitdaging, wat vaak leidt tot heroperaties of aanvullende behandelingen. Chirurgen vertrouwen op preoperatieve beelden en palpatie om de randen van de tumor te schatten, maar deze methoden zijn niet altijd nauwkeurig, met onvolledige resecties in 10% tot 50% van de gevallen.

In dit proefschrift onderzoeken we de integratie van Diffuse Reflectance Spectroscopy (DRS), een optische weefselherkenningstechnologie, in een elektrochirurgisch mes om een slim elektrochirurgisch mes te creëren dat dit probleem aanpakt. DRS helpt om in real-time onderscheid te maken tussen kankerweefsel en gezond weefsel door de optische eigenschappen van weefsels te analyseren, en biedt zo een potentiële oplossing om schone marges tijdens operaties te waarborgen. Onderzoekers hebben aangetoond dat DRS weefsels kan onderscheiden op basis van hun unieke optische kenmerken, zoals de vet/water-verhouding, die helpt bij het bepalen van de tumorgrenzen.

We begonnen met het identificeren van de belangrijkste uitdagingen bij het combineren van DRS met een elektrochirurgisch mes. Eerste tests op varkensweefsel lieten de impact van elektrochirurgie op de optische fibers zien en hun vermogen om onderscheid te maken tussen weefsels (Hoofdstuk 2). Microscopische analyses onthulden veranderingen in de optische fibers en de vorming van debris tijdens elektrochirurgie, wat de nauwkeurigheid van de weefseldetectie kan verstoren. Het hoofdstuk sluit af met een beoordeling van de prestaties van de fibers bij het leveren van licht en het vastleggen van DRS-metingen vóór en na de elektrochirurgie, waarbij de complexiteit van het gebruik van deze technologie in een chirurgische omgeving en de noodzaak van ontwerpaanpassingen om de optische fibers te beschermen tegen de effecten van elektrochirurgie wordt benadrukt.

Om verdere ontwerpherzieningen te onderzoeken en de technologie te verifiëren, hebben we in Hoofdstuk 3 weefsel-nabootsende fantoommaterialen ontwikkeld die de

optische eigenschappen van menselijk borstweefsel nabootsen. Aangezien borstweefsel uit meerdere lagen met verschillende optische eigenschappen bestaat, was het cruciaal om deze complexiteit te simuleren om het slimme elektrochirurgische mes te testen. Deze fantoommaterialen bootsen zowel gezond als kwaadaardig weefsel na en bieden een gecontroleerde omgeving om het vermogen van het mes om tussen weefseltypen te onderscheiden, te evalueren. De resultaten uit dit hoofdstuk hielpen bij het verfijnen van zowel het ontwerp als de testmethodologie van het mes.

In Hoofdstuk 4 richten we ons op de verdere ontwikkeling van het slimme elektrochirurgische mes om ervoor te zorgen dat het bestand is tegen de eisen van langdurige chirurgie. Verschillende ontwerpen werden getest op varkensweefsel om de meest effectieve configuratie voor het integreren van DRS te identificeren. Deze ontwerpen werden geëvalueerd op hun vermogen om nauwkeurige DRS-metingen te behouden tijdens het uitvoeren van elektrochirurgie, waarbij hoge temperaturen en weefselcoagulatie betrokken zijn. Verdere experimenten met weefsel-nabootsende materialen toonden aan dat het mes in staat is om in real-time verschillende weefsellagen te identificeren.

We hebben in Hoofdstuk 5 het ontwerp verder verbeterd door feedback van clinici te integreren. In het eerste deel werd het best presterende ontwerp uit eerdere experimenten verfijnd op basis van suggesties van chirurgen die het apparaat testten. Verschillende ontwerpconcepten werden geproduceerd om de elektrochirurgische en snijprestaties van het mes te optimaliseren, terwijl de integratie van DRS-technologie werd gewaarborgd. In het tweede deel werd de prestatie van het mes geëvalueerd tijdens een gesimuleerde lumpectomie op een fataal met een tumor. Chirurgen voerden de operatie vier keer uit—twee keer met een traditioneel elektrochirurgisch mes met alleen preoperatieve beelden en twee keer met het slimme elektrochirurgische mes dat real-time weefseldetectie biedt. De resultaten toonden aan dat het gebruik van het slimme mes leidde tot betere chirurgische uitkomsten, hetgeen het potentieel van dit intra-operatief instrument benadrukt voor margebeoordeling dat kan leiden tot verbetering van de precisie en veiligheid van borstkankeroperaties.

In Hoofdstuk 6 richten we ons op het vereenvoudigen van de technologie voor bredere chirurgische toepassing. We stelden voor om LED's en fotodetectoren te gebruiken in plaats van breedbandlichtbronnen en spectrometers, wat een compact, consolevrij ontwerp opleverde. Een elektronisch bord werd ontwikkeld om de optimale

---

golfengten voor borstweefsel te identificeren, en een proof-of-concept toonde aan dat dit systeem weefsel-nabootsende materialen kan onderscheiden. We voorzien een handzaam apparaat dat DRS in het elektrochirurgisch mes integreert, waardoor omvangrijke apparatuur overbodig wordt en de weg wordt vrijgemaakt voor een toegankelijker en gebruiksvriendelijker instrument in de klinische setting.

Tot slot geeft Hoofdstuk 7 een overzicht van de belangrijkste bevindingen van het onderzoek en worden afsluitende opmerkingen gepresenteerd. Het proefschrift toont het potentieel aan van het integreren van DRS in chirurgische instrumenten voor real-time weefselidentificatie, wat een waardevolle oplossing biedt voor het probleem van onvolledige tumorresectie.



# Content

<b>Summary .....</b>	<b>vii</b>
<b>Samenvatting .....</b>	<b>ix</b>
<b>1 Introduction .....</b>	<b>17</b>
1.1 Background .....	18
1.2 Problem definition and thesis objectives .....	18
1.3 Thesis outline .....	20
Bibliography.....	23
<b>2 Electrosurgery impact on debris formation and tissue read-out .....</b>	<b>25</b>
2.1 Introduction .....	26
2.2 Materials and Methods.....	27
2.2.1 Sample preparation .....	27
2.2.2 Debris characterization .....	29
2.2.3 Light intensity analysis.....	30
2.2.4 DRS signal deterioration .....	31
2.2.5 Statistical analysis.....	32
2.3 Results .....	32
2.3.1 Debris characterization .....	32
2.3.2 Light intensity analysis.....	35
2.3.3 DRS signal deterioration .....	35
2.4 Discussion .....	37
2.4.1 Debris Characterization .....	37
2.4.2 DRS signal deterioration .....	39
2.5 Conclusion .....	40
Bibliography.....	42

<b>3 Breast phantom.....</b>	<b>45</b>
3.1 Introduction .....	46
3.1.1 Diffuse reflectance spectroscopy.....	46
3.1.2 Breast phantoms.....	47
3.1.3 Fat-water based phantoms for medical optics: mini-review .....	50
3.2 Materials and Methods .....	53
3.2.1 Phantom materials preparation .....	53
3.2.2 DRS measurements .....	54
3.2.3 Electrosurgery.....	58
3.2.4 Stability over time.....	58
3.2.5 Breast phantom preparation.....	58
3.2.6 X-Ray validation.....	59
3.2.7 Statistical analysis .....	59
3.3 results.....	59
3.3.1 DRS measurements .....	60
3.3.2 Electrosurgery.....	65
3.3.3 Stability over time.....	66
3.3.4 Breast phantom production.....	67
3.3.5 X-ray image of the phantoms .....	69
3.4 Discussion.....	70
3.5 Conclusions .....	78
Bibliography .....	79
<b>4 Smart electrosurgical knife's functionality during electrosurgery.....</b>	<b>87</b>
4.1 Introduction .....	88
4.2 Materials and Methods .....	90
4.2.1 Characterization of heat development during electrosurgery .....	90
4.2.2 Heat and debris resistant design of the smart electrosurgical knife.....	91
4.2.3 Experimental setup .....	92

---

4.2.4 Performance assessment .....	95
4.2.5 Statistical analysis.....	100
4.3 Results .....	100
4.3.1 Characterization of heat development during electrosurgery .....	100
4.3.2 Performance assessment .....	101
4.4 Discussion .....	109
4.5 Conclusions.....	114
Bibliography.....	116
<b>5 Pre-Clinical evaluation of Smart electrosurgical knife .....</b>	<b>119</b>
5.1 Introduction .....	120
5.2 Materials and Methods.....	122
5.2.1 Part 1: Evaluating the usability of the smart electrosurgical knife by surgeons .....	122
5.2.2 Tissue sparing surgery on the phantom .....	124
5.3 Results .....	128
5.3.1 Part 1: Evaluating the usability of the smart electrosurgical knife by surgeons .....	128
5.3.1.2 .....	128
5.3.2 Part 2: Tissue sparing surgery on the phantom .....	130
5.3.2.1 <i>Phantom production</i> .....	130
5.4 Discussion .....	135
5.4 Conclusions.....	140
Bibliography.....	141
<b>6 Multi-wavelength probe for fat content detection: Toward LED-based real-time tissue diagnosis .....</b>	<b>143</b>
6.1 Introduction .....	144
6.2 Materials and Methods.....	145
6.2.1 Device design .....	145
6.2.2 Phantom production.....	149

6.2.3 DRS measurement .....	150
6.2.4 Experimental setup .....	151
6.2.3 Data analysis .....	152
6.3 Results .....	153
6.3.1 DRS measurement .....	153
6.3.2 Measurement using the device .....	153
6.5 Conclusions .....	160
Bibliography .....	161
<b>7 Concluding remarks .....</b>	<b>163</b>
7.1 Main findings of this thesis .....	164
7.2 Concluding remarks and future directions: .....	169
7.3 Final words .....	179
Bibliography .....	180
<b>Acknowledgements .....</b>	<b>183</b>
<b>List of publications .....</b>	<b>189</b>
A. Peer-reviewed journal publications .....	189
B. Selected conference presentations .....	190
<b>Curriculum Vitae .....</b>	<b>193</b>

# 1

## Introduction

## 1.1 Background

"It happens without any warning, like a bomb with no timer, deafening you with shock and disbelief, and shattering your entire world when you hear the words, 'You have cancer,'" said Nil, a nurse and mother of three, in 2013, at the age of 43, when she was diagnosed with breast cancer [1]. The Big 'C' invades our lives, or the lives of our loved ones, without any heads-up, like being bombarded out of nowhere. We don't know why it happens, when it started, or how. Some choose to fight back, while others might decide to spend the time they have left freely. Some become survivors and completely recover, some do not, and some must manage chronic aspects of the illness for the rest of their lives.

Modern medicine is dedicating immense time and resources to understand and treat this disease of the century and to save humanity. Over the past 100 years, clinicians and pharmacists have made priceless discoveries in cancer treatment. However, advancements in technical science and engineering have demonstrated that non-clinical professionals, such as engineers and technical scientists, can also contribute significantly.

In the battlefield against cancer, we must add whatever we can to our arsenal. Our opponent is not sitting idle; it is evolving, bringing more and more surprises. Now, more than ever, clinicians, scientists, and engineers must work hand in hand to defeat this enemy of humanity.

As an engineer, I had the opportunity to work on an interdisciplinary project, developing a device that can impact the lives of those dealing with cancer. Together, we can turn the tide and one day use our collective knowledge to transform cancer from a deadly foe into a manageable condition.

## 1.2 Problem definition and thesis objectives

The "Sensing in Surgery" project began with the idea of using tissue sensing technology to prevent incomplete tumor resection during cancer surgery.

For this thesis, the focus is on breast cancer. In the context of this thesis, *breast cancer surgery* refers to "lumpectomy" or "Breast Conserving Surgery" (BCS). This procedure is the main surgical option for treatment of early-stage breast cancer, where removing the tumor is preferred over removing the entire breast. The goal is to extract the tumor while minimizing damage to healthy tissue, preserving the breast's shape, and aiming for better cosmetic outcomes [2].

During a lumpectomy, the surgeon uses an electrosurgical knife to extract the tumor. Surgeons are provided with pre-operative images showing the approximate size, shape, and location of the malignant tissue. Additionally, the surgeon may use a device that tracks the tumor's location, often based on technologies like magnetic seed tracking inserted into the tumor before surgery [3].

It might sound straightforward to remove the tumor, but it is far from easy. In the surgical wound, distinguishing between malignant and healthy tissue with the naked eye is nearly impossible. Tumors are irregular, with many sharp edges penetrating the surrounding tissue. This makes detecting tumor borders challenging while striving to preserve as much healthy tissue as possible [4-6].

Surgeons rely on pre-operative images and palpation techniques to guess the tumor's shape and location, as tumors and healthy tissue can have different stiffness. Despite their best efforts, ***incomplete tumor resection***, or positive margins, occurs in 10% to 50% of these surgeries. This often necessitates additional surgeries or more aggressive therapies [7-10].

Given these challenges, a tissue sensing technology would be immensely beneficial. Such a technique could provide real-time feedback during surgery, helping the surgeon distinguish between healthy and cancerous tissue and precisely locate the tumor border, ensuring a clear resection and a negative margin.

The ***tissue sensing technology*** used in this thesis is called Diffuse Reflectance Spectroscopy (DRS), an optical technique. DRS is a spectroscopic system that uses light sources and spectrometers to emit light to the tissue and collect it through optical fibers. The interaction between light and tissue helps to measure the concentration of different chromophores and to identify tissue types. DRS has shown potential in distinguishing cancerous from benign tissue in various organs [11-18].

This project's primary idea was to incorporate DRS into the workflow of a lumpectomy by integrating it into an electrosurgical knife, and by doing so creating a **Smart Electrosurgical Knife** with tissue recognition capabilities. Over the past four years, through collaboration with surgeons, I have realized that such a tool could be a "Holy Grail" in surgery, addressing the significant challenge of complete tumor resection.

However, integrating DRS into an electrosurgical knife and developing it for clinical use comes with many challenges, which have been the focus of the work in this thesis.

While Diffuse Reflectance Spectroscopy (DRS) is a noninvasive technique to measure the spectral response of tissue, it requires the tip of the optical fibers to be in direct contact with the tissue. However, positioning the optical fibers close to the blade of the electrosurgical knife presents significant challenges, the most critical being the heat produced during electrosurgery and the occlusion of the optical fibers by tissue debris, which can interfere with the DRS system and its performance.

The overarching goal of this thesis is **to bring the smart electrosurgical knife as close to clinical use as possible**. To achieve this, the research objectives are defined as follows:

1. **Identify Challenges:** Determine the obstacles associated with combining electrosurgery and optical measurement, particularly addressing the heat interference with DRS.
2. **Develop Test Platforms:** Create platforms for investigating and testing the smart electrosurgical knife during its development.
3. **Design and Develop:** Engineer a smart electrosurgical knife that overcomes the identified challenges, ensuring reliable performance in clinical settings.
4. **Clinician Insights:** Incorporate feedback and insights from clinicians to refine the design and functionality of the smart electrosurgical knife.
5. **Performance Testing:** Evaluate the performance of the smart electrosurgical knife in simulated operations to ensure its efficacy and safety.
6. **Simplify Design:** Minimize and simplify the design and application of the smart electrosurgical knife to make it user-friendly and practical for clinical use.

These objectives aim to address the technical hurdles and pave the way for the smart electrosurgical knife to become a transformative tool in cancer surgery, enhancing precision and patient outcomes.

### 1.3 Thesis outline

Six chapters follow this introductory chapter, covering the research objectives outlined above.

**Chapter 2** addresses the first objective: identifying challenges. We began by designing a prototype of the smart electrosurgical knife, integrating the optical fibers of the DRS system at the tip of a blade-shaped electrode of a common electrosurgical knife.

We tested this design on porcine tissue to observe the effects of electrosurgery on the optical fibers and tissue readouts. Microscopic investigations were conducted to identify changes in the optical fibers and the nature of debris formed after electrosurgery. We also evaluated the performance of the optical fibers in delivering light and obtaining DRS tissue readouts before and after electrosurgery.

**Chapter 3** explores the development of tissue-mimicking phantom materials that simulate the composition and optical properties of human breast tissues. Human breast tissue consists of various layers, each with unique optical properties. The complex structure of cancerous growths includes tissues with diverse optical properties. These tissue-mimicking materials serve as platforms to further investigate the smart electrosurgical knife's performance in identifying these differences in complex structures, such as the wound site in lumpectomies.

**Chapter 4** focuses on the design and development of smart electrosurgical knives capable of withstanding the harsh conditions of prolonged electrosurgery. Multiple designs were created and tested on porcine tissue to identify the best-performing design. This design was then further investigated on both porcine tissue and tissue-mimicking materials. DRS measurements with different electrosurgical settings were carried out before and after prolonged electrosurgery to showcase the knife's performance in accurately identifying tissue types. Finally, we demonstrated the applicability of this design in real-time tissue identification on layered tissue-mimicking phantoms, each layer having unique compositions and optical properties.

**Chapter 5** incorporates clinicians' insights into the knife's design in two parts. In Part 1, following the identification of the best design from the previous chapter, different design concepts, based on this design, were introduced and produced. We sought surgeons' opinions on how these design incorporations affected the knife's electrosurgical and cutting performance. In Part 2, we tested the smart electrosurgical knife's performance by having a surgeon perform a lumpectomy on a tumor-containing phantom. The surgeon conducted the surgery four times—twice using a normal electrosurgical knife relying on pre-operative images, and twice using the smart electrosurgical knife with tissue guidance. This chapter investigates the potential of the smart electrosurgical knife as an intraoperative margin assessment technique and envisions an improved design incorporating clinician feedback.

**Chapter 6** takes the first step towards producing a handheld device that simplifies the DRS console for integration into the smart electrosurgical knife, aiming for a console-free design. We proposed using LEDs and photodetectors instead of wide-band light sources and spectrometers. First, an electronic board was produced for this purpose, and the desired wavelengths for breast tissue identification were investigated. We conducted a proof of concept for a device that can identify tissue-mimicking materials with different compositions (varying amounts of fat and water) based on this design. Finally, we envisioned a smart electrosurgical knife design that incorporates this simplified DRS system, aiming to streamline the device's application.

**Chapter 7** reviews the main findings of this thesis, presents concluding remarks, and provides an outlook on future research directions.

## Bibliography

- [1] N. S. Mapi, "A Nurse's Journey with Cancer," *Asia-Pacific Journal of Oncology Nursing*, vol. 5, no. 3, pp. 290-295, 2018.
- [2] C. Chiappa *et al.*, "Surgical margins in breast conservation," *International Journal of Surgery*, vol. 11, pp. S69-S72, 2013.
- [3] R. J. Gray *et al.*, "Intraoperative margin management in breast-conserving surgery: a systematic review of the literature," *Annals of surgical oncology*, vol. 25, no. 1, pp. 18-27, 2018.
- [4] H. M. Kuerer *et al.*, "DCIS margins and breast conservation: MD Anderson Cancer Center multidisciplinary practice guidelines and outcomes," *Journal of Cancer*, vol. 8, no. 14, pp. 2653-2662, 2017.
- [5] B. L. Murphy *et al.*, "Factors associated with positive margins in women undergoing breast conservation surgery," in *Mayo Clinic Proceedings*, Year, pp. 429-435.
- [6] L. A. Newman, and J. M. Bensenhaver, *Ductal carcinoma in situ and microinvasive/borderline breast cancer*, p.^pp. 171: Springer, 2015.
- [7] E. Sadot *et al.*, "Resection margin and survival in 2368 patients undergoing hepatic resection for metastatic colorectal cancer: surgical technique or biologic surrogate?," *Annals of surgery*, vol. 262, no. 3, pp. 476, 2015.
- [8] C. Reyna, and S. M. DeSnyder, "Intraoperative margin assessment in breast cancer management," *Surgical Oncology Clinics*, vol. 27, no. 1, pp. 155-165, 2018.
- [9] R. Jeevan *et al.*, "Reoperation rates after breast conserving surgery for breast cancer among women in England: retrospective study of hospital episode statistics," *Bmj*, vol. 345, pp. 1-9, 2012.
- [10] J. Landercasper *et al.*, "Reasons for re-excision after lumpectomy for breast cancer: insight from the American Society of Breast Surgeons Mastery SM database," *Annals of surgical oncology*, vol. 21, no. 10, pp. 3185-3191, 2014.
- [11] R. Nachabé *et al.*, "Diagnosis of breast cancer using diffuse optical spectroscopy from 500 to 1600 nm: comparison of classification methods," *Journal of Biomedical Optics*, vol. 16, no. 8, pp. 087010-087010-12, 2011.
- [12] T. M. Bydlon *et al.*, "Chromophore based analyses of steady-state diffuse reflectance spectroscopy: current status and perspectives for clinical adoption," *Journal of biophotonics*, vol. 8, no. 1-2, pp. 9-24, 2015.
- [13] A. Keller *et al.*, "Diffuse reflectance spectroscopy of human liver tumor specimens-towards a tissue differentiating optical biopsy needle using light emitting diodes," *Biomedical Optics Express*, vol. 9, no. 3, pp. 1069-1081, 2018.
- [14] J. W. Sliethoff *et al.*, "In vivo characterization of colorectal metastases in human liver using diffuse reflectance spectroscopy: toward guidance in oncological procedures," *Journal of biomedical optics*, vol. 21, no. 9, pp. 097004, 2016.
- [15] J. W. Sliethoff *et al.*, "Spectral sensing for tissue diagnosis during lung biopsy procedures: The importance of an adequate internal reference and real-time feedback," *Lung Cancer*, vol. 98, pp. 62-68, 2016.
- [16] M. S. Nogueira *et al.*, "Evaluation of wavelength ranges and tissue depth probed by diffuse reflectance spectroscopy for colorectal cancer detection," *Scientific Reports*, vol. 11, no. 1, pp. 1-17, 2021.

- [17] G. Einstein *et al.*, “Diffuse reflectance spectroscopy for monitoring physiological and morphological changes in oral cancer,” *Optik*, vol. 127, no. 3, pp. 1479-1485, 2016.
- [18] V. G. Prabitha *et al.*, “Detection of cervical lesions by multivariate analysis of diffuse reflectance spectra: a clinical study,” *Lasers in medical science*, vol. 31, no. 1, pp. 67-75, 2016.

# 2

## Electrosurgery impact on debris formation and tissue read-out

Using an intraoperative margin assessment technique during Breast-Conserving Surgery (BCS) helps surgeons to decrease the risk of positive margin occurrence. Diffuse Reflectance Spectroscopy (DRS) has the potential to discriminate healthy breast tissue from cancerous tissue. We investigated the performance of an electrosurgical knife integrated with a DRS on porcine muscle and adipose tissue. Characterizing of the formed debris on the optical fibers after electrosurgery for a short duration revealed that the contamination is mostly burned tissue. Even with contaminated optical fibers after a short session of electrosurgery, both tissues could still be discriminated with DRS based on F/W-ratio . Therefore, the electrosurgical knife integrated with DRS may be a promising technology to provide the surgeon with real-time guidance during BCS.

Published as:

Sara Azizian Amiri, Carlijn M. Van Gent, Jenny Dankelman, Benno H. W. Hendriks, Intraoperative tumor margin assessment using diffuse reflectance spectroscopy: the effect of electrosurgery on tissue discrimination using ex vivo animal tissue models, *Biomedical optics express*, 2020.

## 2.1 Introduction

Breast cancer is the most common cancer among women worldwide and the incidence keeps increasing [1]. The standard surgical treatment for early-stage breast cancer patients is breast-conserving surgery (BCS), in which the surgeon aims to remove the tumor while maintaining the natural shape of the breast as much as possible [2]. It has been shown that lack of direct view over the surgical site or surgeon's failure to determine the exact position of the tumor based on preoperative images may lead to incomplete resection of the tumor and incidence of positive margin[3]. Positive margins occur when the excised tumor is not surrounded by at least 2 mm of healthy tissue. The incidence of positive margin during tumor surgery is a widespread problem in clinical practice, but no standard solution has been developed yet [4]. In the case of positive margin detection, re-excision surgery or extra radiation therapy and chemotherapy are required [5-7]. Based on the literature, the occurrence rate for re-excision surgery ranges from less than 10% to around 50% [8].

While positive margin incidence can cause difficulties for patients and hospitals, pre-operative localization of breast lesions, such as needle localization, intraoperative ultrasound, radio-guided surgery, and also intraoperative assessments techniques, such as gross assessment, specimen radiograph, frozen section, and cavity shave margins, seem to be promising techniques to overcome these undesired outcomes [8]. However, all of these techniques have their limitations. For instance, needle localization could be accompanied by affecting incision location, poor cosmetic results, and could be more time consuming while causing more discomfort to the patient [8, 9]. Intraoperative ultrasound is an operator-dependent technique requiring extra markers for lesions such as DCIS (Ductal Carcinoma In Situ) [8-10]. In addition to the limitation in detecting small, noncalcified lesions during radio-guided surgery and seed localization, the need to onsite nuclear support is associated with consuming more time, costs, and specialist workforce, which is not possible for many facilities [8, 11]. Furthermore, the currently available intraoperative margin assessment techniques are either not completely reliable in detecting small tumors and DCIS, or can lead to the removal of excess healthy tissue, resulting in undesired cosmetic outputs [8, 9]. While applying these techniques decreases the occurrence rate of positive margin during BSC, the occurrence rate remains yet high. Even after the use of the most promising technique still 20% of patients need to go under re-excision surgery, showing that this problem remains unsolved up to now. It seems that

---

for overcoming this challenge emerging technologies need to result in higher diagnostic accuracy in a more cost and time-effective way [12-15].

Recently, researchers proved that Diffuse Reflectance Spectroscopy (DRS) has the potential to be used as a tumor margin assessment technique [12, 13, 16-25]. Each tissue has its own special intrinsic light absorption and scattering for specific wavelengths which are known as “optical fingerprint”. Using DRS in the 400-1600 nm spectral range, De Boer *et al.* showed the Fat/Water-ratio (F/W-ratio) is a determinative factor to distinguish malignant tissue from healthy tissue and to determine the exact border of the tumor [16].

Electrosurgery is mostly used during breast-conserving surgery (BCS). With electrosurgery, a high-frequency alternating electrical current is used to cut or coagulate tissue [26]. During this process, high-temperature heat is produced that may cause collateral tissue damage and histological change. These changes can increase the scattering, decrease the depth of photon penetration and alter its optical properties [26-29]. However, recently, Adank *et al.* showed that the DRS system is capable to distinguish muscle tissue from adipose tissue even after cutting or coagulating both tissues using an electrosurgical knife [3]. Based on these results, integrating the DRS system into the electrosurgical knife seems to be a promising approach to provide the surgeon with real-time oncological guidance during cancer surgery. Despite tissue altering during electrosurgery, tissue debris formation is another undesired factor that may affect the DRS measurements. Eschar formation on the electrode of the electrosurgical knife is the most frequent happening, an unwanted event during electrosurgery [26]. Adank *et al.* also mentioned that debris adhering to the optical fibers of the DRS system integrated into the active electrode of an electrosurgical knife is suspected to deteriorate the DRS signal by altering the light behavior and its optical properties.

Therefore, in this research, the characteristics of debris attached to the optical fibers integrated into the electrosurgical knife are investigated, as well as the effect of the type of debris on the DRS signal deterioration and the F/W-ratio.

## 2.2 Materials and Methods

### 2.2.1 Sample preparation

To integrate the electrosurgical knife and the DRS system, disposable active blade shape electrodes (Hangzhou Valued Med Tech Co., China), stainless steel tubes (with outer Ø 500 µm and inner Ø 400 µm) and acrylate coated optical fibers (Ø 240 µm) were

used. The stainless steel tubes with a length of 1cm have been welded to the sides of active electrodes as shown in Figure 2.1(A), using a laser welding machine. Optical fibers were polished and cleaned to smooth the surface and avoid any roughness. Optical fibers, one connected to the halogen light-source (Avantes, The Netherlands) and one collecting the diffusively reflected light at the surface of the tissue connected to the spectrometer, were placed inside the welded metallic tubes at a 3 mm distance from the center of the emitting fiber to the center of the collecting fiber. Then, the active electrode was placed on the electrosurgical knife.

The optical fibers were connected to a Philips custom-designed diffused reflectance spectroscopy setup (Philips Research, Eindhoven) consisting of a halogen broadband light source (Avantes, The Netherlands) and spectrometers including one spectrometer designated to collect the light in the 400-1000 nm spectral range (Maya2000 Pro, Ocean Optics, USA), and one spectrometer that collects light in the 900-1700 nm spectral range (NIRQuest 512, Ocean Optics, USA). The design and application of the diffused reflectance spectroscopy setup have been described in more detail in previous publications [3, 20, 30]. The measured spectra were used as the input for a Philips custom-developed software. The software uses a nonlinear Levenberg-Marquardt inversion algorithm to fit a curve on the measured spectrum and extract the concentration of the chromophore from the fitted data [20].

Before starting the DRS measurements, the system is calibrated to minimize the influence of the ambient light and correcting the system response by placing the tip of the optical fibers at a fixed distance of 2 mm on top of the white reflectance standard (WS-1-SL, Labsphere Inc., USA). Subsequently, the spectral response of white reference was measured, followed by a background measurement. The DRS system and calibration process applied in this research have been described previously [20, 30, 31].

As mentioned before by using the F/W-ratio of the breast normal tissue (F/W-ratio  $n>1$ ) and tumor tissue ( F/W-ratio  $n<1$ ), it is possible to distinguish the normal tissue from tumor tissue with high sensitivity and specificity [16]. By considering this, porcine adipose tissue was chosen to simulate the healthy breast tissue as both tissues have a F/W-ratio of higher than 1. Also, porcine muscle tissue with a F/W-ratio of lower than 1 was selected to simulate the breast tumor tissue which also has a F/W-ratio lower than 1. Briefly, similar as in Ref. [3] in all the experiments, the healthy breast tissue and tumor tissue were simulated by porcine adipose tissue and porcine muscle tissue, respectively.

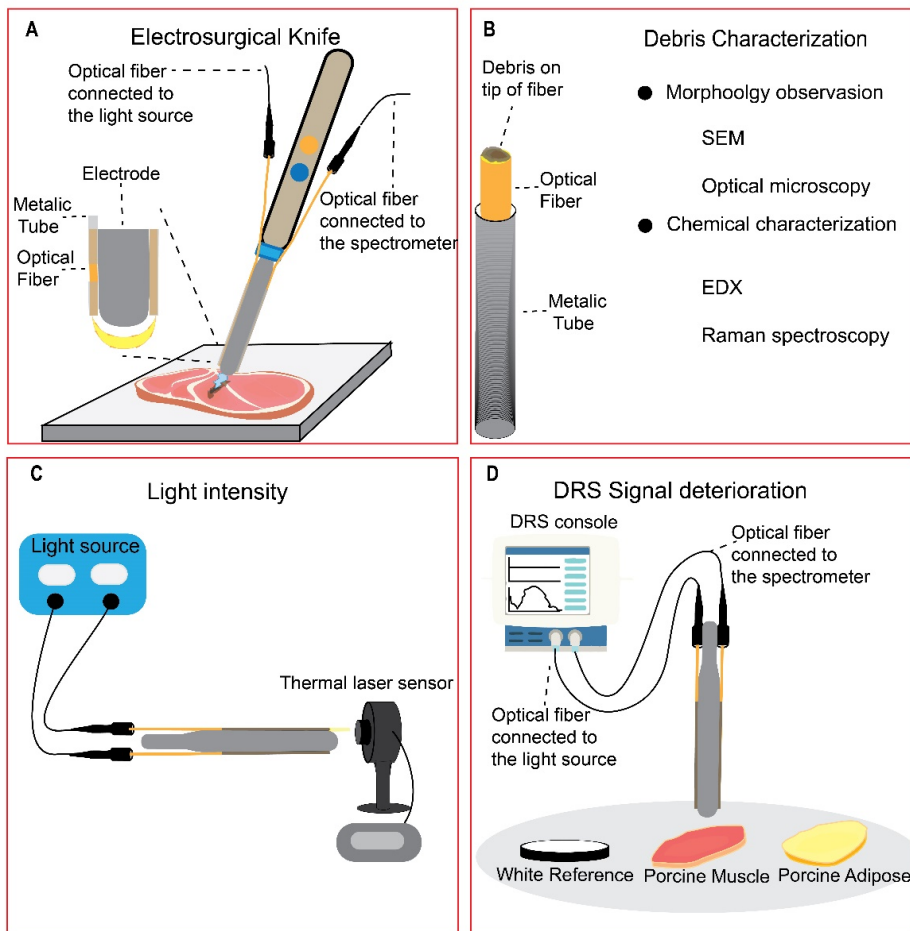


**Figure 2.1.** (A) The design of the electrosurgical knife integrated with DRS (fiber-fiber distance=3mm). (B) Characterizing the debris formed on the tip of optical fibers due to electrosurgery. (C) The used setup to measure the intensity of light passing through the clean and used optical fibers. (D) The setup to investigate the DRS signal deterioration after electrosurgery with three different sets of optical fiber, Clean Fiber (unused fiber), Muscle Fiber (contaminated with muscle tissue), and Fat Fiber (contaminated with adipose tissue) on three different surfaces (white reference, porcine muscle, and porcine adipose tissue).

## 2.2.2 Debris characterization

To create the samples (contaminated optical fibers) using the electrosurgical knife with integrated DRS, *ex vivo* porcine muscle and adipose tissue, an electrosurgical unit (Valleylab, Medtronic plc, USA) and a dispersive pad were used. The electrosurgical knife was used for 30 seconds, in blend mode combined with a power of 60W, to cut porcine

muscle and adipose tissue. For further analysis, the contaminated optical fibers were taken and used for the characterization (Figure 2.1(B)). In the text, Clean Fiber, Muscle Fiber, and Fat Fiber refer to the unused optical fiber, the optical fiber contaminated while cutting the porcine muscle tissue, and the optical fiber contaminated while cutting porcine adipose tissue, respectively.

After sample preparation, the used optical fibers (without connectors) were analyzed on morphology by optical microscopy (Keyence VHX-5000, Keyence Corporation, Japan) and scanning electron microscopy (SEM) (JSM-7500F, JEOL Ltd., Japan). For SEM analysis, the optical fibers were coated with a layer of gold using a gold sputter. The samples were placed under both microscopes and different magnifications were used to obtain images of specific parts of interest. The ImageJ software (version 1.52a, National Institutes of Health, USA) [32] was used to measure the diameter of the optical fibers from the images obtained with optical microscopy, before and after use.

To determine the debris chemical composition, the used optical fibers were analyzed on composition by energy-dispersive spectroscopy (EDX) (Noran system SIX, Thermo Scientific, United States). In this technique based on the interaction of a source of X-ray excitation and a sample, the elemental composition of the sample can be investigated [33]. It is suspected that the high temperature produced while working with the electrosurgical knife might cause the melting of the acrylate coating around the core of the optical fiber, which could lead to melted acrylate flowing over the tip of the fiber.

To investigate the presence of acrylate traces in the debris formed on the tip of the fibers after use, Raman spectroscopy has been used. A confocal Raman microscope (inVia, Renishaw plc., United Kingdom) with laser light of 752 nm was used to produce the clearest Raman spectrum. First, a spectrum from the acrylate coating was taken and the specific vibration peak related to the acrylate coating was determined. A map of the Raman shift from the entire surface of the optical fiber was made. The whole map was searched for specific vibration peaks corresponding to the acrylate coating determined before. As the surface of the optical fiber was not smooth due to debris formation, the Raman Spectroscopy was used to search for the acrylate vibration in different layers of the debris.

### 2.2.3 Light intensity analysis

In order to quantify the influence of the formed debris on the light transmittance through the optical fiber, the intensity of the light passing through the optical fibers was

measured, using a light source (same light source used for DRS measurements) connected to the optical fibers and a high sensitivity thermal laser sensor (NOVA II, Ophir Optronics Solutions, Israel) on the distal side, in front of the optical fiber tip. The light intensity of the optical fibers before and after applying electrosurgery was read from the display of the laser sensor, measured in power ( $\mu\text{W}$ ), as shown in Figure 2.1(C).

#### 2.2.4 DRS signal deterioration

To measure the effect of electrosurgery on the performance of the optical fibers integrated into the electrosurgical knife, the optical fibers at both sides of the blades were attached to the DRS console as described before, and the signal was recorded. For DRS measurements, three sets of DRS integrated knives were prepared for making each Clean Fiber, Fat Fiber, and Muscle Fiber (three knives to prepare each type of fiber). One of the optical fibers was used as the emitter of light and the other optical fiber was used to collect the light. First, the DRS console was calibrated in the wavelength ranging from 400 to 1600 nm, using clean optical fibers on a white reference (Control group) as described before.

With every three sets of each Clean Fiber, Muscle Fiber, and Fat Fiber, three spectra were obtained from white reference, porcine muscle tissue, and porcine adipose tissue separately (three spectra per surface)(Figure 2.1(D)). In total nine spectra per optical fiber (Clean Fiber, Muscle Fiber, Fat Fiber) per surface (white reference, muscle tissue, adipose tissue) obtained. In Fig 5. the average spectrum of these nine spectra with the SD for each type of optical fiber and each surface is shown.

The nine measured spectra were used as the input for a Philips custom-developed software. The software uses a nonlinear Levenberg–Marquardt inversion algorithm to fit a curve on the measured spectra and extract the concentration of the chromophore from the fitted data for each surface and each optical fiber [20]. More information regarding the algorithm used for fitting a curve on the DRS spectrum and calculating the concentration of the chromophores can be found in references [20, 31]. The average concentration of the chromophores ( $\pm$  SD) was used to analyze and report the results. The measured optical fit parameters are the amount of blood% (as a percentage of total hemoglobin concentration which is 150 g/liter in normal human blood), scattering at 800 nm, amount of collagen, the total amount of fat and water (fat+water) and the fraction of

fat. From the last two parameters, the amount of fat as Fat% and the amount of water as Water% and F/W-ratio were calculated [22].

To investigate how the contaminated optical fiber can affect the measurements, for each surface (white reference, muscle tissue, adipose tissue) the statistical analysis performed on the concentration of each chromophore using one-way ANOVA test.

### 2.2.5 Statistical analysis

All the experiments were repeated three times. One-way ANOVA was used to investigate whether the samples are significantly different or not. P-values smaller than 0.05 were considered significant.

## 2.3 Results

### 2.3.1 Debris characterization

The optical fibers used on the tissue (Muscle Fiber and Fat Fiber) became black after being used with an electrosurgical knife (Figure 2.2, top Side view row). From the side view of the optical fibers, it can be determined that the head of the optical fiber becomes black with an average length of 0.43 cm for Fat Fiber and 0.9 cm for Muscle Fiber. The diameter of the clean optical fiber obtained from the SEM images is  $238.9 \pm 1.95 \mu\text{m}$  with an acrylate coating with 10  $\mu\text{m}$  width on each side. The Muscle Fiber and Fat Fiber diameter changed to  $223.7 \pm 4.5$  and  $216.6 \pm 9.2 \mu\text{m}$ , respectively, with a nonsignificant difference between the two fibers ( $p = 0.19$ ).

Meanwhile, based on the optical microscopy and SEM images (Figure 2.2), less debris was formed on the tip of Muscle Fiber than Fat Fiber. While cutting porcine muscle tissue with the electrosurgical knife, tissue burning and carbonization was significant. However, after cutting the porcine adipose tissue, there was more melted fat on the optical fiber and surface of the electrode than burned tissue. Also, there were more traces of unburned biological tissue on the electrode and the metallic tubes of the knife used for cutting adipose tissue compared to those used for cutting muscle tissue. This is also observed for the Fat Fiber, which has some fat like pieces attached to it as shown in Figure 2.2.

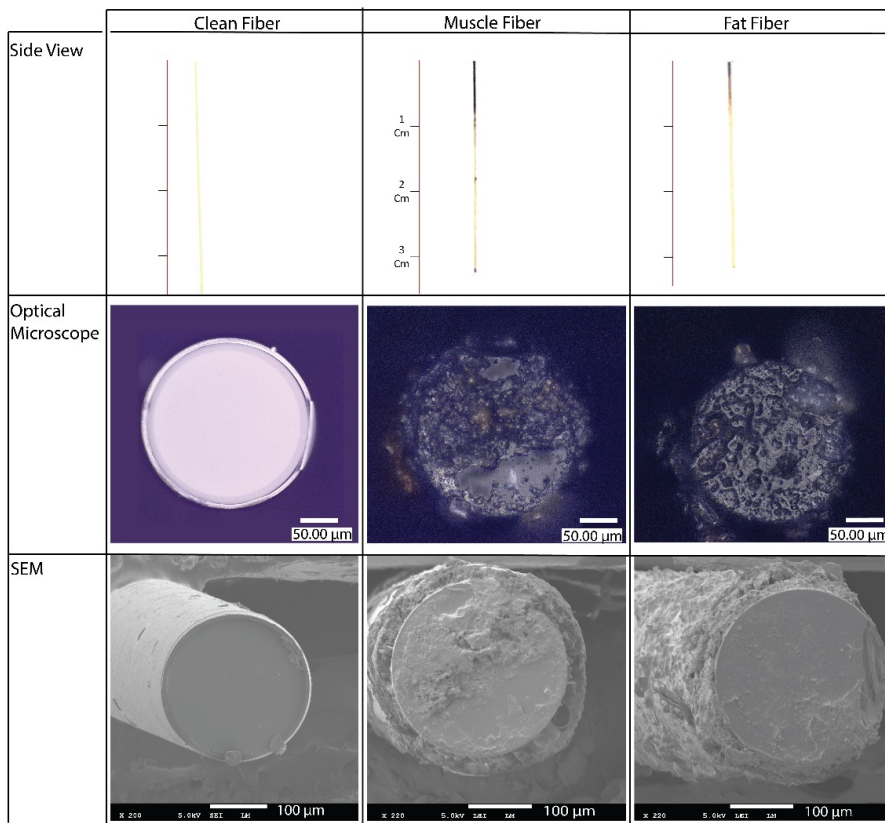


**Figure 2.2.** The shape and morphology of the optical fibers before and after electrosurgery, investigated by optical microscopy (second row) and scanning electron microscopy (SEM, third row).

When using EDX to map the chemical composition it was found that a Clean Fiber consists of a core made of silica or  $\text{SiO}_2$  (Si (silicone), in blue color, and O (Oxygen) in green and an Acrylate based coating which contains C (Carbone) shown in red color (Figure 2.3, top row). After applying the electrosurgical knife the surface of both contaminated fibers gets red meaning the carbon is covering the optical fibers (Figure 2.3, middle and bottom row). The density of the green color (presenting oxygen) and blue cover (presenting Si) decreases, showing that the contamination is covering the surface of the core. For both used optical fibers (Muscle Fiber and Adipose Fiber) there are traces of the Sodium (Na), Magnesium (Mg), Potassium (K) on the top. Furthermore, the EDX of Muscle Fiber confirms the existence of Iron (Fe) on the tip.

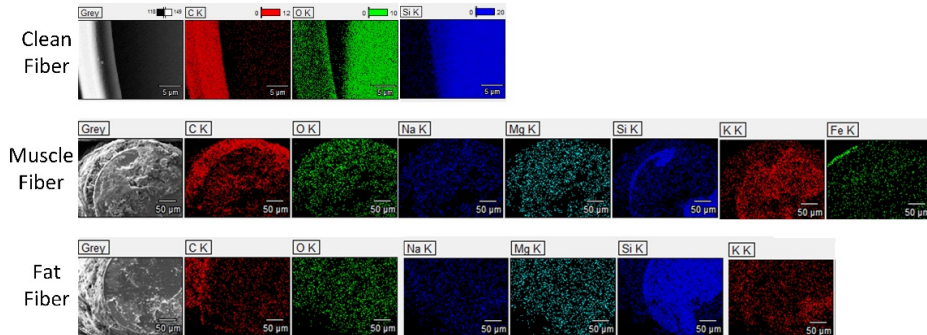


**Figure 2.3.** EDX (energy-dispersive spectroscopy) results taken from the tip of Clean Fiber, Muscle Fiber, and Fat Fiber.

The side view picture of a used optical fiber is shown in Figure 2.4(A). Based on this picture, it can be determined that the acrylate coating has vanished for approximately 500 μm from the tip of optical fiber. Raman spectroscopy of the clean optical fibers shows three main peaks, one at 1377, 1618 and 1782 Raman shift (cm<sup>-1</sup>), respectively (Figure 2.4(B)). Next, the Raman map taken from three different layers of the top surface of the Muscle Fiber and Fat Fiber was searched for the peaks found for acrylate coating. However, neither those peaks nor any other specific peak than the common silica glass was found in these three layers of the debris, indicating that vanished acrylate coating did not play a role in debris formation.

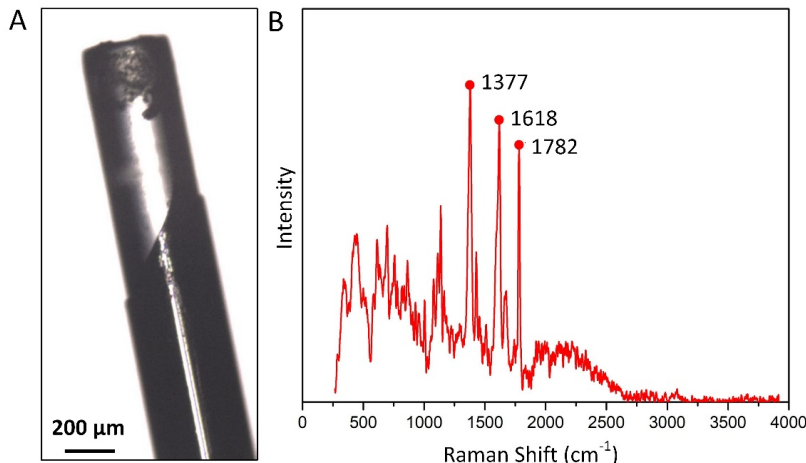


**Figure 2.4.** (A) a side view picture of a used optical fiber integrated into the electrosurgical knife. (B) Raman spectrum is taken from the acrylate coating of clean optical fiber.

### 2.3.2 Light intensity analysis

The intensity of the light passing through the clean optical fiber and the used optical fibers measured using a light source and laser sensor showed that the average power loss for the Muscle and Fat Fiber is  $45.64\% \pm 2.9$  and  $53.44\% \pm 19.77$ , respectively.

### 2.3.3 DRS signal deterioration

After fitting the spectra using the software, the fitted spectra have been used to make an average spectrum for each Clean Fiber, Muscle Fiber and Fat fiber in front of the white reference, muscle tissue, and adipose tissue which is shown in Figure 2.5 along with the SD area.

Spectra obtained using contaminated optical fibers display a decreased intensity on white reference and porcine muscle and adipose tissue for the 400-1600 nm spectral range. Fat Fiber lost more light intensity than Muscle Fiber. The spectrum of both Muscle Fiber and Fat Fiber on the white reference shows the main absorption peaks at wavelengths of 1211, 1393 and 1474 nm.

The spectra of Muscle Fiber and Fat Fiber on muscle tissue shows similar main peaks compared to Clean Fiber on muscle tissue. For the Fat Fiber, the absorption peak at 500-600 nm related to the blood region is less distinct. For both Muscle Fiber and Fat Fiber the slope of the spectrum between 700-900 nm decreases.

The spectrum obtained from porcine adipose tissue using optical fibers is shown in Figure 2.5(C). Again the Fat Fiber spectrum shows a less distinct peak at the 500-600 nm region. Also at wavelengths between 600 to 800 nm, the spectrum of Fat Fibers shows a smaller slope than the spectrum of Muscle and Clean Fibers.

Despite the intensity lost and a few changes, the spectra of the used optical fibers from white reference, porcine muscle, and fat tissue preserve the overall shape found in the spectrum taken by the Clean Fiber on the same tissues.

In Fig 6. the average of each chromophore concentration  $\pm$  SD and F/W-ratio  $\pm$  SD is shown. Fat Fiber on the white reference has a Fat% of 3.6% which is significantly different from the Fat% of the Clean Fiber on the white reference. Moreover, the Muscle Fiber shows a very low-Fat % with no significant difference with the control group. However, the Fat% of the spectra of porcine muscle and adipose tissue taken by Fat Fiber and Muscle Fiber is not significantly different from the Fat% of the spectra of the same tissues taken by the Clean Fiber.

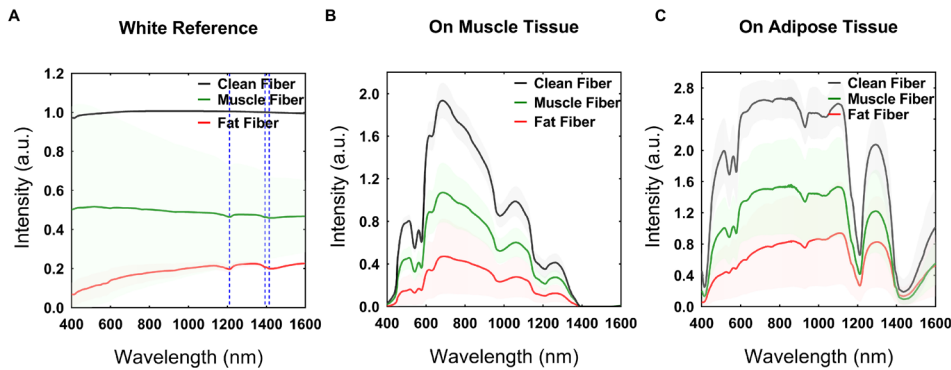


**Figure 2.5.** Fitted spectra using Clean Fiber, Muscle Fiber and Fat fiber in front of the (A) white reference, (B) in contact with muscle tissue and (C) in contact with adipose tissue.

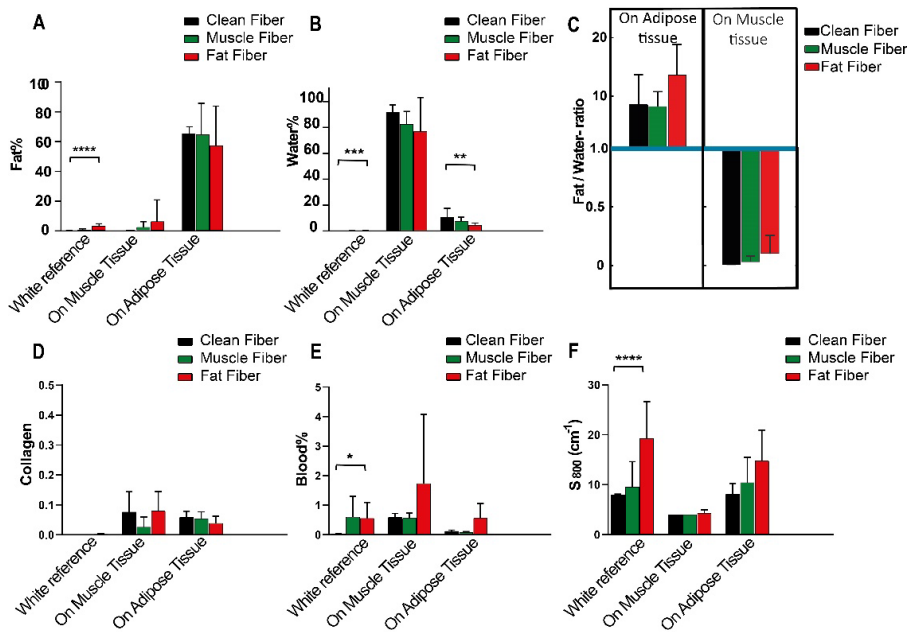


**Figure 2.6.** The concentration of chromophores derived from the obtained spectra using Clean Fiber (black), Muscle Fiber (green) and Fat Fiber (red).

Water% for all the optical fibers on the white reference was negligible. Also, the difference of Water% between the Muscle Fiber and the Clean Fiber on all surfaces was

not significant. The Water% between Clean Fiber and Fat Fiber for both white reference and adipose tissue showed a significant difference.

Figure 2.6(C) shows the F/W-ratio for porcine muscle and adipose tissue extracted from the spectra taken by clean and used optical fibers. The F/W-ratios for muscle tissue measured using Clean Fiber, Muscle Fiber and Fat Fiber are less than 1. While the Fat/Water-ratio of adipose tissue measured using Clean Fiber, Muscle Fiber and Fat Fiber are more than 1 (around 10).

The amount of Collagen for Muscle Fiber and Fat Fiber on the white reference, muscle, and adipose tissue do not show a significant difference with the amount of Collagen of Clean Fiber on the same surfaces.

Although less than 1% blood on the tip of the Muscle Fiber and Fat Fiber has been detected, the Blood% measured using contaminated optical fibers on muscle and adipose tissue shows no significant difference compared to the measured Blood% of Clean Fiber on same tissues.

Figure 2.6(F) shows that the reduced scattering (at 800nm) has increased more for Fat Fiber and less for Muscle Fiber on the white reference. The scattering measured with the Fat Fiber has a significant difference with the scattering measured with the Clean Fiber on the white reference. This increased scattering showed that the contamination on the tip of Fat Fiber can alter the scattering. The difference of reduced scattering at 800 nm between Clean Fiber, Muscle Fiber and Fat Fiber is not significant for the spectra obtained from the muscle and adipose tissue.

## 2.4 Discussion

In this study, we investigated the possibility of integrating a DRS system into the electrosurgical knife to investigate whether it would be possible to provide the surgeon with an intraoperative tumor margin assessment. The focus of this research was on the effect of the electrosurgery on the performance of the DRS system.

### 2.4.1 Debris Characterization

The results of debris characterization show that electrosurgery alters the shape and morphology of the optical fibers, integrated onto the electrode of the electrosurgical knife. During electrosurgery, the temperature around the electrodes significantly increases due to the passing electric current through the tissue [34]. By leading this current through the

tissue, the temperature rises to 100-400 °C and when temperature excess 200 °C, carbonization occurs and tissue turns black [35]. Furthermore, results from the diameter measurement of the tip of optical fibers indicate that the diameter of the optical fibers decreased with 20 µm which is almost equal to the width of the Acrylate coating around the core of the optical fiber. This means that after using the optical fibers with the electrosurgical knife, the acrylate coating around the optical fiber vanished. The results of the Raman spectroscopy of acrylate coating and the contamination show that there is no trace of melted acrylate coating on different layers of the debris, indicating that the acrylate coating has nothing to do with the debris formation on the tip. Another possibility can be that the acrylate coating melts and vaporizes during the use of the electrosurgical knife or that it attaches to the wall of the stainless-steel tube.

The black appearance of the head of the optical fibers can be due to the carbonization of the tissue close to it exposed to high-temperature heat and also some unburdened biological tissue. At temperature around 200°C, carbonization occurs, in which the organic molecules will break and carbon molecules with a brown and black appearance will appear [26, 35]. Meanwhile, the traces of the Na, Mg, and K confirm that some biological tissue residuals, as well as carbonized tissue, are covering the surface of the used optical fibers. Furthermore, on the Muscle Fiber, a trace of Fe is found, which is a building component of blood [36].

The average length of the burned area of the optical fibers used for cutting porcine muscle is longer than the average length of the burned area of the optical fibers used for cutting the porcine adipose tissue. The thermal conductivity of the porcine muscle ( $11 \times 10^{-4}$  cal/cm sec °C) is around 3 times higher than the thermal conductivity of the porcine adipose tissue ( $3.8 \times 10^{-4}$  cal/cm sec °C) [35]. So in comparison with muscle tissue, adipose tissue acts as a heat insulator and guards the blade and optical fibers from excessive heat and burning.

Meanwhile, the SEM shows more distinct debris particles attached to the tip of Fat Fiber than Muscle Fiber. As mentioned above, the heat insulation nature of fat may lead to less burned tissue. The lower burning effect produces less burned tissue while producing more isolated and clingy fat pieces with a tendency to attach to the optical fiber tip. While the burned debris is smaller in size, the clingy and isolated fat residues are bigger and cover more surface, which is visible also in the SEM and optical microscopy

pictures. This can cause less light passing through the Fat Fiber than Muscle Fiber and Clean Fiber.

### 2.4.2 DRS signal deterioration

The DRS spectrum obtained by used optical fibers on white reference shows three main absorption peaks at 1211 nm, 1393 nm, and 1414 nm, which are exactly the absorption peaks of Lipid [37]. This indicates that the main substrate on the tip of Muscle Fiber and Fat Fiber is the lipid, which is in agreement with the results of EDX. Although the intensity of the spectrum obtained using Muscle and Fat Fiber on porcine muscle and adipose tissue decreases, the overall shape of the DRS spectrum remains the same as the spectrum of the Clean Fiber used on the same tissues.

The F/W-ratio for adipose tissue, simulating the breast normal tissue, measured using used optical fibers remains greater than 1, whereas, the F/W-ratio for the muscle tissue simulating the breast tumor tissue remained lower than 1. This indicates that regarding the results of de Boer *et al.* [16], the integrated DRS system of the electrosurgical knife has the potential to distinguish the muscle tissue from adipose tissue based on F/W-ratio, even when the measurements are performed by the used and contaminated optical fibers. Photons between the emitter and collector fiber travel in a “banana-shaped” trajectory inside the tissue (Figure 2.1(A)). It has been shown that the depth of this banana-shaped region, is approximate of the order of the fiber distance [38, 39]. Accordingly, we expect that as far as the contamination on the tip of the optical fibers is only a thin layer of debris without any strong absorbing (in wavelength 400 nm to 1600 nm) component, it will not be affecting the results of DRS significantly. The effect of such a thin layer on the DRS outputs is negligible compared to the effect of the larger tissue volume, through which the light travels. Meanwhile, the results of the experiments also confirm that the thin layer of debris formed during the use of the electrosurgical knife does not have a significant effect on the results of DRS and its tissue discrimination capability.

During cutting different tissues with the DRS integrated electrosurgical knife, sometimes the produced debris due to electrosurgery, stuck in the empty gap between the optical fiber and inner wall of the metallic tube. Despite the weak connection, sometimes these pieces of the debris are big in size and may cover the area around the tip of optical fiber and don't let the light pass. To avoid these to happen, the void gap between the

optical fiber and metallic tube should be confined. Solutions might be reducing the size of the metallic tube or filling this void with a filler material.

Moreover, in our *ex vivo* experiments, the blood perfusion is missing. It has been shown that the presence of blood and methemoglobin (a blood derivative upon coagulation), would only influence the visible region of the spectrum and therefore would not affect the F/W-ratio [40]. However, in *in vivo*, the high volume of the blood in contact with the electrosurgical knife can lead to producing more debris as well as a thicker layer of the contamination resulting in more light intensity loss. To minimize the effect of the contamination, the optical fiber can be protected by a transparent material. A transparent material with self-cleaning properties can protect the tip of the optical fiber from being in direct contact with the tissue while maintaining the surface, which is in front of the optical fiber, clear due to the inherent ability of the material to remove the debris. Hence, developing a new design for integrating the optical fiber to the electrosurgical knife to have the minimum contamination and meanwhile be as close as possible to the tip of the electrode of the electrosurgical knife (to provide the connection between optical fibers and the exposed tissue), is something that should be considered for further developing the electrosurgical knife.

## 2.5 Conclusion

In this study, we investigated the effect of electrosurgery on the performance of the diffused reflectance spectroscopy system integrated into the tip of the electrosurgical knife. Debris formed on the tip of optical fibers is made of carbonized and unburned tissue. Although the light intensity of the DR spectra decreased after electrosurgery, the overall shape of the spectra remains significantly the same for each tissue. Furthermore, there was no significant difference between the concentration of the chromophores of the tissues measured by clean optical fibers and used optical fibers. Also, the F/W-ratio, which is the determinant parameter in distinguishing breast normal tissue (F/W-ratio  $>1$ ) from breast tumor tissue (F/W-ratio  $<1$ ), measured from the spectra taken by used fibers for muscle tissue remained lower than 1 and for adipose tissue remained greater than 1. This shows that electrosurgery does not affect the performance of the diffused reflectance spectroscopy integrated on the electrosurgical knife, and the system still can distinguish normal tissue from tumor tissue despite the effects of electrosurgery. Hence, this novel electrosurgical knife with integrated diffused reflectance spectroscopy technology may

provide the surgeon with real-time oncological guidance during breast-conserving surgery with the ultimate goal of reducing the positive margin incidence.

## Bibliography

- [1] E. R. Sauter, "Breast cancer prevention: Current approaches and future directions," vol. 14, no. 2, pp. 64, 2018.
- [2] C. Chiappa *et al.*, "Surgical margins in breast conservation," *International Journal of Surgery*, vol. 11, pp. S69-S72, 2013.
- [3] M. W. Adank *et al.*, "Real-time oncological guidance using diffuse reflectance spectroscopy in electrosurgery: the effect of coagulation on tissue discrimination," *Journal of biomedical optics*, vol. 23, no. 11, pp. 115004, 2018.
- [4] C. M. O'Kelly Priddy *et al.*, "The importance of surgical margins in breast cancer," *Journal of surgical oncology*, vol. 113, no. 3, pp. 256-263, 2016.
- [5] E. Sadot *et al.*, "Resection margin and survival in 2368 patients undergoing hepatic resection for metastatic colorectal cancer: surgical technique or biologic surrogate?," *Annals of surgery*, vol. 262, no. 3, pp. 476, 2015.
- [6] M. S. Moran *et al.*, "Society of Surgical Oncology–American Society for Radiation Oncology consensus guideline on margins for breast-conserving surgery with whole-breast irradiation in stages I and II invasive breast cancer," *Annals of surgical oncology*, vol. 21, no. 3, pp. 704-716, 2014.
- [7] M. Pilewskie, and M. Morrow, "Extent and role of margin control for DCIS managed by breast-conserving surgery," *Ductal Carcinoma In Situ and Microinvasive/Borderline Breast Cancer*, pp. 67-83: Springer, 2015.
- [8] C. Reyna, and S. M. DeSnyder, "Intraoperative margin assessment in breast cancer management," *Surgical Oncology Clinics*, vol. 27, no. 1, pp. 155-165, 2018.
- [9] R. G. Pleijhuis *et al.*, "Obtaining adequate surgical margins in breast-conserving therapy for patients with early-stage breast cancer: current modalities and future directions," *Annals of surgical oncology*, vol. 16, no. 10, pp. 2717-2730, 2009.
- [10] R. L. Klein *et al.*, "Evaluation of a hydrogel based breast biopsy marker (HydroMARK®) as an alternative to wire and radioactive seed localization for non-palpable breast lesions," *Journal of surgical oncology*, vol. 105, no. 6, pp. 591-594, 2012.
- [11] R. Rao *et al.*, "Experience with seed localization for nonpalpable breast lesions in a public health care system," *Annals of surgical oncology*, vol. 17, no. 12, pp. 3241-3246, 2010.
- [12] A. Keller *et al.*, "Diffuse reflectance spectroscopy of human liver tumor specimens—towards a tissue differentiating optical biopsy needle using light emitting diodes," *Biomedical optics express*, vol. 9, no. 3, pp. 1069-1081, 2018.
- [13] B. S. Nichols *et al.*, "A quantitative diffuse reflectance imaging (QDRI) system for comprehensive surveillance of the morphological landscape in breast tumor margins," *PLoS ONE*, vol. 10, no. 6, pp. e0127525, 2015.
- [14] L. Jacobs, "Positive margins: the challenge continues for breast surgeons," *Annals of surgical oncology*, vol. 15, no. 5, pp. 1271-1272, 2008.
- [15] E. R. St John *et al.*, "Diagnostic accuracy of intraoperative techniques for margin assessment in breast cancer surgery," *Annals of surgery*, vol. 265, no. 2, pp. 300-310, 2017.
- [16] L. De Boer *et al.*, "Fat/water ratios measured with diffuse reflectance spectroscopy to detect breast tumor boundaries," *Breast Cancer Research and Treatment*, vol. 152, no. 3, pp. 509-518, 2015.

[17] D. J. Evers *et al.*, "Diffuse reflectance spectroscopy: towards clinical application in breast cancer," *Breast Cancer Research and Treatment*, vol. 137, no. 1, pp. 155-165, 2013.

[18] L. L. de Boer *et al.*, "Towards detection of positive resection margins with diffuse reflectance spectroscopy during breast conserving surgery (Conference Presentation)," in Diseases in the Breast and Reproductive System V, Year, pp. 108560H.

[19] L. L. De Boer *et al.*, "Towards the use of diffuse reflectance spectroscopy for real-time in vivo detection of breast cancer during surgery," *Journal of translational medicine*, vol. 16, no. 1, pp. 367, 2018.

[20] R. Nachabé *et al.*, "Diagnosis of breast cancer using diffuse optical spectroscopy from 500 to 1600 nm: comparison of classification methods," *Journal of Biomedical Optics*, vol. 16, no. 8, pp. 087010, 2011.

[21] J. W. Spliethoff *et al.*, "Real-time in vivo tissue characterization with diffuse reflectance spectroscopy during transthoracic lung biopsy: a clinical feasibility study," *Clinical cancer research*, vol. 22, no. 2, pp. 357-365, 2016.

[22] L. L. de Boer *et al.*, "Using DRS during breast conserving surgery: identifying robust optical parameters and influence of inter-patient variation," *Biomedical Optics Express*, vol. 7, no. 12, pp. 5188-5200, 2016.

[23] D. J. Evers *et al.*, "Diffuse reflectance spectroscopy: toward real-time quantification of steatosis in liver," *Transplant International*, vol. 28, no. 4, pp. 465-474, 2015.

[24] E. J. Baltussen *et al.*, "Diffuse reflectance spectroscopy as a tool for real-time tissue assessment during colorectal cancer surgery," *Journal of Biomedical Optics*, vol. 22, no. 10, pp. 106014, 2017.

[25] M. Jermyn *et al.*, "Highly accurate detection of cancer in situ with intraoperative, label-free, multimodal optical spectroscopy," *Cancer research*, vol. 77, no. 14, pp. 3942-3950, 2017.

[26] A. Taheri *et al.*, "Electrosurgery: part II. Technology, applications, and safety of electrosurgical devices," *Journal of the American Academy of Dermatology*, vol. 70, no. 4, pp. 607. e1-607. e12, 2014.

[27] A. Yaroslavsky *et al.*, "Optical properties of selected native and coagulated human brain tissues in vitro in the visible and near infrared spectral range," *Physics in Medicine and Biology*, vol. 47, no. 12, pp. 2059, 2002.

[28] G. J. Derbyshire *et al.*, "Thermally induced optical property changes in myocardium at 1.06  $\mu$ m," *Lasers in Surgery and Medicine*, vol. 10, no. 1, pp. 28-34, 1990.

[29] J. P. Ritz *et al.*, "Optical properties of native and coagulated porcine liver tissue between 400 and 2400 nm," *Lasers in Surgery and Medicine*, vol. 29, no. 3, pp. 205-212, 2001.

[30] R. Nachabé *et al.*, "Estimation of biological chromophores using diffuse optical spectroscopy: benefit of extending the UV-VIS wavelength range to include 1000 to 1600 nm," *Biomedical Optics Express*, vol. 1, no. 5, pp. 1432-1442, 2010.

[31] R. Nachabe *et al.*, "Estimation of lipid and water concentrations in scattering media with diffuse optical spectroscopy from 900 to 1600 nm," vol. 15, no. 3, pp. 037015, 2010.

[32] C. A. Schneider *et al.*, "NIH Image to ImageJ: 25 years of image analysis," *Nature methods*, vol. 9, no. 7, pp. 671-675, 2012.

[33] J. I. Goldstein *et al.*, *Scanning electron microscopy and X-ray microanalysis*: Springer, 2017.

- [34] G. A. Vilos, and C. Rajakumar, "Electrosurgical generators and monopolar and bipolar electrosurgery," *Journal of minimally invasive gynecology*, vol. 20, no. 3, pp. 279-287, 2013.
- [35] M. G. Munro, "Fundamentals of electrosurgery part I: principles of radiofrequency energy for surgery," *The SAGES Manual on the Fundamental Use of Surgical Energy (FUSE)*, pp. 15-59: Springer, 2012.
- [36] M. Annals of surgeryRedígolo *et al.*, "Determination of reference interval values for inorganic elements in whole blood samples of humans and laboratory animals by X-ray fluorescence spectrometry," *Journal of Radioanalytical and Nuclear Chemistry*, vol. 297, no. 3, pp. 463-467, 2013.
- [37] T. M. Bydlon *et al.*, "Chromophore based analyses of steady-state diffuse reflectance spectroscopy: current status and perspectives for clinical adoption," *Journal of biophotonics*, vol. 8, no. 1-2, pp. 9-24, 2015.
- [38] S. C. Feng *et al.*, "Monte Carlo simulations of photon migration path distributions in multiple scattering media," in *Photon Migration and Imaging in Random Media and Tissues*, Year, pp. 78-89.
- [39] A. Koenig *et al.*, "Accessing deep optical properties of skin using diffuse reflectance spectroscopy," in *European Conference on Biomedical Optics*, Year, pp. 95370E.
- [40] J. W. Spliethoff *et al.*, "Monitoring of tumor radio frequency ablation using derivative spectroscopy," *Journal of Biomedical Optics*, vol. 19, no. 9, pp. 097004, 2014.

# 3

## Breast phantom

Emerging intraoperative tumor margin assessment techniques require the development of more complex and reliable organ phantoms to assess the performance of the technique before its translation into the clinic. In this work, electrically conductive tissue-mimicking materials (TMMs) based on fat, water and agar/gelatin were produced with tunable optical properties. The composition of the phantoms allowed for the assessment of tumor margins using diffuse reflectance spectroscopy, as the F/W-ratio served as a discriminating factor between the healthy and malignant tissue. Moreover, the possibility of using polyvinyl alcohol (PVA) or transglutaminase in combination with fat, water and gelatin for developing TMMs was studied. The diffuse spectral response of the developed phantom materials had a good match with the spectral response of porcine muscle and adipose tissue, as well as in vitro human breast tissue. Using the developed recipe, anatomically relevant heterogeneous breast phantoms representing the optical properties of different layers of the human breast were fabricated using 3D-printed molds. These TMMs can be used for further development of phantoms applicable for simulating the realistic breast conserving surgery workflow in order to evaluate the intraoperative optical-based tumor margin assessment techniques during electrosurgery.

Published as:

Sara Azizian Amiri, Pieter Van Berckel, Marco Lai, Jenny Dankelman, Benno H. W. Hendriks, Tissue-mimicking phantom materials with tunable optical properties suitable for assessment of diffuse reflectance spectroscopy during electrosurgery, *Biomedical Optics Express*, 2022.

### 3.1 Introduction

As the number of women diagnosed with breast cancer increases every year [1, 2], the challenge of complete tumor resection and achieving a negative margin during breast-conserving surgery (BCS) needs to be addressed. BCS is the preferred type of surgical approach for treatment of the patients with early-stage breast cancer. During surgery, the surgeon intends to remove the tumor completely from the breast of the patient and meanwhile preserve the overall shape of the breast as much as possible by avoiding unnecessary healthy tissue removal [3]. By investigating the excised specimens after BCS, the pathologist confirms whether the tumor resection was complete (negative margin) or that some parts of the tumor remained inside the breast of the patient after surgery (positive margin). When detecting a positive margin, treatment of the patient may have to be followed by a re-excision surgery or boost radiation therapy [3-5]. The occurrence rate of re-excision surgery ranges from less than 10% to around 50% which would ultimately lead to negative cosmetic outcomes associated with less patient satisfaction after surgery or additional morbidity [6-11]. Detecting tumor margins and discriminating diseased tissue from healthy tissue without any direct feedback during BCS, is a bothersome challenge for the surgeon during BCS [12-14]. Although using a margin assessment technique may appear to be quite effective in detecting the border of the tumor in BCS, each of the currently available techniques bears its limitations, so the challenge of finding an effective intraoperative tumor detecting technique still stands [8, 15, 16].

#### 3.1.1 Diffuse reflectance spectroscopy

Diffuse reflectance spectroscopy (DRS) is a non-destructive optical technology that measures the concentration of constituents of the tissue, based on its special intrinsic absorption and scattering of light in each wavelength [17-19]. It has been shown that DRS has the potential to be used as a real-time tumor margin detection technique during breast cancer surgery. DRS enables discrimination of diseased- from healthy tissue in different organs based on the different tissue-light interactions that originate from the different tissue compositions [20-30]. The study of De Boer et al. on application of DRS for investigating the *ex vivo* lumpectomy specimens showed that using a threshold F/W-ratio, breast tumor tissue (with F/W-ratio lower than the determined threshold) can be distinguished from benign tissue (with F/W-ratio higher than the specified threshold) with a specificity and sensitivity of 100% when the tumor border sites are not included. The F/W-ratio of breast tissue varies from patient to patient, hence, a patient-specific

F/W-ratio needs to be defined using the F/W-ratio of the healthy tissue as a reference [21]. Moreover, in another *in vivo* study, the F/W-ratio provided the most effective discrimination between the tumor and healthy tissue with the Area Under Curve (AUC) of 0.94 in a Receiver Operator Characteristic (ROC) analysis [20, 31]. Furthermore, De Boer et al. also showed that among different classification methods, models developed based on the F/W-ratio (mean sensitivity: 0.71, mean specificity: 0.99), full-spectrum (mean sensitivity: 0.94, mean specificity: 0.89) and selected wavelengths (eight wavelengths, mean sensitivity: 0.95, mean specificity: 0.91) were of the most promising predictive models for distinguishing the breast malignant tissue from healthy tissue using DRS [24].

Since DRS is a promising tumor margin assessment technique, DRS can be integrated into common surgical instruments to provide surgeons with real-time and intraoperative feedback of the tissue. For the same purpose, we recently developed an electrosurgical knife integrated with DRS and showed the possibility of detecting the tissue type while cutting/coagulating it [32-34]. The developed prototype has been tested on *ex vivo* porcine adipose and muscle tissue, assuming those tissues represent human healthy and tumor breast tissue sufficiently [32-34]. However, to allow for a successful transition of the prototypes into the clinical phase, more precise validation and accurate assessments are needed. The application we are aiming for includes electrosurgery to excise specimens. Tissue mimicking materials (TMMs) can be developed to allow electrosurgery on them, and hence simulation of the workflow of the realistic breast conserving surgery (lumpectomy). In addition, these TMMs and phantoms can be developed to closely simulate the optical properties of the different layers of the breast tissue. The development of such TMMs could make it possible to form a well-controlled environment for the accurate evaluation of the DRS-integrated electrosurgical knife or, in general, other relevant optical-based margin assessment techniques during electrosurgery.

### 3.1.2 Breast phantoms

Nowadays, tissue-mimicking materials (TMM) and phantoms are a vital part of medical device development. Using a phantom enables accurate validation, optimization and calibration of the new device before its transition to clinical applications. Moreover, a realistic organ phantom can be useful for training medical residents and surgeons to employ the new surgical instrument or intraoperative imaging system in the workflow of

the surgery [35, 36]. Up to now, several phantoms have been developed by researchers for assessing the optical or spectral tissue sensing systems in clinical applications such as diffuse optical spectroscopy [35, 37], fluorescence imaging [38, 39] optical tomography [40-42], photoacoustic imaging [43, 44] and also for the assessment of optical imaging systems in combination with other imaging techniques such as MRI [45] or ultrasound [46].

A realistic breast phantom enables simulation of the different properties of breasts layers as well as the surgical workflow of BCS. For such a realistic phantom the following requirements are defined:

1. Validation of DRS and DRS integrated in the electrosurgical knife, requires that the phantom represent realistic fat- and water percentages of different layers of the breast. As mentioned before, the amount of fat and water in healthy and tumor breasts tissue is a determinative factor for detecting these two tissues using DRS [21]. For instance, a phantom with different layers, same as human breast, each with a distinct F/W-ratio, could be very useful in evaluating the application of the DRS in tumor margin detection. Moreover, detection of the border of the tumor before actually reaching it can be easily and explicitly examined using a layered phantom.
2. To simulate realistic breast surgery, the TMM must be made such that it can be cut with an electrosurgical knife. During the electrosurgery, a radio frequency alternating current is used to induce oscillation of the ionized molecules inside the tissue, which subsequently converts into thermal energy leading to an increase of the local tissue temperature, and finally tissue rupture. Similar to human tissue, the TMM should have enough ions, or in other words, sufficient electrical conductivity [47, 48].
3. The TMMs should not extensively melt during electrosurgery when exposed to high temperatures. During electrosurgery, depending on the settings and tissue properties, the tissue temperature quickly rises to temperatures higher than 100°C, which results in localized tissue cutting/coagulation [49]. The various compounds may melt excessively after exposure to this high temperature. The TMMs are expected not to melt but rather cut cleanly (burned) during electrosurgery, similar to human tissue.

4. The TMM is preferred to show realistic tissue effects such as burning and debris formation during electrosurgery.
5. To simulate the anatomy of the breast realistically, a stable TMM in a realistic breast shape and layer configuration is needed.
6. Encompass other properties such as the ease of manufacturing, shape- and property stability over time, and cost-effectiveness.

Among different types of TMMs, biological-based compositions fulfil these requirements better than non-biological-based compositions. For instance, it is challenging to find and produce polymeric TMMs that represent the optical properties of fat and water sufficiently while being electroconductive [50]. Using water-soluble components, such as gelatin and agar, enables the use of fat and water, which leads to the simulation of the realistic tissue composition and optical properties [37]. On the other hand, using polymers such as polyvinyl chloride (PVC), silicone, polyester and polyurethane makes it almost impossible or difficult to include biological fat and water. In this case, additives such as glass microsphere, carbon black, titanium dioxide ( $TiO_2$ ), microspheres, aluminum oxide ( $Al_2O_3$ ) and gold nanoshells are needed to reach the absorption and reduced scattering coefficient of human breast tissue [36, 40, 43, 51-53]. The addition of large number of additives makes the production process more complex, expensive and time-consuming. Furthermore, closely simulating the absorption and reduced scattering coefficient of fat and water in a continuous wavelength range using these additives is challenging [36, 40, 43, 51-53]. In some applications in which monitoring the tissue only requires measuring the optical response of the tissue in one or a few wavelengths, additives such as  $TiO_2$  can be used to closely simulate the absorption and/or scattering profile of the tissue at those specific wavelengths [44]. However, it has been shown that a continues full-spectrum (400-1600nm) DRS measurement or at least DRS measurement in eight specific wavelengths are required for correct detection of the breast tumor tissue from healthy tissue (or estimate the F/W-ratio of the tissue) using DRS [22].

Besides, most polymers are not electroconductive, hence to make them conductive more additives are needed, which bears more effort and drawbacks [54].

Agar and gelatin have been used vastly in producing different tissues mimicking compositions and phantoms [55, 56]. Both biopolymers are relatively cheap, easy to process and can easily form different shapes. In comparison to agar (with a melting point

of around 85°C), gelatin has a lower melting temperature of around 35°C, which makes gelatin less suitable for a phantom meant for electrosurgical applications [36, 51, 57]. Moreover, it is possible to adjust the electrical conductivity of these two biopolymers using additives such as sodium chloride (NaCl) [58]. One disadvantage of using some hydrogels is the lower life span and durability due to reducing water content or bacterial invasion. However, by controlling the packaging process and storage temperature or using preservative additives such as ethylenediaminetetraacetic acid (EDTA) or sodium azide (NaN<sub>3</sub>), the durability of the agar and gelatin-based phantoms can be expanded [36]. TMM such as gelatin and agar, enables the development of a solid phantom that resembles the fat- and water percentage of the healthy and malignant breast tissue [37, 41, 59, 60].

### 3.1.3 Fat-water based phantoms for medical optics: mini-review

Water-lipid compositions are desirable for making phantoms due to having the main biological components of breast tissue and many other organs. Recently these types of phantoms became popular in evaluating microwave imaging systems, in which the determinative parameter in distinguishing tissues from each other is the dielectric characteristics of the tissue. In these phantoms, water is mixed with different lipids and oils such as Kerosene, safflower oil, glycerin and grape seed oil [61-69]. Water-lipid phantoms have also been used for other imaging techniques. For instance, Merritt et al. developed a series of phantoms consisting of water, soybean oil and Triton x-100, where water and soybean oil represented the absorption characteristics of breast's water and fat, whereas Triton x-100 functioned as an emulsifier for water and lipid. These phantoms were used with water percentages ranging from 30 to 100 percent, on which a quantitative analysis was performed and the potential of MRI and diffuse optical spectroscopy in receiving the fat and water signals were compared. A good correlation between the results of these two systems was found [45]. Michaelsen et al. developed different anthropomorphic water-lipid based breast phantoms using different lipids (butter, margarine, olive oil, canola, vegetable oil and lard) as well as different emulsifiers (guar gum, soy lecithin and borax). Ultimately, guar gum in combination with water and lard was the most promising combination for a successful phantom. Compositions with fat and water percentages from 15% to 85% were produced for simulating layers of the breast. The final phantom was breast shaped and included an adipose layer with 30% water and

70% lipid, a fibroglandular layer with 70% water and 30% lipid, and a tumor insertion with 80% water and 20% lipid. Near-infrared tomography measurement showed the water percentages ranged from 30% for the adipose layer to 73% for the tumor [41]. Quatrole et al. also developed phantoms based on distilled water and commercial pork fat either with or without emulsifiers, to assess the capability of diffuse reflectance spectroscopy to estimate the concentrations of the constituents. Agar and Triton-X were used as emulsifiers to produce phantoms with 30-70%, 50-50% and 70-30% fat-water concentrations. Among all the phantoms, the group which was made of 1% agar showed better stability for the whole range of F/W-ratios. However, handling agar as a thickener complicated the production process, as precise control over temperature and timing are required to secure the agar phantom formation. Using Triton-x enabled the formation of all F/W-ratios, nevertheless, Triton-x led to higher scattering properties than tissue and low phantom durability of around 2-3 hours [59]. Ohmae et al. established semi-solid phantoms using distilled water, soybean oil as lipid, soybean lecithin as an emulsifier and either agar or oil solidifying agent as a coagulant. In their research, agar was used for phantoms with 99%, 80% and 60% of water (oil-in-water) and an oil solidifying agent was used for phantoms with 40%, 20% and 5% of water. To assess the water-to-lipid volume fraction of the phantoms, a six-wavelength time-domain diffuse optical spectroscopy system was used to estimate the concentration of constituents and suitability of the phantoms for this purpose [37]. Recently, Bush et al. developed a recipe of a fat-water phantom with a fat fraction of 0%, 25%, 50%, 75% and 100% consisting of distilled water, agar, oil-soluble, sodium benzoate and peanut oil. They showed a good correlation between the fat fraction measured by MRI and the target values in the developed phantoms [60].

The challenge regarding the development of these phantoms is to achieve good stability and homogeneity as well as the desired absorption and scattering profile. In this research, we developed four different phantom material recipes to simulate the different layers of the breast phantom. To simulate the fat content of human breast tissue as close as possible, pure porcine fat or lard were used in all phantoms. Like human white adipose tissue which is made up of mostly lipids in the form of triglycerides, lard consists of 97.9% triglycerides. This resemblance in composition between lard and human adipose tissue, as well as the fact that lard is easily accessible, makes lard a great and competent material to represent human adipose tissue in phantoms [70].

For the phantoms, agar and gelatin were both used as emulsifiers for fat and water, as well as a coagulant to solidify and stabilize the phantoms. In comparison with agar, gelatin has low thermal stability which makes it less suitable for electrosurgery. Lately, blending of polyvinyl alcohol (PVA) and gelatin has gained attention since the final product of this combination exhibits improved properties that could not be obtained from each of these polymers alone [71-74]. For instance, Thangprasert et al. showed that combining PVA and gelatin to form a hybrid hydrogel led to an increase of the compressive stress and young's modulus of the final composition [75]. Therefore to increase the overall stability of the gelatin phantom, PVA was used in one of the four phantoms in combination with lard, water and gelatin. Additionally, in this research, we used transglutaminase (TG) to enzymatically cross-link the gelatin to improve its stability and gel strength. TG is vastly used in the food industry to crosslink the proteins in milk and meat. Crosslinking gelatin using TG, results in a hydrogel with promising characteristics for biomedical and tissue engineering applications [76-81].

In this chapter, TMMs were designed to simulate the optical properties of different layers of the human breast such that electrical surgery can be performed on those. The ultimate goal of producing such TMMs and phantom is to use them for assessment of the capability of the DRS system in detecting the tumor border while using the electrosurgical knife to excise the tumor during the breast conserving surgery (lumpectomy). For this purpose, four groups of phantoms were produced, namely based on lard-water-agar (Agar phantom), lard-water-gelatin (Gelatin phantom), lard-water-gelatin-PVA (Gelatin-PVA phantom) and lard-water-gelatin-TG (Gelatin-TG phantom). To the best of the authors' knowledge, these are the first results reported on the combination of lard-water-gelatin with or without PVA and TG to produce a TMM and a phantom. Phantoms with different amounts of fat and water content were produced to simulate the breast's different layers and tumor tissue. Diffuse reflectance spectroscopy was used to characterize the phantom materials. Unlike other studies in this area, light in 1000nm-1600nm wavelength was used to measure the spectral response and optical properties of the phantom materials, as it has been shown that fat and water have their main optical absorption in this wavelength range [19, 82].

The effect of electrosurgery on the TMMs was inspected qualitatively and the stability of the TMMs over time was investigated. Eventually, using the phantom materials, anatomically relevant heterogeneous breast phantoms representing the

physiological composition and optical properties of human breast tissue including a tumor were developed for further research.

## 3.2 Materials and Methods

### 3.2.1 Phantom materials preparation

Four different phantoms were developed, an Agar-based, Gelatin-based, Gelatin-TG-based and Gelatin-PVA-based phantom. For each phantom, three different compositions of Adipose, Gland and Tumor were used that represent the different layers of the breast, namely the adipose-, fibroglandular- and tumor tissue layer, respectively. The F/W-ratio of the Adipose, Gland (fibroglandular) and Tumor layer was respectively 60-40%, 40-60% and 20-80%. Table 3.1 indicates the amount of each component to produce 100ml of each layer. The steps for producing each phantom are summarized in Figure 3.1. To make the phantoms, agar powder extracted from red algae (HL0106, Natural Spices) or bovine gelatin powder 250 Bloom (ES1477, Natural Spices) were used as emulsifier. Pure lard (without any additives), which was produced by melting the belly fat of the pig at a low temperature, was purchased (ready to use) from the online butcher shop (JP Puurvlees, Netherlands). Also, a gelling agent, distilled water, Sodium Benzoate (Sigma-Aldrich, USA) as a preservative agent, and Barium sulphate (BS) (Hinmeijer, Netherlands) as a tumor contrast agent for x-ray imaging were used.

Moreover, NaCl (Jozo, Netherlands) was used as an additive to manipulate the electrical conductivity of the TMMs, which leads to the free movement of ions in the solution and improvement of the conductivity [83]. Different concentration of NaCl (from 0.1 to 10 wt%) has been used in developing Agar phantoms that could mimic the electrical conductivity of various tissues for studying the effect of background tissue on radiofrequency-induced heating [84]. NaCl with concentration of 1% (or close to 1%) has been used in different studies for producing hydrogel phantoms based on TX-150 or agar or gelatin or synthetic polymer to adjust the electrical conductivity to represent the electrical properties of for example breast or muscle tissue [85-88].

Briefly, to develop the Agar phantom, the melted lard (in volume unit) was added to the water (in volume) mixture containing all the other chemicals (in mass unit) at boiling temperature.

**Table 3.1.** Materials for producing phantoms.

	For all phantoms				Only for Agar Phantom		Only for Gelatin based phantom		
	Lard (ml)	Water (ml)	NaCl (g)	Sodium benzoate (g)	BS (g)	Agar (g)	For all Gelatin based phantoms	Only Gelatin-TG Phantom	Only Gelatin-PVA Phantom
							Gelatin (g) (15%)	TG 1 g /6 g Gelatin	PVA(g)
Adipose	60	40	0.4 (1%)	0.04 (0.1%)	-	1.2 (3%)	6 (15%)	1 g	4 (10%)
Gland	40	60	0.6 (1%)	0.06 (0.1%)	-	1.8 (3%)	9 (15%)	1.5	6 (10%)
Tumor	20	80	0.8 (1%)	0.08 (0.1%)	1.6 (2%)	2.4 (3%)	12 (15%)	2 g	8 (10%)

To produce the Gelatin based phantoms, the lard was added to the water mixture at 50 °C. The percentage of the agar, gelatin, NaCl, sodium benzoate, and barium sulphate were based on the volume of the water. Right after adding lard to the water mixture for all phantom materials, a creamy opaque mixture was formed. To produce the Gelatin-TG phantom, after adding the lard to the gelatin-water mixture, the TG was added to it very slowly while the mixture was on the stirrer. The Agar, Gelatin and Gelatin-TG phantoms were stored in the freezer for 1 hour and then refrigerated overnight. For the Gelatin-PVA phantom, a PVA-water mixture (PVA 10% g/ml.) was prepared beforehand and placed on a heater stirrer until the temperature reached 50 °C. Then the PVA mixture was added to the gelatin –lard water mixture and followed by staying on heater stirrer at 90 °C for one hour. Then the Gelatin-PVA mixture was stored in the freezer overnight and after that refrigerated. All phantom materials were produced in three replicates (three different batches). Before carrying out any assessment, all phantoms were taken out of the refrigerator and stayed at room temperature for 1 hour.

### 3.2.2 DRS measurements

To investigate the optical properties of the phantom materials and validate their application for DRS measurement, a Philips custom-designed diffuse reflectance spectroscopy setup (Philips Research, Eindhoven) was used. The device includes a

halogen broadband light source (Avantes, The Netherlands) and a spectrometer designated to collect the light in the 900-1700 nm spectral range (NIRQuest 512, Ocean Optics, USA).

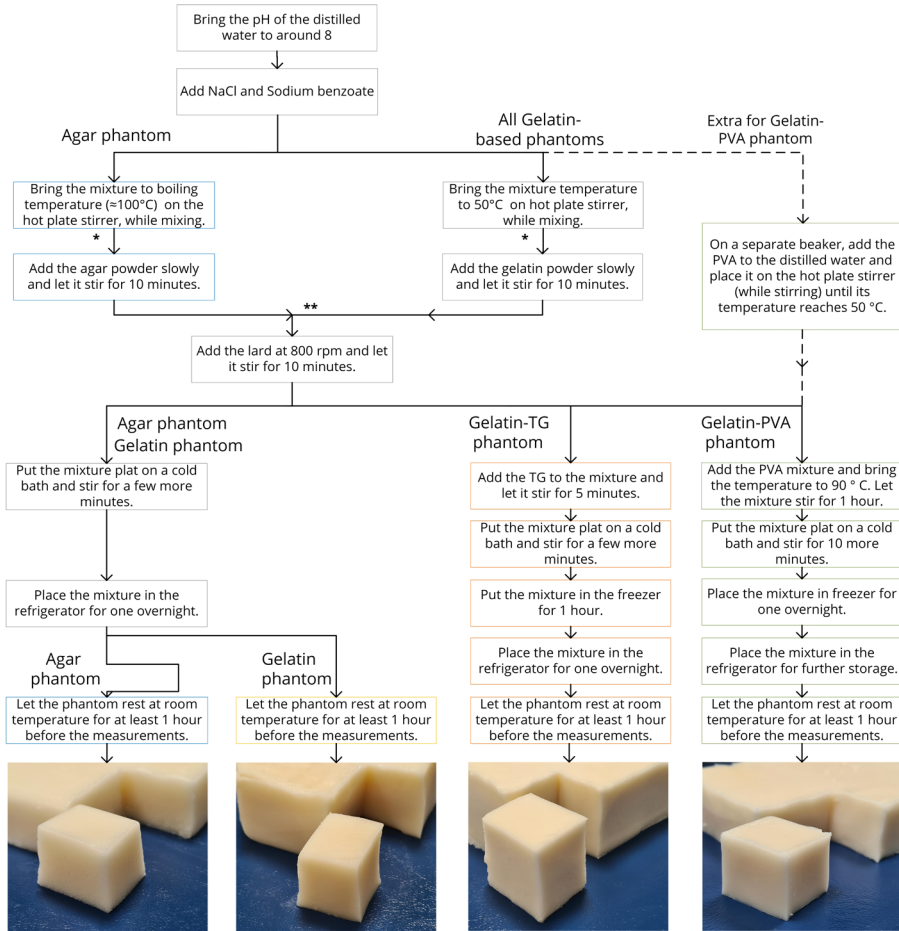


**Figure 3.1.** Steps involved in producing four different phantoms.

A flat-tipped optical needle consisting of two optical fibers (with a total diameter of 220  $\mu\text{m}$ , core diameter of 200  $\mu\text{m}$  and numerical aperture (NA) of 0.22) with orientation parallel to the axis of the needle probe (end of the optical fibers are perpendicular to the probe axis) and a center-to-center fiber distance (FD) of 1.2 mm (fiber distance, FD), was used to emit the light from the light source to the tissue and collect the light to the

spectrometer [32-34]. The setup used in this experiment is shown in Figure 3.2(A). The measurements of the spectrometer were used as inputs for a Philips custom-developed Matlab-based software. In this software, the spectra were fitted with an analytical model, as explained in Figure 3.2(B) which has first been described by Farrell et al. [89], by applying a nonlinear Levenberg–Marquardt inversion algorithm and subsequently the concentration of the chromophores were extracted from the fitted data [18, 23]. More information regarding the design and application of diffuse reflectance spectroscopy can be found in these publications [17-19, 23, 90].

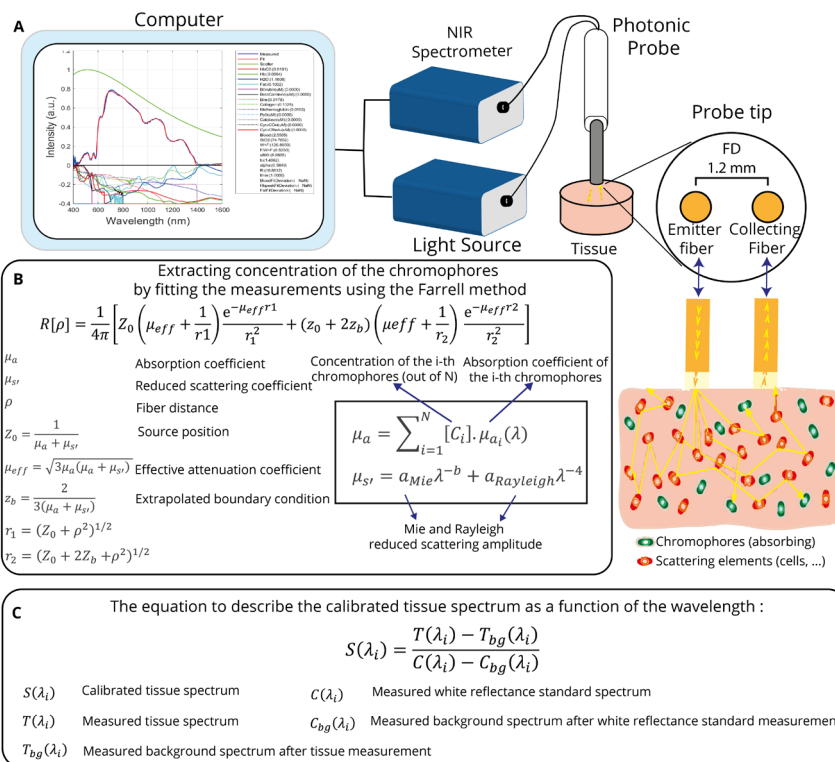


**Figure 3.2.** (A) Custom-designed diffuse reflectance spectroscopy setup (made available by Philips). (B) Analytical models to translate the DRS measurements and calculate the concentration of the physiological parameters [91]. (C) Data pre-processing for calibration of the DRS system to compute the tissue spectrum from the measured and the calibration spectra [18, 91].

Calibration was carried out for the DRS setup, to minimize the effect of ambient light and emending the system response. For this purpose, using a probe-holder, the tip of the photonic needle was fixed on a 2 mm distance from a white reflectance standard

(Spectralon with reflectivity of 99% for 400-1500 nm and >96% for 250-2000 nm, model:WS-1-SL, Labsphere Inc., USA) (the distal end of the fibers were parallel to the standard). A 2 mm distance from the Spectralon was shown to provide sufficient accuracy for the DRS measurements (data not shown). Then the calibration was followed by measuring the spectral response of the white reference along with a background measurement [17, 18, 23]. In more detail, first, an inner wavelength calibration was performed on the sensor array of the detector to assign a wavelength to each pixel. Then the white reflectance measurements were performed (in front of the Spectralon) to measure the system response, and those were used later to offset the spectral shape of the light from the lamp as well as any wavelength-dependent sensitivity in the detector or optics of the system. Then to diminish the effect of the ambient light, a background measurement was performed. Moreover, each tissue/phantom measurement was followed by a background measurement by shuttering the light input. Eventually, the final tissue spectrum was defined using the equations mentioned in Figure 3.2(C) as a function of the wavelength [18].

All the phantom/tissue measurements were obtained by placing the tip of the needle probe (optical fibers) at the distal end parallel and in contact with the TMMs and tissues. From each phantom material, three different locations were chosen randomly and from each location, three DRS spectra were obtained (produces nine spectra per phantom material). The fitted spectra of each measurement were calculated by using the software and consisted of the absorption profile, reduced scattering profile and concentration of chromophores. The extracted optical parameters for each spectrum are the total amount of fat and water (fat+water) and the fat fraction. Using the fat+water and fat fraction, the percentage of fat as Fat% and the percentage of water as Water% and F/W-ratio were calculated [21].

Moreover, the DRS measurements from human in vitro breast tissue reported by [92] was used in this chapter to compare the characteristics of the TMMs with the targeted human tissue. These data had been taken from freshly excised breast tissue from normal fat, glandular, fibroadenoma lesions and (pre)-malignant locations.

Furthermore, as porcine adipose and muscle tissue own almost similar F/W-ratio as healthy and tumor breast tissue respectively [33, 34], the spectral measurement from the two porcine tissues were used as a reference to relate the phantom spectral results to real breast tissue.

### 3.2.3 Electrosurgery

To study the effects of electrosurgery on the phantom materials, an electrosurgical knife with a blade shape electrode (WEIDE, Hangzhou Valued Medtech Co.,Ltd, China) connected to an electrosurgical unit (Force FX, Valleylab, Medtronic plc, USA) was used, as well as a dispersive pad. The knife was applied to each phantom material in the blend mode with 60 W power setting. To qualitatively compare the effects of electrosurgery on phantom tissue with the real tissue, porcine adipose and muscle tissue were used to simulate breast healthy and tumor tissue, respectively.

### 3.2.4 Stability over time

To investigate the stability of the phantom materials over time, DRS measurements were carried out on the phantoms after 10 days after the production day. During these 10 days the phantoms were stored in the refrigerator (4° C). Moreover, visual inspection was performed 3 weeks after the production day to check the morphological stability of the phantom materials over time.

### 3.2.5 Breast phantom preparation

The process of shaping the breast phantom was inspired by the work of Dantuma et al [44]. To prepare the breast phantoms, three phantom materials with the best results were chosen (the reason will be discussed later). One 3D printed mold in the shape of a human breast and another 3D printed mold to form the fibroglandular layer were made, using the design of the models used in reference [44, 93, 94], as shown later in a figure. Silicone molds were made to produce tumors in different shapes and sizes. Following the process of realistic heterogeneous phantoms production in, first, the inner wall of the main breast mold was filled with a thin layer of silicone rubber (Dragon Skin™ 10 MEDIUM, Smooth-On, Inc.). This silicone layer allows the final phantom to be easily detached from the mold. In addition, silicone rubber can be dyed with skin-like colors to visually simulate the skin layer. Then the mold was filled with the adipose mixture while the fibroglandular mold was inserted inside it. The mold was stored in the freezer and after 1 hour the fibroglandular mold was removed carefully. In this way, the adipose layer was formed with a fibroglandular cavity in it. Tumors were made by filling the silicone molds with the tumor materials and letting the tumors rest in the freezer for 1 hour. To complete the phantom, tumors were fixed inside the fibroglandular layer cavity using wires and supports to hold those in the right positions. The gland mixture was poured

inside the cavity and the whole phantom was stored in the freezer for 1 hour. Afterwards, the phantom was taken out, the wires were pulled out and the phantom was separated from the mold, and finally the phantoms were stored in the refrigerator overnight. Moreover, to inspect the visual similarity between the layers of the phantom, a layered phantom consisting of Tumor, Gland and Adipose layer was made using the Gelatin-TG TMMs.

### 3.2.6 X-Ray validation

Three phantoms were made for the X-ray imaging. The X-ray imaging was performed using the Allura system (Philips Healthcare, Best, The Netherlands). With this system a 3D reconstructed volume with 0.5-mm voxel size of the phantoms was created.

### 3.2.7 Statistical analysis

For all the layers in each phantom, three replicates were made separately, which resulted in three Adipose, Gland and Tumor phantoms materials for each of the four different phantoms. For DRS measurements for each phantom material, three measurements were taken at three different locations of the phantom. To show the results of the spectra (DRS, absorption and reduced scattering), the mean spectra  $\pm$  SD (standard deviation) for each phantom material (results of nine spectra for each phantom material) was used in the figures. For DRS measurements, before calculating the mean, all the spectra were first normalized. To study the significance of the data, t-test was used considering P values lower than 0.05 as significant. For all the statistical data analysis, GraphPad Prism version 8.1.2 (GraphPad Software, La Jolla California USA, [www.graphpad.com](http://www.graphpad.com)) was used.

## 3.3 results

Three different mixtures of phantom materials were produced, namely Adipose with 60% fat-40% water, Gland (representing fibroglandular layer) with 40% fat-60% water and Tumor with 20% fat and 80% water (percentage based on the total amount of fat and water). All phantom materials were stable when separated from the plate/mold and there was no sign of phase separation in the form of layers or particles. All phantoms were assessed on day 1 of production, after removing them from the refrigerator and letting them rest for 1 hour at room temperature. First, DRS measurements were carried out followed by electrosurgery and finally x-ray imaging was performed.

### 3.3.1 DRS measurements

The results of the DRS measurements of the phantom materials can be found in Figure 3.3. The normalized spectra for each material are the mean spectra  $\pm$  SD of all measurements from different locations of each replicates. Moreover, Figure 4 shows the absorption and reduced scattering coefficients of each material. In Figure 3.3 and 3.4, six wavelengths are marked with dotted lines. These marks indicate the wavelengths in which fat (blue dotted lines) and water (orange dotted lines) have their main absorption peaks.

In Figure 3.3 and 3.4, the DRS spectra of the fresh porcine adipose and muscle tissue as well as different types of *in vitro* human tissue (adapted from [92]) are visible. In Figure 3.3 top boxes, the spectrum of the porcine adipose tissue (which simulates the breast adipose tissue) and human adipose tissue, show a sharp dent on 1211 nm and a flat dent between 1393 nm-1453 nm. The absorption coefficients of both human and porcine adipose in Figure 3.4 displays a peak at 1211 nm and a flat and higher peak between 1400 nm and 1500 nm as well. On the contrary, the human tumor tissue (red) and porcine muscle spectrum shows a wider flat dent close to 1200 nm and becomes almost zero at 1400 nm and onward. In Figure 3.4, the absorption of the human tumor tissue and porcine muscle shows a lower flat peak at 1200 nm area and a very high and sharp peak at 1453 nm, which corresponds to water absorption. As shown in Figure 3.4, reduced scattering of all adipose tissues (human and porcine) is higher than reduced scattering of muscle (porcine) or tumor (human) tissue in all wavelengths.

The DRS spectra of all Adipose phantoms show one sharp dent around 1200 nm (at 1211 nm) and one flat dent around 1400 nm. Furthermore, the intensity remains more than zero in all wavelengths (same as porcine adipose tissue). Meanwhile, the absorption profile of the Adipose phantoms shows the same lower sharp peak on 1211 nm as well as the higher flatter peak between 1400 nm and 1500 nm, same as the porcine adipose tissue and human *in vitro* adipose tissue.

Like porcine muscle and human tumor tissue, the DRS spectra of the Tumor phantom shows flat dents around 1200 nm and 1400 nm (almost zero). The absorption profile of the Tumor phantoms also represents the same flat peak around 1200 nm and a sharp peak on 1453 nm, the same as muscle tissue (porcine) and tumor tissue (*in vitro*, human).

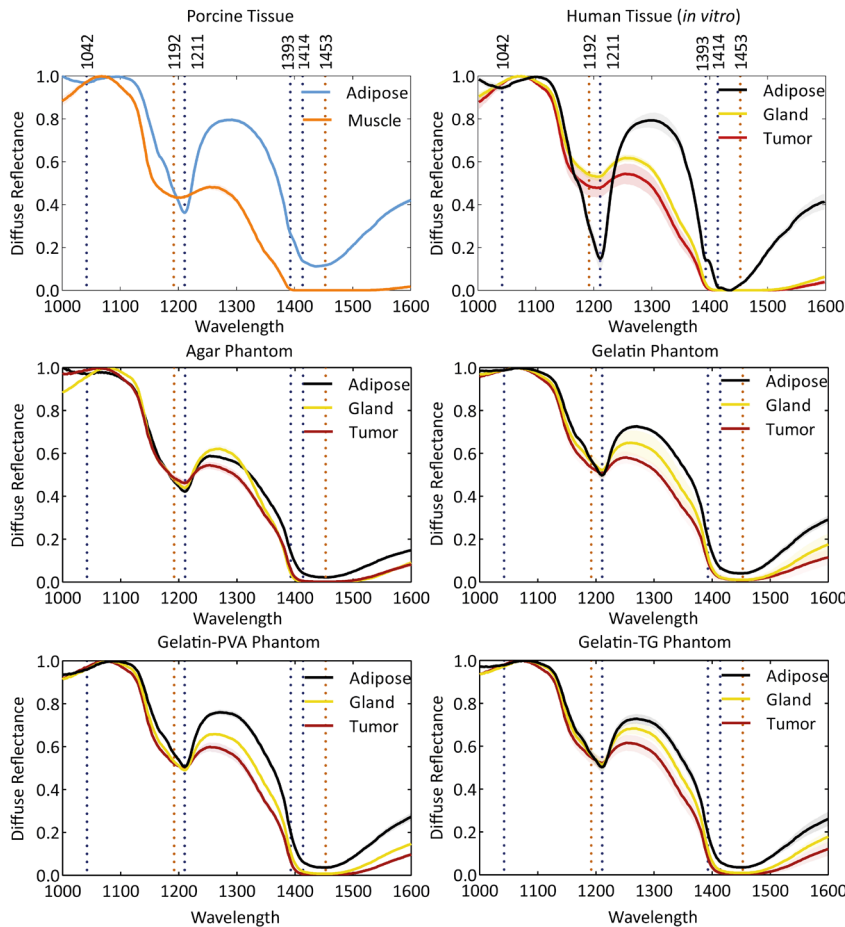


**Figure 3.3.** DRS measurements taken from porcine tissue, human breast tissue from four different phantoms. The DRS data of human breast tissue is adapted from [92].

In between, all the Gland phantoms show DRS spectra similar to the spectra of the human *in vitro* gland. The Gland spectra for all TMMs and *in vitro* human tissue is between the spectra of the Adipose and Tumor phantoms with DRS dents not as sharp as Adipose tissue and not as flat as Tumor tissue. The spectra of Agar phantoms in Figure 3.4 indicate similar reduced scattering for Adipose, Gland and Tumor tissue. For the Gelatin and Gelatin-PVA phantom, the reduced scattering of the Adipose phantom is higher than Tumor and reduced scattering of the Gland is in between those. For the Gelatin-TG phantom, the Adipose and Gland reduced scattering is almost the same after

1200 nm. The overall absorption and reduced scattering of the Gelatin phantoms are less than other phantoms.

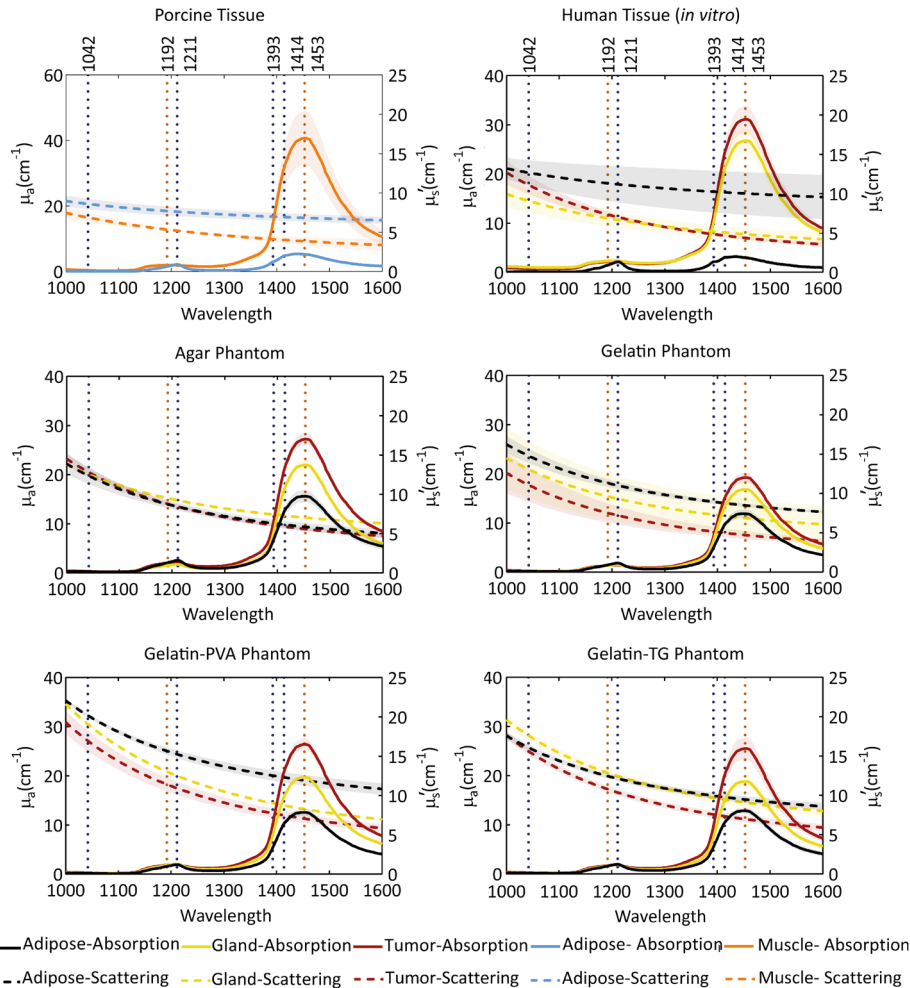


**Figure 3.4.** Absorption ( $\mu_a$ ,  $\text{cm}^{-1}$ ) and reduced scattering ( $\mu_s'$ ,  $\text{cm}^{-1}$ ) coefficient of porcine tissue, human tissue (in vitro) and each tissue mimicking materials. The DRS data of human breast tissue is derived from [90].

In general Gelatin-PVA phantoms seem to have a lower SD which shows that the phantoms are more homogenous, also within a phantom (different locations) as well as between phantoms replicates. The absorption spectra of all Tumor phantoms show a lower peak in 1453 nm in comparison with the muscle tissue and *in vitro* human Tumor

tissue. In addition, the height of the absorption peaks of the Adipose phantoms is close to the human adipose tissue, as well as those reduced scattering. In Table 3.2 and Figure 3.5, the reduced scattering coefficients of porcine tissue, human *in vitro* samples and each TMM at 1000 nm and 1200 nm wavelength are listed. The reduced scattering of human adipose tissue has higher deviations ranging from around 10 to 15  $\text{cm}^{-1}$ . Agar adipose phantom has the closest reduced scattering to the human adipose tissue at 1000 nm and to the porcine adipose tissue at 1200 nm, in comparison to other phantoms.

**Table 3.2.** Reduced scattering coefficient ( $\mu_s, \text{cm}^{-1}$ ) at 1000 nm and 1200 nm

Wavelength		Type of the tissue		
		Gland		
		Adipose	(fibroglandular tissue)	Tumor
<b>Porcine tissue</b>	1000 nm	8.96 $\pm$ 0.71	-	7.48 $\pm$ 0.79
	1200 nm	7.67 $\pm$ 0.56	-	5.28 $\pm$ 0.09
<b>Human tissue (<i>in vitro</i>)</b>	1000 nm	13.17 $\pm$ 1.37	9.91 $\pm$ 1.70	12.61 $\pm$ 1.51
	1200 nm	11.26 $\pm$ 2.26	6.76 $\pm$ 0.99	7.20 $\pm$ 0.38
<b>Agar Phantom</b>	1000 nm	13.88 $\pm$ 1.32	13.81 $\pm$ 0.31	14.53 $\pm$ 0.73
	1200 nm	8.60 $\pm$ 0.50	9.39 $\pm$ 0.20	8.62 $\pm$ 0.30
<b>Gelatin Phantom</b>	1000 nm	16.23 $\pm$ 1.11	14.49 $\pm$ 3.90	12.58 $\pm$ 2.56
	1200 nm	11.18 $\pm$ 0.48	9.49 $\pm$ 2.92	7.37 $\pm$ 1.18
<b>Gelatin-PVA Phantom</b>	1000 nm	22.07 $\pm$ 0.26	21.65 $\pm$ 0.34	19.33 $\pm$ 1.47
	1200 nm	15.48 $\pm$ 0.47	12.81 $\pm$ 0.06	11.21 $\pm$ 0.84
<b>Gelatin-TG phantom</b>	1000 nm	17.58 $\pm$ 0.46	19.60 $\pm$ 0.61	17.66 $\pm$ 0.53
	1200 nm	12.31 $\pm$ 0.33	12.69 $\pm$ 0.50	10.60 $\pm$ 0.41

On the other hand, at 1200 nm, Gelatin and Gelatin-TG adipose tissue simulate the reduced scattering of the human adipose tissue more closely. Moreover, Tumor mimicking material of Agar and Gelatin phantom also showed almost the same reduced scattering coefficient as the human tumor tissue and porcine muscle tissue. Adding PVA and TG to the Gelatin phantom resulted in higher reduced scattering numbers. The reduced scattering of both phantoms at 1000 nm are higher than the reduced scattering

of human tissue but in higher wavelengths, such as 1200 nm, the reduced scattering of these phantoms get closer to the targeted human tissue.

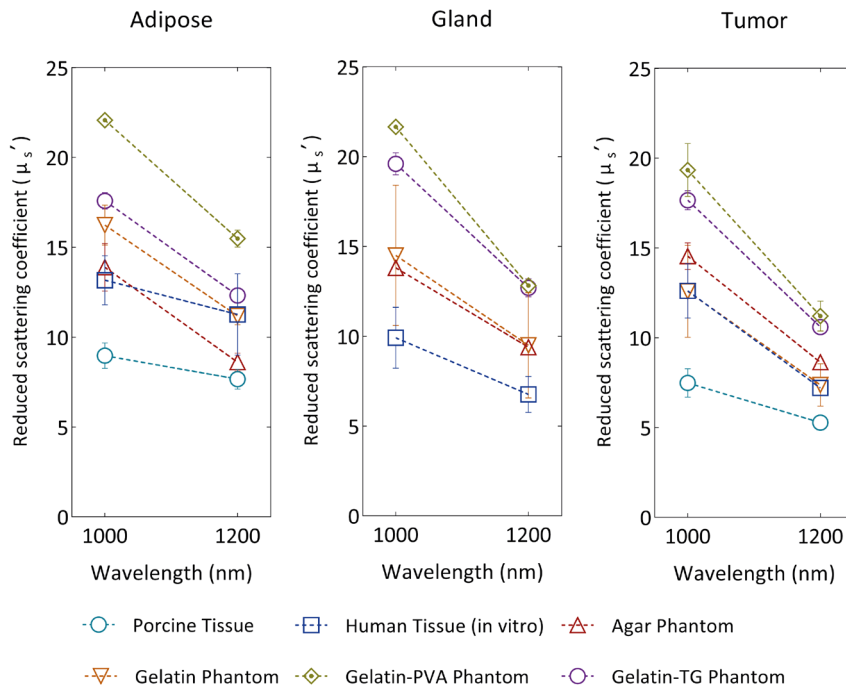


**Figure 3.5.** Reduced scattering ( $\mu_s'$ ,  $\text{cm}^{-1}$ ) at 1000 nm and 1200 nm for porcine tissue, in vitro human breast tissue and each. TMMs.

By using the software mentioned before, the fraction of fat and water was extracted from the DRS measurements for all phantom materials and subsequently, the F/W-ratio was calculated, as shown in Figure 3.6. The float box plots in Figure 3.6 show the mean, minimum and maximum of the Fat%, Water% and F/W-ratio. For all Adipose phantom materials, the Fat% is higher than 60%. The Fat% for the Gelatin-PVA phantom has the closest minimum to maximum, so the boxplot became smaller. Fat percentages among the Adipose, Gland and Tumor phantom materials of all phantoms have no overlap. This applies also to Water% and Fat/Water-ratio. From all the Adipose phantoms containing gelatin, the Adipose Gelatin phantom shows the highest Fat% and F/W-ratio. All phantoms show a clear distance between the F/W-ratios of the different layers.

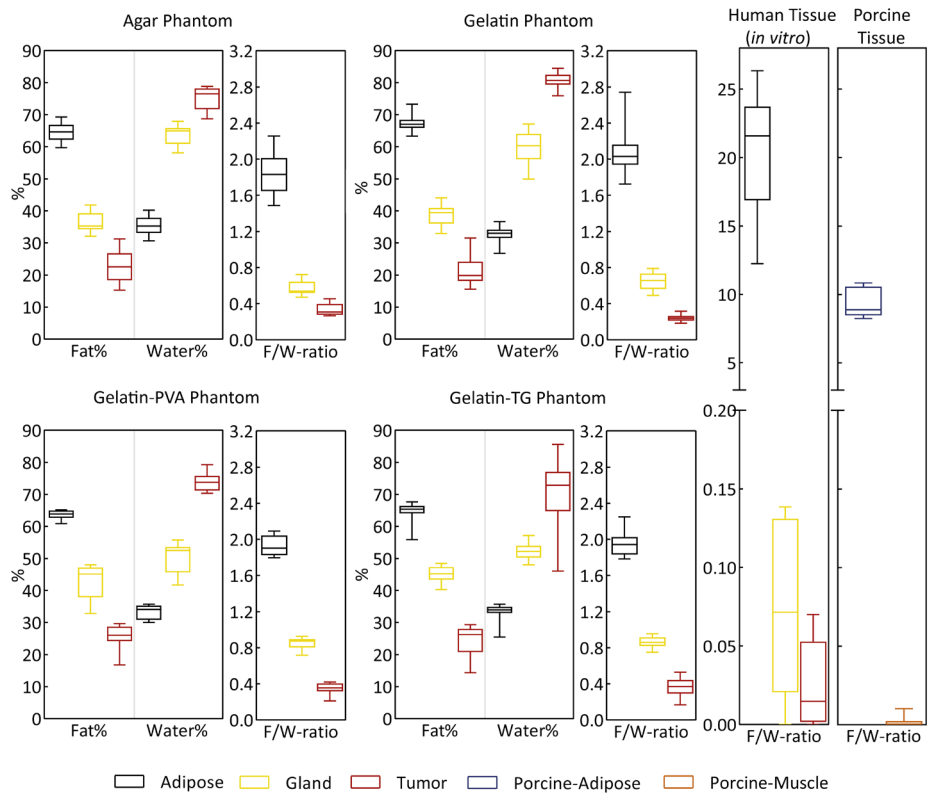


**Figure 3.6.** The Fat%, Water% and calculated F/W-ratio for each phantom extracted from the DRS measurements, boxes showing the min to max of the parameter along with its mean value (line inside the box).

### 3.3.2 Electrosurgery

One hour after removing the phantom materials from the fridge, they were cut with the electrosurgical knife using 60 W. Figure 3.7 displays the pictures taken from each phantom after being cut. Similarly, to porcine adipose and muscle tissue, melting and burning occurred when cutting the phantoms with the electrosurgical knife. The Adipose phantoms and porcine adipose tissue showed the most melting whilst the Tumor phantoms and porcine muscle tissue showed the least melting. Among the phantoms, Gelatin and Gelatin-PVA melted the most and Gelatin-TG melted the least. Burning effects and char production were clearly visible on the Gelatin-PVA and Gelatin-TG phantoms. From the phantoms, the Adipose Gelatin-PVA and Adipose Gelatin-TG resembled the electrosurgical effects (melting and burning) to the porcine adipose tissue

the most. Finally, cuttings on the Tumor Agar and Tumor Gelatin-TG phantoms were most similar to cuttings on the porcine muscle tissue.

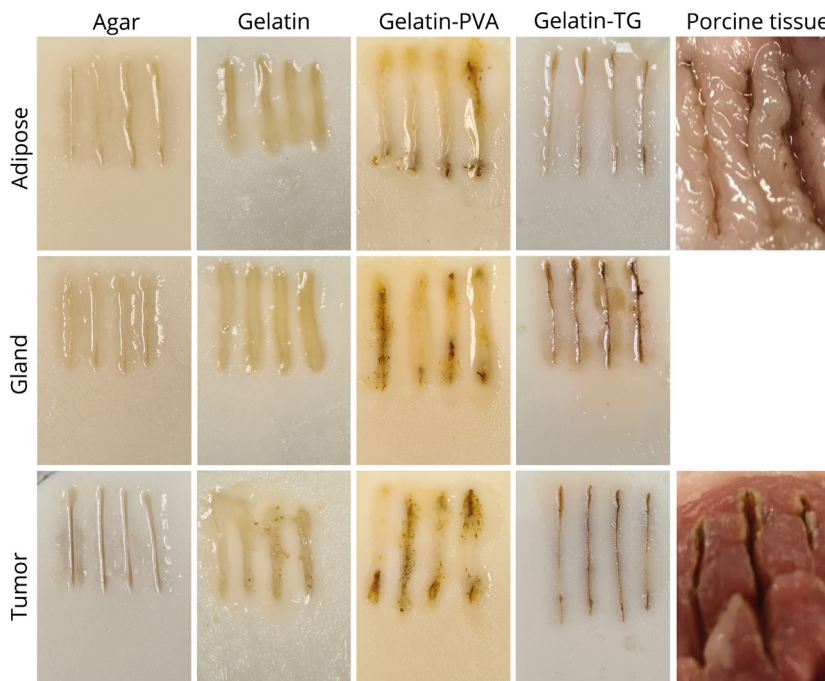


**Figure 3.7.** The effect of electrosurgery on the tissue phantoms.

### 3.3.3 Stability over time

To investigate how the phantom composition and optical properties would change over time, DRS measurements were carried out on all phantoms on day 10 after production. The F/W-ratio of all phantoms at day 1 and day 10 are shown in Figure 3.8. The F/W-ratios for most phantoms increased after 10 days. The difference between the F/W-ratio at day 1 and day 10 for all Agar phantom and Gelatin phantom materials were significant. For Gelatin-PVA and Gelatin-TG there was not a significant difference between the F/W-ratio of day 1 and day 10 of the Adipose layers and Gland layers, while for the Tumor phantom the difference with one star was seen. Although time significantly changes F/W-ratios of most phantoms, there is still a significant difference in F/W-ratio between the Adipose, Gland and Tumor phantom materials (none of the phantoms' F/W-ratios overlap).

Additionally, a visual inspection of the phantom materials after three weeks was carried out. All Agar phantoms and Gelatin-PVA phantoms (different layers in replicates) were intact, there was no sign of mold or size reduction. On the other hand, small mold colonies were formed on the surfaces of the Gelatin phantoms without any change in the size of the phantoms. Finally, concerning the Gelatin-TG phantoms, deformation occurred, and molds were formed all over the phantoms.

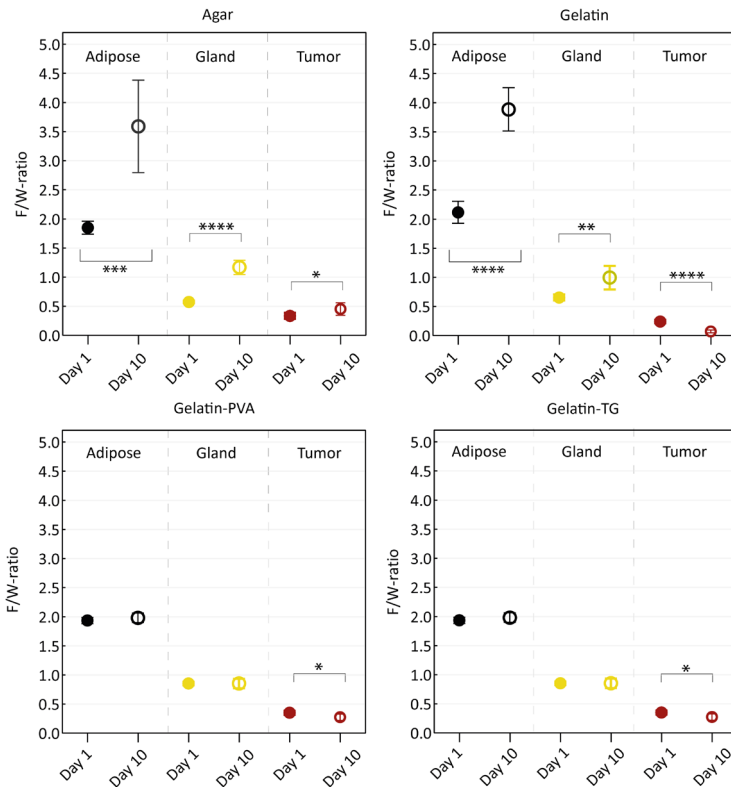


**Figure 3.8.** F/W-ratio between the phantoms on day 1 and day 10 from the production (\*: p-value<0.05, \*\*:p-value<0.01, \*\*\*:p-value<0.001, and \*\*\*\*: p-value<0.0001).

### 3.3.4 Breast phantom production

The breast phantoms were made following the production steps mentioned in Figure 3.9. Using silicone molds, it was possible to produce tumors in different shapes (with round edges or star-like shapes) and sizes (with a diameter of 0.5 cm to 4 cm) (Figure 3.9(d)). After removing the gland mold (Figure 3.9(b)), visible in Figure 3.9(C), the gland cavity was made and then along with the tumors in it, it was filled with gland

materials (Figure 3.9(E)). In the end, a realistic breast phantom containing tumors in different shapes and sizes were produced (Figure 3.9(F)). The presence of the silicone layer allowed the easy detachment of the phantom from the mold. Moreover, the silicone layer was colored with a skin-like silicone-based color to represent the appearance of the skin layer (only visually, no optical characterization has been done on the silicone layer). In further studies, this layer can be removed from the phantom if needed.

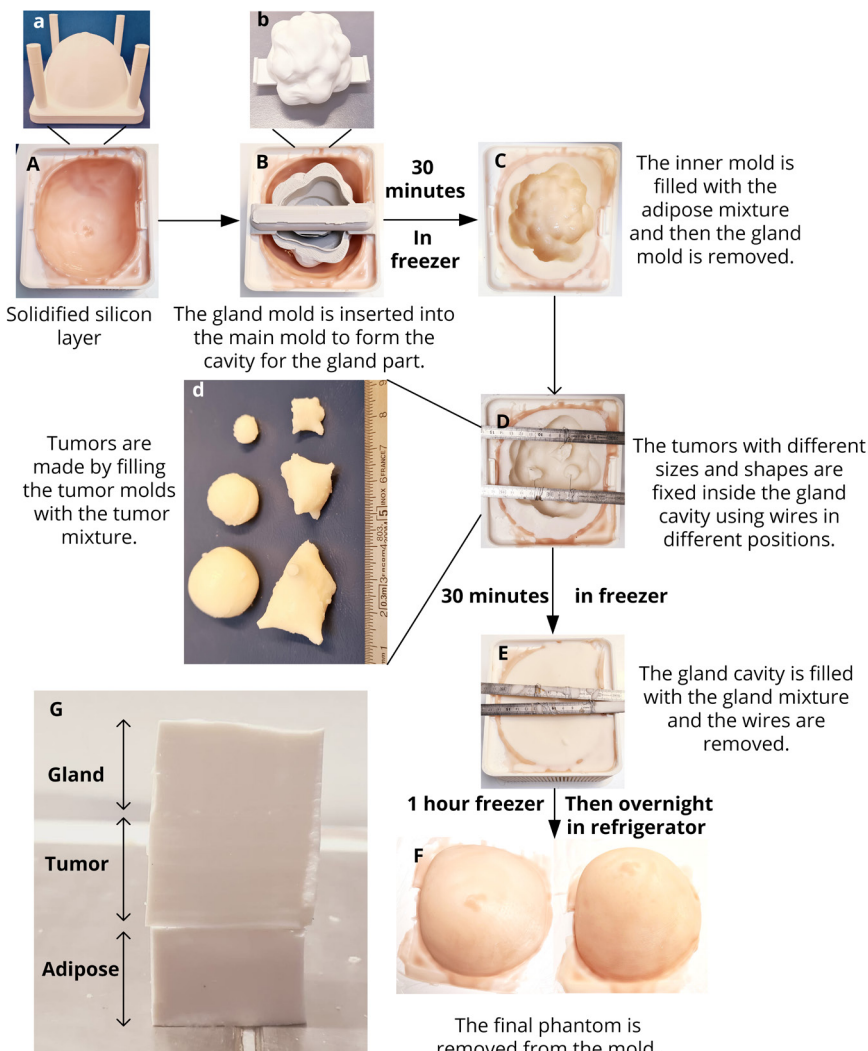


**Figure 3.9.** (A-F) Production of the final breast phantom. (G) The layered phantom consists of Gland, Tumor and Adipose layers.

Moreover, Figure 3.9(G) shows a layered phantom with layers of Gland, Tumor and Adipose (respectively from top to bottom) made of Gelatin-TG TMMs. These layers have similar colors and textures, and distinguishing them from each other is challenging with the unaided eye. Considering the DRS and electrosurgical results, the Gelatin phantom was removed from the list of final phantom production as this phantom showed less suitable properties (less optical homogeneity, higher melting, and less stability over time) in comparison to other phantoms.

### 3.3.5 X-ray image of the phantoms

X-ray images were taken using the Allura system (Philips Healthcare, Best, The Netherlands) from the three chosen final breast phantoms (Agar phantom, Gelatin-PVA phantom and Gelatin-TG phantom). Figure 3.10 shows the side and top view of the phantoms as well as its 3D rendering with the inserted tumors. The images show successful insertion of the tumors and other layers of the phantoms.

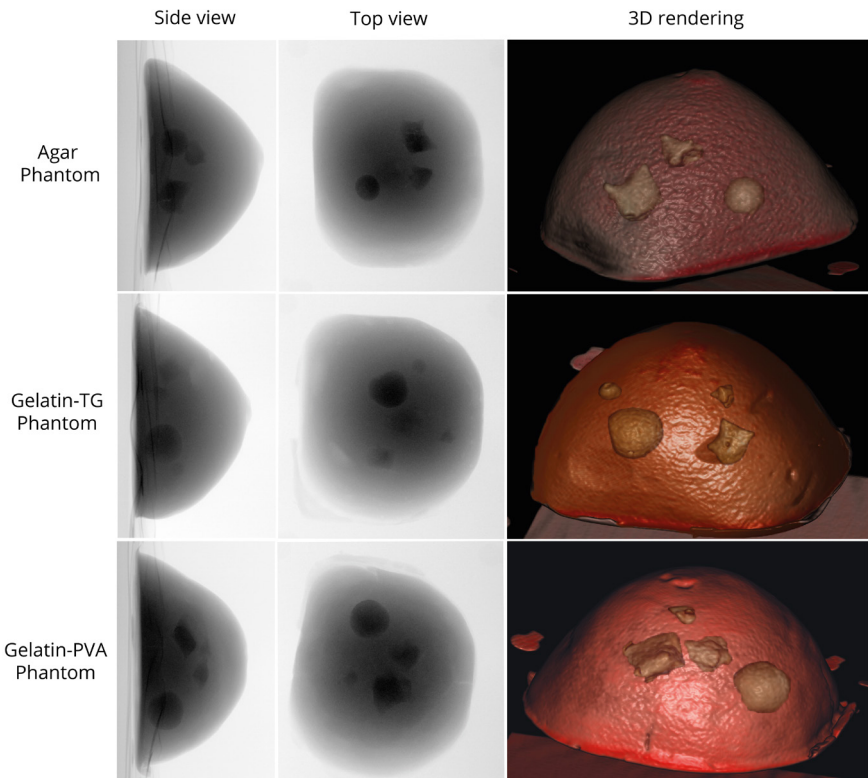


**Figure 3.10.** X-ray images of the final phantoms.

In all phantoms, the tumors were clear and visible due to the addition of the barium sulfate. The gland and adipose layer of the Gelatin-PVA phantom are clearly distinguishable from each other due to the difference in color, namely a darker color for the gland layer and a light grey color for the adipose layer. For the two other phantoms, the gland layer is only a little bit darker than the adipose layer but a clear margin for this layer is not visible.

### 3.4 Discussion

Fat-water based tissue-mimicking materials (TMM) and phantoms based on gelatin or agar with different recipes were developed in this work. The main purpose of developing such phantoms is to simulate the physiological composition of human breasts in different layers including tumors to assess the capability of the optical imaging systems, namely diffuse reflectance spectroscopy, in detecting the tumor during breast conserving surgery. To achieve this objective, phantoms were produced that represent the optical properties of the different layers of human breasts by controlling the amount of the lipid and water of the TMM as the main constituent of human tissue, specifically, women breast tissue.

Agar and gelatin were used as a fat and water emulsifier as well as a gelling and coagulant agent to solidify the mixture. Additionally, the effect of adding polyvinyl alcohol (PVA) (Gelatin-PVA phantom) and transglutaminase (Gelatin-TG phantom) to the optical properties of the TMM and its stability during electrosurgery were investigated. The development process of all phantoms was time and cost-efficient and all the produced phantoms were stable at room temperature and easily moldable.

The results of the DRS measurements showed that the main absorption and reduced scattering profile of each TMM was similar to the target tissue. De Boer et al. investigated the spectral profile of different locations on sixteen specimens of lumpectomy samples to find the robust discriminative parameter between healthy tissue and tumor tissue in the NIR part using DRS [21]. They showed that for all samples, the F/W-ratio of all healthy locations was higher than a certain threshold, while for all tumor locations this parameter was lower than the threshold. Moreover, in almost all samples the F/W-ratio clearly decreased when moving from the healthy tissue to the border of the tumor tissue. They showed that by using a threshold for the F/W-ratio, it is possible to make a safe surgical plan to remove the tumor from the breast of the patient using DRS as an intra-operative

---

margin assessment technique. This patient-specific F/W-ratio threshold, can be measured at the beginning of the surgery [21].

In another research, De Boer et al. also studied the effectiveness of DRS in an *in vivo* setup using a biopsy needle integrated with DRS optical fibers [24]. They showed that classification of the measurements based on F/W-ratio, results in healthy-tumor discrimination with mean sensitivity and specificity of 0.71 and 0.99, respectively. They could also classify the tissues correctly with high sensitivity and specificity (more than 0.91) using DRS measurements in some specific wavelengths. These specific wavelengths are in the wavelength range that is related to the main absorption of fat and water. These specific wavelengths are mostly in the range of 1000-1600 and that is why this wavelength range is used in this research, as the amount of fat and water is the main discriminating parameter between the malignant and healthy tissue of the breast. Moreover, at the surgical site blood contamination can decrease the reliability of the measurements at the visible part of the spectra (400-800) [24].

It has been shown that using a higher wavelength range of spectra can result in more precise tissue classification [21, 24]. From the calculated Fat%, Water% and F/W-ratio of the produced TMMs (shown in Figure 3.6) it is possible to consider a clear F/W-ratio threshold not only between the adipose and fibroglandular layer, but also between the tumor layer and both adipose and fibroglandular layer for all phantoms. Furthermore, the shape of the DRS spectra of the TMMs produced in Figure 3.3. indicate a close similarity in the shape of the spectra between the TMM and its targeted *in vitro* human tissue and porcine tissue. Indeed, the shape of the spectra of the TMMs in this work is in accordance with the spectra of the healthy and tumor tissue of the breast measured by De Boer et al. [22, 24]. The developed TMMs in this work could closely simulate the absorption and scattering profile of the human breast tissue. Therefore, similar to the human breast tissue [21], we can find a specific F/W-ratio that can be used as a threshold for discriminating healthy tissue phantom material (adipose and fibroglandular layer) from malignant tissue phantom material (tumor layer). Thereupon, we can create a surgical plan to detect the border of the tumor using DRS and remove it from the heterogeneous breast phantom using the electrosurgical knife.

Among all phantoms, Agar phantoms had a scattering profile closer to human breast tissue at 1000 nm while at 1200 nm, Gelatin-phantoms could represent reduced scattering coefficient closer to the human breast tissue. Taroni et al. showed reduced scattering close

to  $10\text{ cm}^{-1}$  for the breast tissue [95]. Yoshizawa et al. showed that breast tissue has reduced scattering between  $5\text{--}15\text{ cm}^{-1}$  at  $795\text{ nm}$  [96]. Moreover, Nachabe et al. showed that in the breast the reduced scattering amplitude at  $800\text{ nm}$  is around  $5$  to  $10\text{ cm}^{-1}$  depending on the type of the tissue [23]. De Boer et al. also determined that the reduced scattering at  $800\text{ nm}$  for breast tissue (normal and malignant) ranges from around  $5\text{ cm}^{-1}$  to  $60\text{ cm}^{-1}$  [21]. Furthermore, Evers et al. measured reduced scattering from less than  $5\text{ cm}^{-1}$  to around  $20\text{ cm}^{-1}$  for different tissue of the breast at  $800\text{ nm}$  [92]. In this research the approximate reduced scattering for all phantoms are in the range of  $10$  to around  $20\text{ cm}^{-1}$  at  $1000\text{ nm}$ , which is in accordance with Taroni et al [95] and De Boer et al. [21] and the mentioned measurements form work of Evers et al [92] in which a higher wavelength range was used to measure the spectral response of the human breast tissue. The reduced scattering profile of the Gland and Tumor layer is similar to the reduced scattering profile of the porcine muscle tissue and *in vitro* human adipose tissue. Besides, the slight differences between the DRS spectra of the Adipose layer and the porcine adipose tissue can be due to the lower amount of fat in the Adipose layer (60% fat) than the porcine adipose tissue (more than 90% fat). The reduced scattering of the Gland phantoms for all the composition is not matching exactly with the reduced scattering of the fibroglandular layer of human *in vitro* tissue which is due to the fact that the Fat% of the human fibroglandular tissue is lower than 40% (Figure 3.6). Accordingly, reaching to the same scattering of fibroglandular layers is easily possible through adjusting the amount of the fat of the Gland layer of the TMM materials. Another point to consider regarding the optical properties of the developed TMMs is the effect that the addition of the barium sulfate (as an X-ray contrast agent) might have on the DRS outputs of the Tumor phantoms. The application of Barium Sulfate ( $\text{BaSO}_4$ ) as a reflection standard, due to its high reflectivity (average of 92%) in the range of  $173\text{--}2500\text{ nm}$ , have been extensively studied [97]. It is known that the Mie reduced scattering slope (in equations explained in Figure 3.2(B)) correlates with the particle size. Adding barium sulfate to the mixture can change the average particle size of the mixture and subsequently is reduced scattering [91, 97]. Most of the barium sulfate containing Tumor TMMs developed in this research (more specifically Agar and Gelatin phantom) could closely simulate the reduced scattering coefficient of the human breast tumor tissue in higher wavelengths ( $1000\text{ nm}$  and  $1200\text{ nm}$ ). The F/W-ratio of the tumor phantoms were also in the expected range based on the production recipe in which fat and water were used with the ratio of 20:80 (20 ml fat, 80 ml water). However, understanding the extent to which the addition of the

---

barium sulfate can affect the reduced scattering coefficient and the measured F/W-ratio of the material can be the subject of further studies.

Performing electrosurgery on all phantom materials was possible, and based on the qualitative inspections, TMMs showed similar effects as electrosurgery on porcine tissue. Adank et al. [32] showed that the coagulated area produced by cutting porcine tissue with the electrosurgical knife can alter the characteristics and affect the optical properties of porcine tissue. In their research, they showed that by increasing the power of the electrosurgical knife, reduced scattering will increase which results in overestimation of the fat fraction. To simulate realistic BCS for assessing spectral sensing systems such as DRS, it is required to consider the same electrosurgical effects for the phantoms materials. Among all phantoms, electrosurgery on the Gelatin phantom showed the least similarity in electrosurgical tissue effects (melting and burning) compared to the porcine tissue, which is due to the unstable character of gelatin in high temperatures. Among the other phantoms, the Gelatin-TG phantom resembled the electrosurgical tissue effects of porcine tissue the best. While all phantoms demonstrated electrosurgical tissue effects sufficiently similar to porcine tissue, more DRS studies are required to quantify the electrosurgical effects on the phantoms so that the electrosurgical tissue effects can be more accurately simulated in the future. Although producing a visually tissue-like electrosurgery effect was achievable using the developed TMMs, further studies are required to quantify this similarity. In an in-depth evaluation of the electrosurgery effect on TMMs, DRS spectra can be taken from the intact and then affected sites (cut or coagulated tissue) of phantom and *ex vivo* animal or human tissue. The results can then be compared to determine the quantitative similarity between the TMMs and human/porcine tissue regarding the electrosurgery effect.

It is also important to note that although the TMMs were produced to be used in electrosurgery applications, this research does not focus on the extent to which the TMMs can be quantitatively similar to human/porcine tissue in terms of electrical conductivity. The majority of these phantoms are used in the process of assessment and calibration of the detecting/imaging systems that work based on the electrical characteristics of the tissue, such as impedance spectroscopy and microwave imaging systems [98, 99]. Due to the similar composition of the TMMs and breast tissue (both contain mostly fat and water), it is expected that these TMMs could (be modified to) have electrical properties similar to the human tissue. To show this, more comprehensive and quantitative

assessment of the dielectric characteristics of the TMM is required, especially when they are intended for the applications in which measuring electrical properties of the TMMs are desired. In comparison to the other phantoms, DRS measurements of Gelatin-PVA and Gelatin-TG showed superior stability after 10 days of production. Concerning PVA, it has been shown that the physical crosslinking of the gelatin-PVA mixture can improve the mechanical properties of the final hydrogel [75]. Furthermore, Liu et al. showed that adding gelatin to PVA has no significant effect on the thermal behavior of PVA. This explains why adding PVA to the gelatin phantom (Gelatin-PVA) did not affect the electrosurgical effect of it, namely melting rather than burning effects were seen on the material [73]. Additionally, enzymatic crosslinking of gelatin using TG can increase the thermal stability and mechanical properties of the final product [100], which clarifies the decrease in melting of the phantom material with electrosurgery and the improved electrosurgical effect of the Gelatin-TG phantom in comparison to the Gelatin-Phantom.

It is noteworthy that the enzymatic crosslinking of gelatin in the Gelatin-TG phantom inhibits the water loss and increases the water detention and stability of the phantom, which is consistent with the results of other studies [101]. More research could be done in this area to measure the exact amount of water loss for each phantom. The increase of the F/W-ratio in the Agar and Gelatin phantom is due to the water loss after 10 days. Because of the increased cross-linked network of the Gelatin-PVA and Gelatin-TG phantom, the water loss after 10 days was lower in these two phantoms, which resulted in a more stable F/W-ratio over time. Although the difference between the F/W-ratio of the tumor phantom material between day 1 and day 10 in Gelatin-PVA and Gelatin-TG was significant with one star (\*: p-value<0.05), there is still a clear threshold between the F/W-ratio of the Tumor and Gland/Adipose layer, which enables the correct tissue classification using DRS. Based on the results of this research, the Gelatin-PVA and Gelatin-TG phantom can be still used for the intended application, even after 10 days after the production. Although using PVA and TG could increase the stability of the TMM material, the increased scattering of the TMM due to their presence can negatively affect their applicability for our application. However, using a more robust stirring system such as syndicators or powerful kitchen blenders instead of the magnetic stirrer can help for having a more homogeneous blend with finer particles especially for the TG phantom which can result in lower reduced scattering numbers [37].

The pure lard which was used in this research contained no additives, while some lards that are available commercially may contain additives such as antioxidants that might alter the characteristics (optical, electrosurgery effect or other properties such as stability over time) of the final product [102]. The composition of the lard (percentage of each fatty acid) can vary depending on the animal's diet and the anatomical source of the lard. It has been shown that different components of the fatty acids have only a slight effect on the near-infrared absorption profile of the materials [41, 103]. Furthermore, although during the production of the TMMs, lard from different batches (all batches were from the same butcher and animal organ but from different purchases) were used, no significant differences were seen between the optical profile (Figure 3.3, 3.4 and 3.5) or fat-water content (Figure 3.6) of the three replicates of each phantom (phantoms with same compositions). Nevertheless, further studies should be carried out to examine the effect of the lard's source on the final properties of the TMMs.

The TMM production method developed in this study can be used to produce materials with adjustable optical properties based on water and fat. The development of such methods and TMMs requires performing many experiments, which can lead to the use of large quantities of raw materials. Moreover, one of the aims of this research was to produce cost-efficient TMMs since the final products are intended to be used during electrosurgery, which results in the destruction of the phantom. Therefore, during the development of the TMMs, food-grade agar and gelatin were used to reduce the costs of the final product and produce a more cost-effective phantom recipe. Further studies can be done to comprehend the effect of using different agar or gelatin on the properties of the TMMs. The use of high quality and precisely processed agar and gelatin from scientific suppliers such as Sigma-Aldrich (Sigma-Aldrich, United States) in further studies may result in more reliable and reproducible phantoms, which in turn increases the costs of the final product.

Finally, the phantom materials were used to form anatomically-relevant breast phantoms for assessing breast imaging systems such as DRS. Moreover, the similar color and texture of the layers would make it difficult to detect the tumor borders surrounded with either Adipose or Gland TMMs, same as the situation that surgeons deal with during breast conserving surgery. The silicone layer, which could easily be removed from the phantom, was mainly used to ease the production process of the phantom and represent

the appearance of the skin. No optical or any other characterization was done on this layer.

Although the application of DRS in the detection of breast tumors has been studied vastly, the capability of DRS in real-time detection of the tumor border, while moving the probe along the different layers of the breast tissue during the electrosurgery, has not yet been fully researched. Phantom studies can accelerate the adaptation of the DRS into clinical practice. In future studies, incisions in these anthropomorphic breast phantoms containing tumors can be made with the aim of simulating the intraoperative use of the DRS probe and electrosurgical knife in the detection and extraction of the tumors. The tumors containing Barium sulfate are clearly visible in the X-ray images, which enables to study of the performance of the intraoperative margin detection system after performing a BCS on the phantom. It is important to point out that in developing the TMMs, no action has been taken for quantitative simulation of the mechanical properties of the tissue. Although the application of hydrogel-based TMMs made it possible to develop soft phantoms, further studies and research are required to characterize and modify the mechanical properties of the phantoms for more quantitative simulation of breast tissue.

Table 3.3 summarizes the pros and cons of each developed TMMs for the intended application in this chapter. While each TMMs developed in this research has its advantages over other phantoms, based on the results of this research and the discussed points, Agar phantom and Gelatin-TG phantom can better fulfil the requirements mentioned earlier and can be useful in applications that include optical measurements and electrosurgery.

An ideal phantom intended to be used in assessing intraoperative tumor margin detection techniques, requires to be electrically conductive, since in most cancer surgeries, such as BCS (lumpectomy) and liver cancer, the electrosurgical knives will be used to cut out malignant tissue. However, developing such a phantom material meant for both applications (assessing the tumor detection technique while enabling electrosurgery) have not sufficiently been explored yet. To the best of our knowledge, this is the first fat-water based breast phantom used for optical measurement in the range of 1000-1600 nm which is also intended for electrosurgery. Hence, it seems there is still room for additional research regarding the production of such phantom materials. These phantom materials should have features that enable realistic simulation of the workflow during

surgery/diagnosis either to validate, optimize and calibrate the margin detection technique or to train the medical residents and surgeons, as close as possible to reality.

**Table 3.3.** Summarizing the pros and cons of each tissue mimicking phantom material

Phantom	Pros	Cons
Agar	DRS spectra similar to the human breast tissue closely simulating the absorption and scattering profile of the human breast tissue in NIR wavelength range  No excessive melting during electrosurgery	No burning effect during electrosurgery unlike tissue  Low stability of optical properties after 10 days of storage
Gelatin	DRS spectra similar to the human breast tissue  Closely simulating the scattering profile of the human breast tissue in NIR wavelength range  Ease of manufacturing process	Excessive melting during electrosurgery  Low stability of optical properties after 10 days of storage
Gelatin-PVA	DRS spectra similar to the human breast tissue  High stability of optical properties after 10 days of storage	Melting during electrosurgery (rather than burning)  Higher reduced scattering coefficients due to the use of PVA  Complicated manufacturing process
Gelatin-TGA	DRS spectra similar to the human breast tissue  High stability of optical properties after 10 days of storage  Tissue-like electrosurgery effect	Higher reduced scattering coefficients due to the use of TG

As mentioned before, developing a physiologically relevant breast phantom representing the fat and water content of breast tissue is essential to evaluate the performance of the spectral imaging system in estimating the constituents of breast tissue. The results of this research show that using fat-water based TMMs, enable the simulation of human breast tissue's absorption and reduced scattering coefficient closely. Additionally, these type of phantoms can be used to assess other types of imaging systems that aim to measure the fat and water content of breast tissue for diagnostic or therapeutic purposes. For instance, these fat-water phantoms can be used for the assessment of X-ray and MRI imaging systems in the evaluation of the breast density, detection of lesions [70,

104-106], or the assessment of Microwave imaging systems [61-63, 65-67], or hybrid imaging techniques [68], or the assessment of therapeutic systems such as pulsed electric field [107].

### **3.5 Conclusions**

In this study, tissue-mimicking materials with tunable optical properties were developed mainly based on water and porcine fat (lard). The developed phantom materials were produced in such a way that they could be cut using electrosurgical instruments, and as a result, they can be used to simulate surgeries in which an electrosurgical knife is used to remove the tumors. These tissue-mimicking phantom materials can be used to simulate the performance of optical-based imaging systems in detecting the breast tumor before moving to clinical trials.

## Bibliography

- [1] E. R. Sauter, "Breast cancer prevention: current approaches and future directions," *European journal of breast health*, vol. 14, no. 2, pp. 64-71, 2018.
- [2] C. E. DeSantis *et al.*, "Breast cancer statistics, 2019," *CA: a cancer journal for clinician*, vol. 69, no. 6, pp. 438-451, 2019.
- [3] C. Chiappa *et al.*, "Surgical margins in breast conservation," *International Journal of Surgery*, vol. 11, pp. S69-S72, 2013.
- [4] D. W. Shipp *et al.*, "Intra-operative spectroscopic assessment of surgical margins during breast conserving surgery," *Breast cancer research*, vol. 20, no. 1, pp. 1-14, 2018.
- [5] C. M. O'Kelly Priddy *et al.*, "The importance of surgical margins in breast cancer," *Journal of surgical oncology*, vol. 113, no. 3, pp. 256-263, 2016.
- [6] E. Sadot *et al.*, "Resection margin and survival in 2368 patients undergoing hepatic resection for metastatic colorectal cancer: surgical technique or biologic surrogate?," *Annals of surgery*, vol. 262, no. 3, pp. 476, 2015.
- [7] M. S. Moran *et al.*, "Society of Surgical Oncology-American Society for Radiation Oncology consensus guideline on margins for breast-conserving surgery with whole-breast irradiation in stages I and II invasive breast cancer," *International Journal of adiation Oncology\* Biology\* Physics*, vol. 88, no. 3, pp. 553-564, 2014.
- [8] C. Reyna, and S. M. DeSnyder, "Intraoperative margin assessment in breast cancer management," *Surgical Oncology Clinics*, vol. 27, no. 1, pp. 155-165, 2018.
- [9] M. Pilewskie, and M. Morrow, "Extent and role of margin control for DCIS managed by breast-conserving surgery," *Ductal carcinoma in situ and microinvasive/borderline breast cancer*, pp. 67-83: Springer, 2015.
- [10] R. Jeevan *et al.*, "Reoperation rates after breast conserving surgery for breast cancer among women in England: retrospective study of hospital episode statistics," *Bmj*, vol. 345, pp. 1-9, 2012.
- [11] J. Landercasper *et al.*, "Reasons for re-excision after lumpectomy for breast cancer: insight from the American Society of Breast Surgeons Mastery SM database," *Annals of surgical oncology*, vol. 21, no. 10, pp. 3185-3191, 2014.
- [12] H. M. Kuerer *et al.*, "DCIS margins and breast conservation: MD Anderson Cancer Center multidisciplinary practice guidelines and outcomes," *Journal of Cancer*, vol. 8, no. 14, pp. 2653-2662, 2017.
- [13] B. L. Murphy *et al.*, "Factors associated with positive margins in women undergoing breast conservation surgery," in *Mayo Clinic Proceedings*, Year, pp. 429-435.
- [14] L. A. Newman, and J. M. Bensenhaver, "Ductal carcinoma in situ and microinvasive/borderline breast cancer", p.^pp. 171: Springer, 2015.
- [15] L. Jacobs, "Positive margins: the challenge continues for breast surgeons," *Annals of surgical oncology*, vol. 15, no. 5, pp. 1271-1272, 2008.
- [16] R. J. Gray *et al.*, "Intraoperative margin management in breast-conserving surgery: a systematic review of the literature," *Annals of surgical oncology*, vol. 25, no. 1, pp. 18-27, 2018.
- [17] R. Nachabe *et al.*, "Estimation of lipid and water concentrations in scattering media with diffuse optical spectroscopy from 900 to 1600 nm," *Journal of biomedical optics*, vol. 15, no. 3, pp. 037015, 2010.

- [18] R. Nachabé *et al.*, "Estimation of biological chromophores using diffuse optical spectroscopy: benefit of extending the UV-VIS wavelength range to include 1000 to 1600 nm," *Biomedical optics express*, vol. 1, no. 5, pp. 1432-1442, 2010.
- [19] T. M. Bydlon *et al.*, "Chromophore based analyses of steady-state diffuse reflectance spectroscopy: current status and perspectives for clinical adoption," *Journal of biophotonics*, vol. 8, no. 1-2, pp. 9-24, 2015.
- [20] L. L. de Boer *et al.*, "Using DRS during breast conserving surgery: identifying robust optical parameters and influence of inter-patient variation," *Biomedical Optics Express*, vol. 7, no. 12, pp. 5188-5200, 2016.
- [21] L. De Boer *et al.*, "Fat/water ratios measured with diffuse reflectance spectroscopy to detect breast tumor boundaries," *Breast cancer research treatment*, vol. 152, no. 3, pp. 509-518, 2015.
- [22] L. L. de Boer, *Detecting breast cancer tissue with diffuse reflectance spectroscopy*, Enschede: University of Twente, 2019.
- [23] R. Nachabe *et al.*, "Diagnosis of breast cancer using diffuse optical spectroscopy from 500 to 1600 nm: comparison of classification methods," *Journal of biomedical optics*, vol. 16, no. 8, pp. 087010, 2011.
- [24] L. L. De Boer *et al.*, "Towards the use of diffuse reflectance spectroscopy for real-time in vivo detection of breast cancer during surgery," *Journal of translational medicine*, vol. 16, no. 1, pp. 1-14, 2018.
- [25] T. M. Bydlon *et al.*, "Performance metrics of an optical spectral imaging system for intra-operative assessment of breast tumor margins," *Optics express*, vol. 18, no. 8, pp. 8058-8076, 2010.
- [26] S. Kennedy *et al.*, "Optical breast cancer margin assessment: an observational study of the effects of tissue heterogeneity on optical contrast," *Breast cancer research*, vol. 12, no. 6, pp. 1-13, 2010.
- [27] L. L. de Boer *et al.*, "in vivo optical spectral tissue sensing—how to go from research to routine clinical application?," *Lasers in medical science*, vol. 32, no. 3, pp. 711-719, 2017.
- [28] J. W. Spliethoff *et al.*, "In vivo characterization of colorectal metastases in human liver using diffuse reflectance spectroscopy: toward guidance in oncological procedures," *Journal of biomedical optics*, vol. 21, no. 9, pp. 097004, 2016.
- [29] J. Spliethof, *Spectral tissue sensing for guidance and monitoring in oncological procedures*, Enschede: Universiteit Twente, 2015.
- [30] A. Keller *et al.*, "Diffuse reflectance spectroscopy of human liver tumor specimens—towards a tissue differentiating optical biopsy needle using light emitting diodes," *Biomedical optics express*, vol. 9, no. 3, pp. 1069-1081, 2018.
- [31] L. L. de Boer *et al.*, "Using DRS during breast conserving surgery: identifying robust optical parameters and influence of inter-patient variation," *Biomedical Optics Express*, vol. 7, no. 12, pp. 5188-5200, 2016.
- [32] M. W. Adank *et al.*, "Real-time oncological guidance using diffuse reflectance spectroscopy in electrosurgery: the effect of coagulation on tissue discrimination," *Journal of biomedical optics*, vol. 23, no. 11, pp. 115004, 2018.
- [33] S. A. Amiri *et al.*, "Electrosurgical knife equipped with diffused reflectance spectroscopy sensing for tumor margin detection during breast conserving surgery: a phantom study,"

in Advanced Biomedical and Clinical Diagnostic and Surgical Guidance Systems XIX, Year, pp. 1163110.

- [34] S. A. Amiri *et al.*, "Intraoperative tumor margin assessment using diffuse reflectance spectroscopy: the effect of electrosurgery on tissue discrimination using ex vivo animal tissue models," *Biomedical optics express*, vol. 11, no. 5, pp. 2402-2415, 2020.
- [35] A. E. Cerussi *et al.*, "Tissue phantoms in multicenter clinical trials for diffuse optical technologies," *Biomedical Optics Express*, vol. 3, no. 5, pp. 966-971, 2012.
- [36] B. W. Pogue, and M. S. Patterson, "Review of tissue simulating phantoms for optical spectroscopy, imaging and dosimetry," *Journal of biomedical optics*, vol. 11, no. 4, pp. 041102, 2006.
- [37] E. Ohmae *et al.*, "Stable tissue-simulating phantoms with various water and lipid contents for diffuse optical spectroscopy," *Biomedical Optics Express*, vol. 9, no. 11, pp. 5792-5808, 2018.
- [38] R. Pleijhuis *et al.*, "Near-infrared fluorescence (NIRF) imaging in breast-conserving surgery: assessing intraoperative techniques in tissue-simulating breast phantoms," *European Journal of Surgical Oncology*, vol. 37, no. 1, pp. 32-39, 2011.
- [39] M. Anastasopoulou *et al.*, "Comprehensive phantom for interventional fluorescence molecular imaging," *Journal of biomedical optics*, vol. 21, no. 9, pp. 091309, 2016.
- [40] G. Lamouche *et al.*, "Review of tissue simulating phantoms with controllable optical, mechanical and structural properties for use in optical coherence tomography," *Biomedical Optics Express*, vol. 3, no. 6, pp. 1381-1398, 2012.
- [41] K. E. Michaelsen *et al.*, "Anthropomorphic breast phantoms with physiological water, lipid, and hemoglobin content for near-infrared spectral tomography," *Journal of biomedical optics*, vol. 19, no. 2, pp. 026012, 2014.
- [42] N. Ukhrowiyah *et al.*, "Fabrication and characterization of breast phantom based on gelatin-glycerin-tio2 for a continuous-wave diffuse optical tomography," *Malaysian Journal of Science*, vol. 38, no. Sp3, pp. 53-65, 2019.
- [43] W. C. Vogt *et al.*, "Biologically relevant photoacoustic imaging phantoms with tunable optical and acoustic properties," *Journal of biomedical optics*, vol. 21, no. 10, pp. 101405, 2016.
- [44] M. Dantuma *et al.*, "Semi-anthropomorphic photoacoustic breast phantom," *Biomedical Optics Express*, vol. 10, no. 11, pp. 5921-5939, 2019.
- [45] S. Merritt *et al.*, "Comparison of water and lipid content measurements using diffuse optical spectroscopy and MRI in emulsion phantoms," *Technology in cancer research*, vol. 2, no. 6, pp. 563-569, 2003.
- [46] L. C. Cabrelli *et al.*, "Stable phantom materials for ultrasound and optical imaging," *Physics in Medicine Biology*, vol. 62, no. 2, pp. 432-447, 2016.
- [47] A. Taheri *et al.*, "Electrosurgery: part I. Basics and principles," vol. 70, no. 4, pp. 591. e1-e14, 2014.
- [48] M. G. Munro, "Fundamentals of electrosurgery part I: principles of radiofrequency energy for surgery," *The SAGES manual on the fundamental use of surgical energy (FUSE)*, pp. 15-59: Springer, 2012.
- [49] I. Alkatout *et al.*, "Principles and safety measures of electrosurgery in laparoscopy," *Journal of the Society of Laparoscopic & Robotic Surgeons*, vol. 16, no. 1, pp. 130-139, 2012.

- [50] J. C. Hebden *et al.*, "A soft deformable tissue-equivalent phantom for diffuse optical tomography," *Physics in Medicine Biology*, vol. 51, no. 21, pp. 5581-5590, 2006.
- [51] P. Li *et al.*, "Tissue mimicking materials in image-guided needle-based interventions: A review," *Materials Science Engineering: C*, vol. 93, pp. 1116-1131, 2018.
- [52] F. Ayers *et al.*, "Fabrication and characterization of silicone-based tissue phantoms with tunable optical properties in the visible and near infrared domain," in *Design and Performance Validation of Phantoms Used in Conjunction with Optical Measurements of Tissue*, Year, pp. 687007.
- [53] G. T. Kennedy *et al.*, "Solid tissue simulating phantoms having absorption at 970 nm for diffuse optics," *Journal of biomedical optics*, vol. 22, no. 7, pp. 076013, 2017.
- [54] J. Garrett, and E. Fear, "A new breast phantom with a durable skin layer for microwave breast imaging," *IEEE Transactions on Antennas Propagation*, vol. 63, no. 4, pp. 1693-1700, 2015.
- [55] A. I. Chen *et al.*, "Multilayered tissue mimicking skin and vessel phantoms with tunable mechanical, optical, and acoustic properties," *Medical physics*, vol. 43, no. 6Part1, pp. 3117-3131, 2016.
- [56] S. Srinivasan *et al.*, "Image guided near-infrared spectroscopy of breast tissue in vivo using boundary element method," *Journal of biomedical optics*, vol. 15, no. 6, pp. 061703, 2010.
- [57] G. Menikou, and C. Damianou, "Acoustic and thermal characterization of agar based phantoms used for evaluating focused ultrasound exposures," *Journal of therapeutic ultrasound*, vol. 5, no. 1, pp. 1-14, 2017.
- [58] M. A. Kandadai *et al.*, "Comparison of electrical conductivities of various brain phantom gels: Developing a 'brain gel model,'" *Materials Science Engineering: C*, vol. 32, no. 8, pp. 2664-2667, 2012.
- [59] G. Quarto *et al.*, "Comparison of organic phantom recipes and characterization by time-resolved diffuse optical spectroscopy," in *European Conference on Biomedical Optics*, Year, pp. 879905.
- [60] E. C. Bush *et al.*, "Fat-water phantoms for magnetic resonance imaging validation: a flexible and scalable protocol," *JoVE*, no. 139, pp. e57704, 2018.
- [61] M. O'Halloran *et al.*, "Development of anatomically and dielectrically accurate breast phantoms for microwave imaging applications," in *Radar Sensor Technology XVIII*, Year, pp. 90770Y.
- [62] N. Joachimowicz *et al.*, "Breast phantoms for microwave imaging," *IEEE Antennas Wireless Propagation Letters*, vol. 13, pp. 1333-1336, 2014.
- [63] M. Ostadrabimi *et al.*, "A heterogeneous breast phantom for microwave breast imaging," in *2009 Annual International Conference of the IEEE Engineering in Medicine and Biology Society*, Year, pp. 2727-2730.
- [64] M. Miyakawa *et al.*, "Development of non-uniform breast phantom and its microwave imaging for tumor detection by CP-MCT," in *2009 Annual International Conference of the IEEE Engineering in Medicine and Biology Society*, Year, pp. 2723-2726.
- [65] C. Hahn, and S. Noghanian, "Heterogeneous breast phantom development for microwave imaging using regression models," *International journal of biomedical imaging*, vol. 2012, pp. 803607, 2012.

[66] J. C. Y. Lai *et al.*, "Homogeneous and heterogeneous breast phantoms for ultra-wideband microwave imaging applications," *Progress In Electromagnetics Research*, vol. 100, pp. 397-415, 2010.

[67] E. Porter *et al.*, "Improved tissue phantoms for experimental validation of microwave breast cancer detection," in Proceedings of the fourth European conference on antennas and propagation, Year, pp. 1-5.

[68] B. Henin *et al.*, "Electro-biomechanical breast phantom for hybrid breast imaging," in 2015 International Symposium on Antennas and Propagation (ISAP), Year, pp. 1-3.

[69] I. E. Khuda, "A comprehensive review on design and development of human breast phantoms for ultra-wide band breast cancer imaging systems," *Engineering Journal*, vol. 21, no. 3, pp. 183-206, 2017.

[70] M. Freed *et al.*, "An anthropomorphic phantom for quantitative evaluation of breast MRI," *Medical physics*, vol. 38, no. 2, pp. 743-753, 2011.

[71] J. Meshram *et al.*, "Anti-microbial surfaces: An approach for deposition of ZnO nanoparticles on PVA-Gelatin composite film by screen printing technique," *Materials Science Engineering: C*, vol. 73, pp. 257-266, 2017.

[72] P. N. Charron *et al.*, "PVA-gelatin hydrogels formed using combined theta-gel and cryo-gel fabrication techniques," *Journal of the mechanical behavior of biomedical materials*, vol. 92, pp. 90-96, 2019.

[73] Y. Liu *et al.*, "Thermal behavior and mechanical properties of physically crosslinked PVA/Gelatin hydrogels," *Journal of the mechanical behavior of biomedical materials*, vol. 3, no. 2, pp. 203-209, 2010.

[74] M. A. Anugrah *et al.*, "Gelatin/Poly (vinyl alcohol)/Inorganic filler composites for phantom breasts," *Materials Chemistry Physics*, vol. 262, pp. 124333, 2021.

[75] A. Thangprasert *et al.*, "Mimicked hybrid hydrogel based on gelatin/PVA for tissue engineering in subchondral bone interface for osteoarthritis surgery," *Materials Design*, vol. 183, pp. 108113, 2019.

[76] A. Ito *et al.*, "Transglutaminase-mediated gelatin matrices incorporating cell adhesion factors as a biomaterial for tissue engineering," *Journal of bioscience bioengineering*, vol. 95, no. 2, pp. 196-199, 2003.

[77] M. K. McDermott *et al.*, "Mechanical properties of biomimetic tissue adhesive based on the microbial transglutaminase-catalyzed crosslinking of gelatin," *Biomacromolecules*, vol. 5, no. 4, pp. 1270-1279, 2004.

[78] L. T. Lim *et al.*, "Barrier and tensile properties of transglutaminase cross-linked gelatin films as affected by relative humidity, temperature, and glycerol content," *Journal of food science*, vol. 64, no. 4, pp. 616-622, 1999.

[79] S. A. Irvine *et al.*, "Printing cell-laden gelatin constructs by free-form fabrication and enzymatic protein crosslinking," *Biomedical microdevices*, vol. 17, no. 1, pp. 1-8, 2015.

[80] L. M. Bellan *et al.*, "A 3D interconnected microchannel network formed in gelatin by sacrificial shellac microfibers," *Advanced Materials*, vol. 24, no. 38, pp. 5187-5191, 2012.

[81] M. K. George *et al.*, "Perfusion flow phantoms with randomly oriented microchannels," in Medical Imaging 2018: Ultrasonic Imaging and Tomography, Year, pp. 1058006.

[82] R. Nachabe *et al.*, "Determination of water and lipid concentrations by diffuse optical spectroscopy in lipid emulsions in the wavelength range of 1000 to 1500 nm," in *Biomedical Optics*, Year, pp. BTuD88.

[83] R. K. Chen, and A. Shih, "Multi-modality gellan gum-based tissue-mimicking phantom with targeted mechanical, electrical, and thermal properties," *Physics in Medicine Biology*, vol. 58, no. 16, pp. 5511-5525, 2013.

[84] S. A. Solazzo *et al.*, "Radiofrequency ablation: importance of background tissue electrical conductivity—an agar phantom and computer modeling study," *Radiology*, vol. 236, no. 2, pp. 495-502, 2005.

[85] C. Ianniello *et al.*, "Synthesized tissue-equivalent dielectric phantoms using salt and polyvinylpyrrolidone solutions," *Magnetic resonance in medicine*, vol. 80, no. 1, pp. 413-419, 2018.

[86] V. G. Sirtoli *et al.*, "Electrical properties of phantoms for mimicking breast tissue," in 2017 39th Annual International Conference of the IEEE Engineering in Medicine and Biology Society (EMBC), Year, pp. 157-160.

[87] C. K. Chou *et al.*, "Formulas for preparing phantom muscle tissue at various radiofrequencies," *Bioelectromagnetics: Journal of the Bioelectromagnetics Society, The Society for Physical Regulation in Biology Medicine, The European Bioelectromagnetics Association*, vol. 5, no. 4, pp. 435-441, 1984.

[88] G. Fiaschetti *et al.*, "Tissue mimicking materials for multi-modality breast phantoms," in 2018 2nd URSI Atlantic Radio Science Meeting (AT-RASC), Year, pp. 1-6.

[89] T. J. Farrell *et al.*, "A diffusion theory model of spatially resolved, steady-state diffuse reflectance for the noninvasive determination of tissue optical properties in vivo," *Medical physics*, vol. 19, no. 4, pp. 879-888, 1992.

[90] R. Nachabé *et al.*, "Effect of bile absorption coefficients on the estimation of liver tissue optical properties and related implications in discriminating healthy and tumorous samples," *Biomedical optics express*, vol. 2, no. 3, pp. 600-614, 2011.

[91] R. Nachabé, *Diagnosis with near infrared spectroscopy during minimally invasive procedures*, 2012.

[92] D. J. Evers *et al.*, "Diffuse reflectance spectroscopy: towards clinical application in breast cancer," *Breast cancer research treatment*, vol. 137, no. 1, pp. 155-165, 2013.

[93] M. Dantuma, "Dataset 1.STL," T. O. S. Dataset., ed., 2019.

[94] M. Dantuma, "Dataset 2.STL," T. O. S. Dataset, ed., 2019.

[95] P. Taroni *et al.*, "Breast tissue composition and its dependence on demographic risk factors for breast cancer: non-invasive assessment by time domain diffuse optical spectroscopy," *PLoS one*, vol. 10, no. 6, pp. e0128941, 2015.

[96] N. Yoshizawa *et al.*, "Factors affecting measurement of optic parameters by time-resolved near-infrared spectroscopy in breast cancer," *Journal of biomedical optics*, vol. 23, no. 2, pp. 026010, 2018.

[97] A. H. Poh *et al.*, "Diffuse reflectance spectroscopic analysis of barium sulfate as a reflection standard within 173–2500 nm: From pure to sintered form," vol. 27, no. 6, pp. 393-401, 2019.

[98] M. Islam *et al.*, "A low cost and portable microwave imaging system for breast tumor detection using UWB directional antenna array," *Scientific reports*, vol. 9, no. 1, pp. 1-13, 2019.

---

- [99] G. Anand *et al.*, “Tissue phantoms to mimic the dielectric properties of human forearm section for multi-frequency bioimpedance analysis at low frequencies,” *Materials Science Engineering: C*, vol. 96, pp. 496-508, 2019.
- [100] Y. Liu *et al.*, “Tunable physical and mechanical properties of gelatin hydrogel after transglutaminase crosslinking on two gelatin types,” *International journal of biological macromolecules*, vol. 162, pp. 405-413, 2020.
- [101] Y. Wang *et al.*, “Transglutaminase-induced crosslinking of gelatin–calcium carbonate composite films,” *Food chemistry*, vol. 166, pp. 414-422, 2015.
- [102] L. Atarés *et al.*, “The role of some antioxidants in the HPMC film properties and lipid protection in coated toasted almonds,” vol. 104, no. 4, pp. 649-656, 2011.
- [103] C.-L. Tsai *et al.*, “Near-infrared absorption property of biological soft tissue constituents,” vol. 21, no. 1, pp. 7-14, 2001.
- [104] J. Byng *et al.*, “X-ray characterization of breast phantom materials,” *Physics in Medicine Biology*, vol. 43, no. 5, pp. 1367-1377, 1998.
- [105] G. J. Wengert *et al.*, “Accuracy of fully automated, quantitative, volumetric measurement of the amount of fibroglandular breast tissue using MRI: correlation with anthropomorphic breast phantoms,” *NMR in Biomedicine*, vol. 30, no. 6, pp. e3705, 2017.
- [106] M. Freed *et al.*, “X-ray properties of an anthropomorphic breast phantom for MRI and x-ray imaging,” *Physics in Medicine Biology*, vol. 56, no. 12, pp. 3513-3533, 2011.
- [107] S. Poompavai, and V. G. Sree, “Dielectric property measurement of breast—Tumor phantom model under pulsed electric field treatment,” *IEEE Transactions on Radiation Plasma Medical Sciences*, vol. 2, no. 6, pp. 608-617, 2018.



# 4

## Smart electrosurgical knife's functionality during electrosurgery

Detecting the cancerous growth margin and achieving a negative margin is one of the challenges that surgeons face during cancer procedures. A smart electrosurgical knife with integrated optical fibers has been designed previously to enable real-time use of diffuse reflectance spectroscopy for intraoperative margin assessment. In this chapter, the thermal effect of the electrosurgical knife on tissue sensing is investigated. Porcine tissues and phantoms were used to investigate the performance of the smart electrosurgical knife after electrosurgery. The fat-to-water content ratio (F/W-ratio) served as the discriminative parameter for distinguishing tissues and tissue mimicking phantoms with varying fat content. The F/W-ratio of tissues and phantoms was measured with the smart electrosurgical knife before and after 14 minutes of electrosurgery. Additionally, a layered porcine tissue and phantom were sliced and measured from top to bottom with the smart electrosurgical knife. Mapping the thermal activity of the electrosurgical knife's electrode during animal tissue electrosurgery revealed temperatures exceeding 400°C. Electrosurgery for 14 minutes had no impact on the device's accurate detection of the F/W-ratio. The smart electrosurgical knife enables real-time tissue detection and predicts the fat content of the next layer from 4 mm ahead. The design of the smart electrosurgical knife outlined in this chapter demonstrates its potential utility for tissue detection during electrosurgery. In the future, the smart electrosurgical knife could be a valuable intraoperative margin assessment tool, aiding surgeons in detecting tumor borders and achieving negative margins.

Published as:

Sara Azizian Amiri, Jenny Dankelman, Benno H. W. Hendriks, Enhancing Intraoperative Tissue Identification: Investigating a Smart Electrosurgical Knife's Functionality During Electrosurgery, *IEEE Transactions on Biomedical Engineering*, 2024.

## 4.1 Introduction

The increasing rate of patients undergoing cancer surgeries demands new technologies that can assist surgeons in pinpointing the border of the cancerous growth from the surrounding healthy or benign tissue to achieve complete tumor resection and negative margin [1].

Diffuse reflectance spectroscopy (DRS) has been studied vastly for its application in detecting the tissue type and discriminating healthy tissue from malignant tissue [2-12]. In DRS the amount of light that travels inside the tissue between the emitting and collecting fiber after multiple scattering and absorption events is measured [13].

From the diffused reflectance response of the tissue, optical characteristics of the tissue such as absorption and scattering profile or the concentration of the known chromophores of the tissue can be determined [14]. This potential has prompted scientists to further explore the application of the DRS in detecting abnormal tissue and discriminating it from the surrounding benign tissue [2-12]. For instance, de Boer *et al.* demonstrated that breast malignant tissue can be distinguished from benign tissue either by comparing the parameters related to the concentration of chromophores such as fat content or fat-water ratio (F/W-ratio) of the tissues or the different features on the specific wavelength ranges (400 nm-1600 nm) of the DRS spectrum of the tissues [5, 15, 16].

Being non-destructive, providing real-time results without requiring any extra contrast agent/dye or prior tissue/patient preparation [5] would be the advantage of the DRS over other existing margin assessment techniques. Although the effectiveness of the DRS in the detection of malignant tissue has been studied widely, the appropriate approach to incorporate DRS into the surgical workflow is still unclear.

Lately, efforts have been made to investigate the integration of the DRS into the electrosurgical knife as the main instrument that commonly being used by surgeons during tumor excision [17].

While an electrosurgical knife with intraoperative real-time tissue recognition power can become a “Holy Grail” for every surgeon performing cancer surgery, embedding DRS in the electrosurgical knife raises many challenges.

Adank *et al.* showed that tissue carbonization upon electrosurgery can change its optical properties and DRS response [18]. However, they also indicated that as long as a larger fiber distance is being used, the depth that light can travel inside the tissue becomes

---

larger than the depth of the affected tissue (cut or coagulated tissue) by the electrosurgical knife. Hence by using a larger fiber distance the effect of the electrosurgery on the accurate DRS read-out and tissue recognition can be minimized [18].

Tissue debris as a byproduct of electrosurgery could also have a huge impact on the optical tissue read-out. In a prior study, we, the authors of the present research, investigated the effect of the tissue debris attachment on the tip of the optical fibers which were mounted on the tip of a blade shape electrode of the electrosurgical knife [17]. After 30 seconds of electrosurgery with this DRS-integrated electrosurgical knife, a layer of contamination was formed on the tip of the optical fibers which mostly consisted of carbonized tissue. Moreover, it has been indicated that, to the extent that this contamination was a thin layer of debris, it would not adversely affect DRS measurement and tissue detection [17].

However, during the actual surgery, the electrosurgical knife would be used for several minutes which can cause a large amount of debris attachment and further disrupt the DRS measurements [18]. Furthermore, the effect of the heat produced during the electrosurgery on the optical fibers and DRS read-out, which can gravely disturb the application of the DRS-integrated electrosurgical knife, has not still researched.

While the Smart Electrosurgical Knife has been initially designed and developed previously [17-19], design modifications are imperative to enhance its robustness during electrosurgery. The goal is to minimize debris attachment and prevent optical fiber deterioration, issues stemming from the excessive heat generated during the procedure. To this end, this chapter addresses the following aspects: first, an exploration of the maximum temperature attainable during electrosurgery; next, an investigation into various electrode designs for the Smart Electrosurgical Knife to identify a design that effectively reduces the impact of heat and debris attachment, byproducts of the electrosurgery, on tissue optical readout. Finally, the functionality of the ultimate design in tissue detection during electrosurgery is examined using ex vivo animal tissue, along with a study involving phantoms.

Research findings have demonstrated significant variations in fat content (Fat%) and the ratio between fat and water content between healthy and malignant human breast tissue, highlighting their potential as distinguishing factors between the two tissue types [15, 16]. Consequently, in this chapter, these parameters are employed to evaluate the performance of the smart electrosurgical knife in detecting tissues with varying fat

content and its potential to identify positive resection margins. Here, the main application we foresee in the future for the smart electrosurgical knife is for breast conserving surgery (lumpectomy) since the main discriminative parameter between the healthy tissue and tumor tissue in this cancer was vastly researched by the researchers. However, the application of the device can further be prospected in other types of surgery in which the discrimination of the tissues is possible with the DRS.

## 4.2 Materials and Methods

The primary objective of this chapter is to identify and evaluate the optimal design for the smart electrosurgical knife, ensuring its durability against the elevated heat and debris generated during electrosurgery. To achieve this goal, a comprehensive series of experiments was conducted, following the outlined timeline: Initially, the temperature reached by the blade during electrosurgery was examined to ascertain the extent of temperature involved in the process (section II-A). Subsequently, diverse design iterations were developed with the intention of meeting the specified requirements (section II-B). Experiment setups, as detailed in section II-C, encompassing the DRS measurement console, ex vivo animal tissue, and tissue-mimicking phantoms were established and used to assess the functionality of the designs. Subsequently, investigations were conducted to assess the performance of the designs, pre-select the promising design, and further explore its potential (section II-D). These various designs were subjected to testing on animal tissue (section II-D1). Building upon the insights gained from these initial experiments, the most effective design was selected for further investigation. This subsequent phase involved testing the chosen design in electrosurgery settings similar to those employed by surgeons during breast cancer procedures, first on animal tissue (sections II-D2 and 3) and subsequently on a phantom model (section II-D4). Lastly, the smart electrosurgical knife, equipped with the optimized design, was utilized to take measurements while applying electrosurgery to layered animal and phantom tissues (section II-D5). The investigation aimed to determine the device's ability to distinguish distinct tissue layers prior to reaching the tissue borders.

### 4.2.1 Characterization of heat development during electrosurgery

To determine the range of the temperature of the heat that the optical fibers can be exposed to during the electrosurgery, a thermal imaging infrared camera (FLIR E54 24°,

Teledyne FLIR LLC, United States) was used to measure the thermal signature of the blade of the electrosurgical knife during electrosurgery on porcine belly tissue. The electrosurgical knife with a blade-shaped electrode (WEIDE, Hangzhou Valued Medtech Co.,Ltd, China) was used to cut the tissue in different modes and settings. Porcine belly was purchased from the local butcher. The effect of the electrosurgery settings on the temperature of the blade was investigated using an electrosurgery unit (Force FX, Valleylab, Medtronic plc, USA) which allowed the electrosurgery in different modes of Cut-Pure, Cut-Blend, Coagulation-Spray, Coagulation-Fulguration. In each mode, the cutting was performed with different cutting powers of 40 W, 50 W, and 60 W.

The electrosurgical knife was used to cut the tissue in each mode/each setting in a continuous mode for 1 minute (1 minute of tissue electrosurgery without stops). The thermal imaging camera, which was fixed using the holders close to the electrosurgery setup, captured movies over the tissue while being cut/coagulated using the electrosurgical knife. Subsequently, the whole experiment was repeated, this time in an interrupted mode in which the knife was active (on) for 2 seconds and then inactive (off) for 2 seconds and this pattern was repeated till the whole electrosurgery time reached 2 minutes (in total 1 min active and 1 min inactive). The selection of these options was based on the results of research that investigated the most common electrosurgery settings and the time that surgeons spend in various surgeries [20]. The interrupted mode is more close to what happens in reality during surgery [20]. Then using the thermal imaging infrared camera and then software (FLIR ResearchIR MAX, Teledyne FLIR LLC, United States), the temperature of the tip of the blade (region of interest) in each pixel was recorded and the maximum temperature of it for each experiment was determined.

#### 4.2.2 Heat and debris resistant design of the smart electrosurgical knife

Previously, the smart electrosurgical knife was developed by integrating DRS optical fibers into its structure. To date, two distinct designs have been documented. In the initial design (a prototype previously developed in [17, 18]), optical fibers were positioned within metallic tubes, which were affixed to the sides of a blade-shaped electrode using laser welding (Design 0). In the subsequent design iteration (Design 1), quartz tubes were added to the previous design to encapsulate the optical fibers on the blade-shaped electrode [19].

Given the adverse conditions of high temperature and debris exposure that the DRS optical fibers face during electrosurgery, this study introduces two additional distinct designs, referred to as Design 2 and Design 3, aimed at mitigating the adverse impact of heat on the optical fibers and DRS outputs. Depicted in Figure 4.1 are these designs. Subsequently, the designs underwent testing to evaluate their efficacy and performance.

#### *4.2.2.1 Description of Design 1*

In Design 1 the optical fibers were first put inside quartz tubes (Hengshui Yuanbo Import And Export Co, China) with an inner diameter (ID) of 300  $\mu\text{m}$  and an outer diameter (OD) of 1 mm.

#### *4.2.2.2 Description of Design 2*

In Design 2 heat shrinking Polytetrafluoroethylene (PTFE) tubes (Zeus Industrial Products, Inc., United States) were first heated up while the quartz tubes (Hengshui Yuanbo Import And Export Co, China) with ID of 300  $\mu\text{m}$  and OD of 500  $\mu\text{m}$  was inside those to reach the right size then the optical fiber was placed inside the quartz tubes and the whole part were placed inside the metallic tubes.

#### *4.2.2.3 Description of Design 3*

In Design 3, first, the optical fibers were put inside the PTFE tubes (Zeus Industrial Products, Inc., United States) and then quartz tubes (Hengshui Yuanbo Import And Export Co, China) with ID 600  $\mu\text{m}$  and OD 1 mm were used to surround the PTFE and optical fiber inside the metallic tubes.

### *4.2.3 Experimental setup*

To assess the smart electrosurgical designs and performance, the following experiment setups were used for further experimentation:

#### *4.2.3.1 DRS setup*

The DRS setup comprises a measurement console, software for processing the measurements, and a custom-designed DRS needle probe.

**Measurement console:** For DRS measurements, a Philips custom-designed DRS console (Philips Research, Eindhoven) was used. The console includes a halogen broadband light source (Avantes, The Netherlands) and two spectrometers, one designated to collect the light in the 900–1700nm spectral range (NIRQuest 512, Ocean

Optics, United States) and the other one in the 400-1000 nm spectral range (Maya2000 Pro, Ocean Optics, United States). One of the optical fibers was connected to the light source, the other one to the spectrometers, and the other end of the optical fibers was placed into the prototypes through different configurations. Before using each prototype, the optical console was calibrated thoroughly following the calibration process as mentioned in previous papers [3, 14, 21, 22]. Briefly, to calibrate the DRS console, the smart electrosurgical knife or the needle probe was placed at a fixed distance above a white reference standard (Spectralon with reflectivity of 99% for 400–1500 nm and >96% for 250–2000 nm, model: WS-1-SL, Labsphere Inc., United States) so that the distal end of the optical fibers become parallel to the surface of the standard. Subsequently, the spectral response of the white reference and a background measurement were recorded to minimize the influence of the ambient light [3, 14, 21, 22]. The calibration was performed once at the beginning of using each knife/probe.

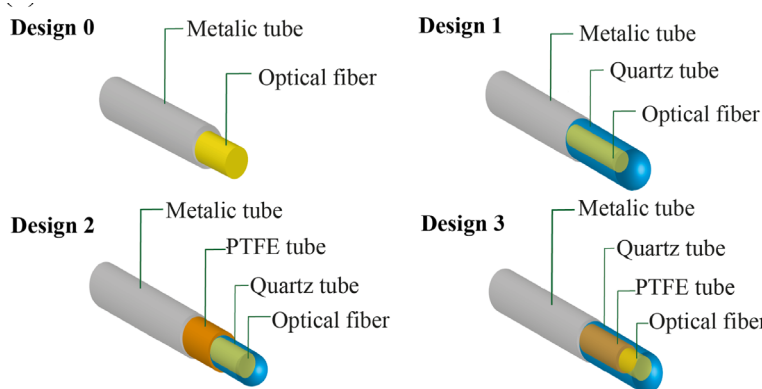


**Figure 4.1.** Different mounting approaches for integrating optical fiber to the electrosurgical knife

**Software:** The DRS system outputs were processed using a Philips custom-developed software (Philips Research, Eindhoven). In this MatLab-based software a nonlinear Levenberg–Marquardt inversion algorithm based on an analytical model, first described by Farrell *et al.* [23], was used to fit a curve on the input spectrum which can be used further to calculate the concentration of the chromophore from the fitted data. More information about the method and model can be found in [3, 14]. Using the software each spectrum was analyzed and the fat fraction (Fat/Fat+water) and the total amount of fat

and water content (Fat+Water) were extracted. More information regarding the DRS and its application in healthcare can be found in [4, 14, 22, 24].

**Custom-designed DRS needle probe:** Furthermore, in experiments described in sections II-D2, D3, and D4, a custom-designed DRS needle probe was also utilized, as employed in the author's previous research [17, 19, 21]. This probe featured a configuration that incorporated two optical fibers aligned in parallel with the probe's vertical axis, ensuring precise alignment of the fiber tips with the probe tip. With a functional fiber distance (FD) of 3.8 mm, this probe closely matched the FD of the smart electrosurgical knives.

Importantly, the design of the probe excluded the supplementary components found in the smart electrosurgical knife—components primarily designed to safeguard the optical fibers during electrosurgical procedures. Consequently, the outcomes obtained from these measurements serve as a control group, aimed at thoroughly investigating the impacts of integrating these supplementary components and the design of the smart electrosurgical knife on the measurement accuracy achieved by the prototypes.

#### 4.2.3.2 Ex vivo animal tissue model

Fresh ex vivo porcine belly tissue (purchased from the local butcher), adipose and muscle tissue, were utilized consistently in the experiments, serving both as a substrate for electrosurgery and as a sample for diffuse reflectance spectroscopy (DRS) measurements. Furthermore, in specific experiments, chicken liver tissue was employed as an additional sample for electrosurgery to deliberately contaminate the electrosurgical knife. The liver tissue, abundant in blood content, was chosen to compensate for the absence of blood in the porcine tissue.

#### 4.2.3.3 Tissue-mimicking phantoms to assess fat/water content

Tissue-mimicking phantom materials with tunable optical characteristics were developed to investigate the smart electrosurgical knives in a more controlled setup. These phantoms were produced with different and specific fat and water content to mimic tissues with various fat-to-water ratios. In comparison to animal tissue, these tissue-mimicking phantom materials have a more homogeneous composition, ensuring a reliable comparison between measurement results. The production process of these phantoms was previously described in [21]. Additionally, the materials utilized for

producing the phantoms are detailed in Table 4.1. Briefly, lard - pure porcine fat (BEEF&STEAK (<https://beefensteak.nl/>), Netherlands), distilled water, gelatin (250 Bloom, ES1477, Natural Spices, Netherlands) as an emulsifier and gelling agent, Transglutaminase (TG) (unique products Schuurman, Netherlands) as cross-linker, and sodium benzoate (SB) (Natural Spices, Netherlands) as preservation agent were used to produce the phantom.

**Table 4.1.** The material and their concentration used in production of the phantoms with different amount of fat and water

Role	Amount for 100 ml Phantom X%
Lard (ml)	X (ml)
Water (distilled) (ml)	100-X (ml)
Gelatin (g)	15% of water volume emulsifier
Transglutaminase (g)	10% of Gelatin weight increase the thermal stability
Sodium Benzoate (g)	0.1% of water volume

First, depending on the required fat content of the phantom, the mixture of the water and SB was heated in a beaker on a heater stirrer till the temperature reached 50 °C. Then the gelatin powder was added slowly to the mixture and the whole liquid was then heated up. When the temperature of the mixture reached 90 °C, the lard was added to it and the beaker remained on a stirrer for a few more minutes and then the TG was added slowly to it. After 10 minutes the content of the beaker was poured on the molds and placed inside the freezer. After an hour the mold was removed from the freezer and the content of it was placed in the fridge overnight.

#### 4.2.4 Performance assessment

##### 4.2.4.1 DRS measurements to preselect the promising design

To identify the most efficient design that can effectively protect the performance of the DRS during electrosurgery, the developed prototypes were tested in different experiments involving DRS measurements before and after electrosurgery on ex vivo

animal tissue. To investigate the effect of electrosurgery on the DRS performance, one prototype from each design was produced and used to measure fixed locations on three pieces of fresh porcine adipose tissue and three pieces of fresh porcine muscle tissue (purchased from the local butcher), as depicted in Figure 4.2(a). Then each prototype was used for electrosurgery on a large piece of porcine belly tissue, as depicted in Figure 4.2(b) (mixes of fatty and muscle tissue) for 2 minutes in continuous mode (2 minutes active time) in the electrosurgery mode of Cut-Pure-60 W. Then the used prototype was used again to take DRS measurement from the same fixed location on adipose and muscle tissue. Then the process was repeated this time with cutting 1 minute (1 minute active time) and again the same fixed tissue locations were measured. The second step was repeated two more times to reach a total of 5 minutes of electrosurgery. With this process, it was possible to compare the DRS spectra of the same location measured with a prototype that was used for electrosurgery in different durations so that the effect of electrosurgery (heat and debris attachment) on tissue measurements could be studied.

By comparing the overall shape of the spectra and the calculated F/W-ratios between the fixed location measured with the unused prototype (before electrosurgery) and then the used prototype (after electrosurgery), it was possible to identify the most promising design. The results of these experiments unveiled the promising nature of the electrosurgical knife with Design 2. Subsequently, this design was selected for use in the subsequent experiments to further explore its application.

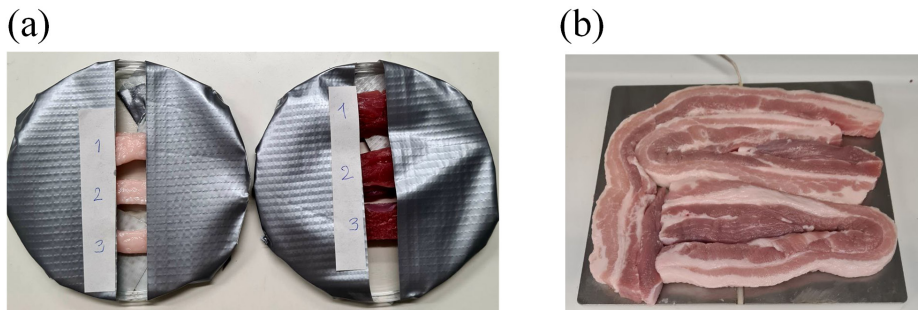


**Figure 4.2.** Ex vivo animal tissues used in the experiments, with specific details provided in section II.C. In the image (a), three sections of porcine adipose tissue (on the left) and muscle tissue (on the right) are presented. These tissue samples were employed for Diffuse Reflectance Spectroscopy (DRS) measurements and were secured onto the plate using gray tapes. In image (b), the representation features the porcine tissue that underwent electrosurgery.

#### *4.2.4.2 DRS measurements in an interrupted electrosurgery*

Design 2, which exhibited the most promising outcomes in the previous experiment was used for further investigations to determine its fullest potential. During a lumpectomy surgery, the electrosurgical knife usually is active on average for 2 seconds (0.6 s-3.8 s, measured for 23 lumpectomy surgery) [20] and in general, based on a surgical observation the whole activation time of the electrosurgical knife (sum of the time of each activation period) during the lumpectomy surgery is around 3.5 minutes to 7 minutes [25].

The smart electrosurgical knife with Design 2 (based on the outcomes of the previous experiment) was tested in a realistic setup similar to the lumpectomy surgery to indicate whether it can withstand the harsh environment during the lumpectomy electrosurgery and can accurately detect the tissue even after being used for several minutes. To resemble the previous experiment, pork muscle and fat tissue along with fresh chicken liver were used for the electrosurgery to contaminate the electrosurgical knife. The liver tissue with high blood content was used to compensate for the lack of blood in the porcine tissue.

Similar to the previous experiment, the chosen prototype was used for cutting the animal tissues for different durations in the interrupted (2 seconds on-2 seconds off) in Cut-Pure mode with the power of 60 W. Before using the prototype and then after every 2 minutes of cutting (in total 1 min activation time and 1 min inactivation time), DRS spectra were taken from specific locations on 3 pieces of porcine muscle tissue and 3 pieces of porcine adipose tissue, similar to the figure shown in Figure 4.2(a). This process was repeated seven times to reach the total cutting duration of 14 minutes (7 minutes on-7 minutes off). Furthermore, the custom-designed DRS needle probe was also utilized, as employed in the author's previous research [17, 19, 21]. The probe was employed to conduct DRS measurements at fixed locations on sections of porcine tissue. Then the outputs of the DRS console were explored through the same method mentioned in the previous sections using the Philips custom-designed software. The performance of Design 2 was evaluated by comparing variations in the shape of spectra and the calculated F/W-ratios of measurements obtained using the smart electrosurgical knife used for different durations of electrosurgery, as well as those taken with the optical needle probe.

#### *4.2.4.3 DRS measurements in an extended electrosurgery*

In previous experiments, the electrosurgical knife was deactivated for DRS measurements of porcine tissue after every 2 minutes of electrosurgery (1 minute active-1 minute inactive), whereas, during lumpectomy surgery, the electrosurgical knife can remain active for more extended periods [20, 25], subjecting the blade design to higher temperatures. To investigate the impact of prolonged electrosurgery on the smart electrosurgical knife's performance, this experiment involves using the smart electrosurgical knife with the promising design to perform electrosurgery (Cut-Pure-40W) on porcine tissue and chicken liver tissue for a continuous 14-minute duration (with no intervening measurement sessions) in an interrupted mode (2 seconds on-2 seconds off), subsequent to the initial DRS measurements from porcine adipose and muscle tissue (3 separate pieces of each, at specific locations, similar to the figure shown in Figure 4.2(a)). Afterward, DRS measurements from those specific porcine muscles and adipose pieces (same locations that were measured before electrosurgery) were carried out. This experiment was then performed again with a clean knife with Design 2 in the same condition only with a cutting power of 60W to compare the effect of the cutting power on the performance of the prototype and the final outcomes. The results of the DRS measurements then were interpreted using the same method mentioned in the last experiments. Furthermore, measurements taken by the needle probe from the specific location on the porcine muscle and adipose tissue were used as the control group, similar to the previous experiments. In a manner similar to the previous experiment, the spectral shape and calculated F/W-ratios were used to assess the performance of Design 2 in this experiment.

#### *4.2.4.4 Fat and water content estimation in phantoms*

One of the issues of using porcine tissue for comparing the DRS measurements (before and after surgery) is that whenever the tissue is pressed with the tip of the device, the tissue content moves slightly. Since the tissue composition is not homogeneous, with each small movement, the measured tissue can change a little, which could lead to small differences in the DRS response. Hence, the comparisons of the measurements taken with different probes from one specific location can be debatable. To address this issue, the homogeneous tissue-mimicking phantom with tunable fat and water content was produced (section II-C3) to investigate the performance of the prototype in a more controlled situation.

To determine if the smart electrosurgical knife with Design 2 can accurately estimate the fat content of the phantoms, tissue-mimicking phantom materials with Fat% of 0%, 5%, 15%, 20%, 40%, 50%, 60% were made following the process mentioned in section II-C3. Moreover, a piece of lard (pure porcine fat) was used as a phantom material with Fat% close to 100%. Then from each phantom with different Fat%, DRS measurements were obtained from 3 different locations, once using a normal DRS needle probe (used as reference measurements as mentioned in previous sections) and once using a new smart electrosurgical knife. Then the Fat% and F/W-ratio of each spectrum were calculated and employed to assess the performance of Design 2.

For the second phantom study, the potential of the smart electrosurgical knife in accurate detection of the Fat% of the phantom after the knife was used for electrosurgery (used and contaminated) was tested. Similar to the experiment mentioned in previous sections, first a smart electrosurgical knife (Design 2) and then a needle probe (as reference) were used for measuring phantoms with Fat% of 10%, 40%, and 60%. Then the smart electrosurgical knife was used to cut porcine tissue (muscle and adipose) and chicken liver tissue for 14 minutes in an interrupted mode (2 seconds on- 2 seconds off) with electrosurgery settings of Cut-Pure, once with the power of 40 W and once with the power of 60 W. Afterwards, measurements were acquired from the phantoms by the used/contaminated smart electrosurgical knife. Then the measured Fat% of each phantom taken by the needle probe, clean smart electrosurgical knife, and used smart electrosurgical knife were compared.

#### *4.2.4.5 Real-time measurement during cutting layered tissue and phantom*

A layered porcine tissue consisting of layers of adipose and muscle tissue, along with a layered phantom containing layers with different Fat% was prepared. The depth of the layers of the layered porcine tissue was not isometric or specified. However, each layer of the layered phantom had a 1 cm depth.

The smart electrosurgical knife was fixed on a vertical translation stage to set its height, while its horizontal movement was manually controlled. The tip of the knife was perpendicular to the top surface of the tissue/phantoms. The layered porcine tissue (placed on the back electrode of the electrosurgical unit) was cut (electrosurgery) from top to bottom with steps of 2 mm using the smart electrosurgical knife with the setting of Cut-Pure-60W (2 mm of cutting the tissue/phantom while the knife is active). After each

2 mm of cutting, the smart electrosurgical knife was stopped at the location, and DRS measurements were acquired. Then the process was repeated until the knife reached the bottom of the tissue/phantom. From the DRS spectra at each location, Fat% and F/W-ratio (as explained in the previous sections) were calculated and reported.

#### 4.2.5 Statistical analysis

On each measuring location on the porcine tissue or phantom material, three or four spectra were taken (different in each experiment). Moreover, the measurements were taken on three different locations (or pieces) which resulted in nine or twelve measurements in total for each tissue/phantom material in each experiment. The final spectrum of each measured location was averaged and shown in the graphs as the mean of these nine/twelve measurements  $\pm$  SD (standard deviation, highlighted area). The measured Fat% or F/W-ratio was also reported as the mean  $\pm$  SD of the calculated parameter from those nine/twelve measurements. Depending on the experiment the one-way or two-way ANOVA was used to statistically study the results and find evidence of any significant differences between the groups of the measurements. *p*-value less than 0.05 was considered significant (\*: *p*-value  $< 0.05$ , \*\*: *p*-value  $< 0.01$ , \*\*\*: *p*-value  $< 0.001$ ). For the statistical analysis of the data or producing the graphs, MatLab (The MathWorks, Inc., Natick, Massachusetts, United States) and GraphPad Prism version 8.1.2 (GraphPad Software, La Jolla, CA USA, [www.graphpad.com](http://www.graphpad.com)) were used.

### 4.3 Results

#### 4.3.1 Characterization of heat development during electrosurgery

Figure 4.3(a) shows the thermal image of the porcine tissue and the electrode during electrosurgery. The maximum temperate that the tip of the electrode reached in continuous (1 minute) or interrupted (2 minutes, 2 seconds on- 2 seconds off) electrosurgery in different settings and powers are shown in Figure 4.3(b and c). Electrosurgery in interrupted mode with cool-down periods corresponded with a lower temperature than electrosurgery in continuous mode. In both continuous and interrupted modes, in most cases, the maximum temperature of the blade increased by increasing the power from 40 W to 60 W. Electrosurgery in Cut-Pure produced the highest temperature in the blade (438.9°C in continuous mode and 351.7°C in interrupted mode) while the

electrosurgery in coagulation modes (Fulguration and Spray) resulted in a lower temperature in the blades ( $\approx 100$ - $200$ °C).

### 4.3.2 Performance assessment

#### 4.3.2.1 DRS measurements to preselect the promising design

Design 0 was excluded from the experiments since after 1 minute of cutting the optical fibers were damaged and DRS measurement was not possible anymore.

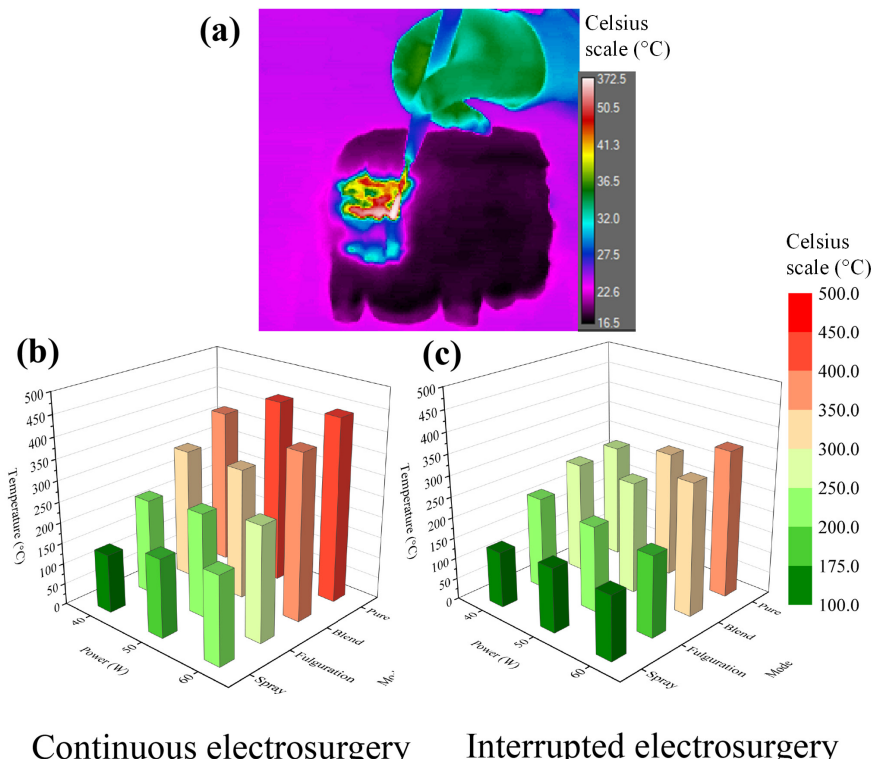


**Figure 4.3.** Heat measurements during electrosurgery. (a) A typical image captured by the FLIR camera on the porcine tissue. (b) and (c) are showing the maximum temperature (°C) that the tip of the electrode of the electrosurgical knife reached during electrosurgery in different settings and powers. (b) is showing the blade tip temperature in continuous electrosurgery and (c) is showing the blade tip temperature interrupted electrosurgery. The graphs were made with OriginPro 2015, OriginLab Corporation, Northampton, MA.

Figure 4.4 shows the results of DRS measurements, along with the calculated F/W-ratio, from fixed locations on three porcine muscle tissue samples and three porcine adipose tissue samples taken with the smart electrosurgical knives before electrosurgery

and then after electrosurgery with the settings of Cut-Pure-60 W, in continuous mode and different durations (maximum 5 minutes). Since the measured F/W-ratio fluctuates largely for each design, the scale of the F/W-ratio diagram is adjusted differently for each design. In Design 1 the morphology of the DRS spectrum was changed noticeably after 2 minutes of electrosurgery. The most affected part of the spectrum is the Near-Infrared part which is the area where fat and water have the main absorption peaks (close to 1000 nm and 1200 nm). This explains the alternation of the F/W-ratio of the tissue, measured after using Design 1, especially for muscle tissue. Due to the low fat content of the muscle tissue, the F/W-ratio of this tissue is usually less than 1. On the contrary, the F/W-ratio of the muscle measured by the knife with Design 1 exceeds one when the knife is used for 2 minutes. Although the morphology of the adipose spectrum changes by increasing the duration of electrosurgery, the most affected part of the spectrum is in the visible wavelength ranges, which mostly corresponds to the blood content of the tissue. Hence, it is expected to see less fluctuation in the F/W-ratio of the adipose tissue. In Design 3, not only does the shape of the spectra of both muscle and adipose tissue change after a few minutes of electrosurgery but also the F/W-ratio of both tissues changes significantly, making this design unreliable after electrosurgery. Contrastingly, when employing Design 2 for DRS measurement, the morphology of the spectrum for each tissue remains nearly unchanged even after 4 minutes of electrosurgery. However, the spectrum of the tissues changes significantly after 5 minutes of electrosurgery, especially in adipose tissue. The F/W-ratio of the tissues fluctuates less slightly in comparison to the other designs. Based on these outputs, this design (Design 2) was used for further investigations on settings more similar to realistic setups (Interrupted electrosurgery mode).

#### *4.3.2.2 DRS measurements in an interrupted electrosurgery using Design 2*

The results of the experiment in an interrupted electrosurgery mode are shown in Figure 4.5. For each tissue type (muscle and adipose tissue) four measurements were done, each on three different locations, which results in twelve measurements per tissue. The spectra are shown as the average of these twelve spectra with the SD.

In Figure 4.5(b) the results of DRS measurement in front of white reference (Spectralon<sup>®</sup>) taken by needle probe and by a smart electrosurgical knife before electrosurgery and then after each time of electrosurgery are shown.

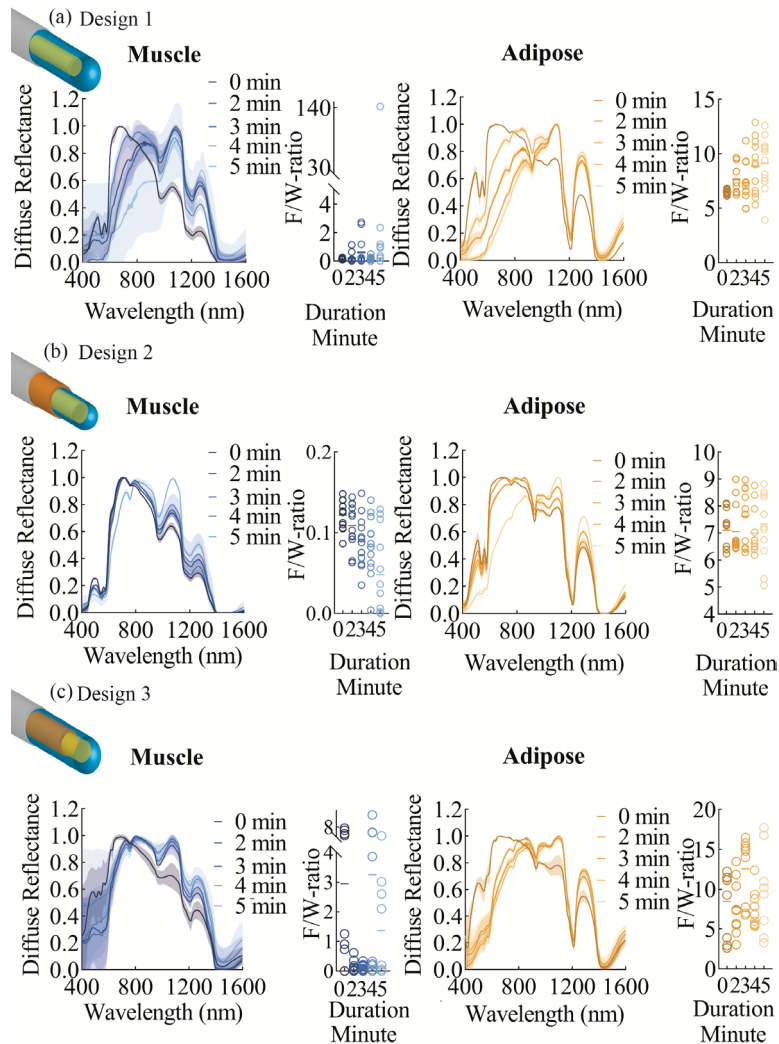


**Figure 4.4.** Tissue detection results following continuous electrosurgery using different smart electrosurgical knife designs. Each design was employed to measure the diffuse reflectance spectroscopy (DRS) response of three pre-fixed adipose tissue samples and three pre-fixed muscle tissue samples (as depicted in Figure 4.2(a)), both before (0 minutes) and after being subjected to electrosurgery at different durations. Electrosurgery was performed on separated pieces of the tissue shown in Figure 4.1(b). Each measurement on each of these three tissue pieces was replicated four times, resulting in twelve measurements for each tissue type (muscle and adipose) at each duration of electrosurgery, ranging from 0 minutes to 5 minutes. The figure presents the averaged spectra of these 12 measurements with highlighted areas around the spectra indicating the standard deviation (SD). The data on the F/W-ratio scatterplot represent the calculated F/W-ratio from all twelve measurements on the specific tissue (three tissue pieces, with four replicates for each tissue piece, resulting in 12 measurements per tissue) after electrosurgery at different durations.

The DRS spectrum for the needle probe and the unused and clean smart electrosurgical knife is the smooth line and similar to each other. Then after the electrosurgery the spectra change, mostly at visible light wavelengths (400-1000 nm). The dents on the spectra are at the wavelengths where absorption occurs in the blood (414 nm, 433 nm, 542 nm, 556 nm, 576 nm, 758 nm) and fat (760 nm, 930 nm, 1042 nm, 1211 nm, 1393 nm, and 1414 nm), showing that the source of these changes can be the tissue contamination (main contamination with blood and fat).

The overall shape of the spectra of the adipose and muscle tissue stayed almost the same when taken by the needle and the smart electrosurgical knife before and after electrosurgery (Figure 4.5(c and e)). Some deviations were seen on the spectrum of the tissues measured by the needle probe and then the unused smart electrosurgical knife, mostly in the visible part (400 nm-800 nm) of muscle tissue and in the NIR part (800 nm-1600 nm) of adipose tissue. Subsequent to electrosurgery and then measurement using the smart electrosurgical knife, the spectrum of the muscle tissue was altered slightly in the NIR part while the spectrum of the adipose tissue was mostly changed in the visible light wavelengths.

However, the calculated F/W-ratio for each tissue taken by the smart electrosurgical knives after electrosurgery for different durations is not significantly different from the F/W-ratio measured using the needle probe or the clean (unused) smart electrosurgical knife. The results of the one-way ANOVA test on the multiple comparisons of the calculated F/W-ratio showed in most cases no significant differences between F/W-ratio of tissues measured by the needle probe, clean smart electrosurgical knife and then the smart electrosurgical knife after being used for electrosurgery in different durations.

The only significant difference was detected between the F/W-ratio of the adipose tissue measured with a smart electrosurgical knife after 2 minutes (4 minutes interrupted) and 7 minutes (14 minutes interrupted) electrosurgery with  $p=0.035$ . Considering the non-significant deviation of the measured F/W-ratio by the smart electrosurgical knife after electrosurgery for extended durations, the muscle tissue (F/W-ratio  $< 0.3$ ) and adipose tissue (F/W-ratio  $> 5$ ) are easily detectable from each other.

#### *4.3.2.3 DRS measurements in an extended electrosurgery using Design 2*

The statistical analysis of the results (shown in Figure 4.6(a) and Figure 4.6(c)) showed no significant differences between the F/W-ratio measured before and after the

electrosurgery with the smart electrosurgical knife and the needle shape DRS probe in both experiments.

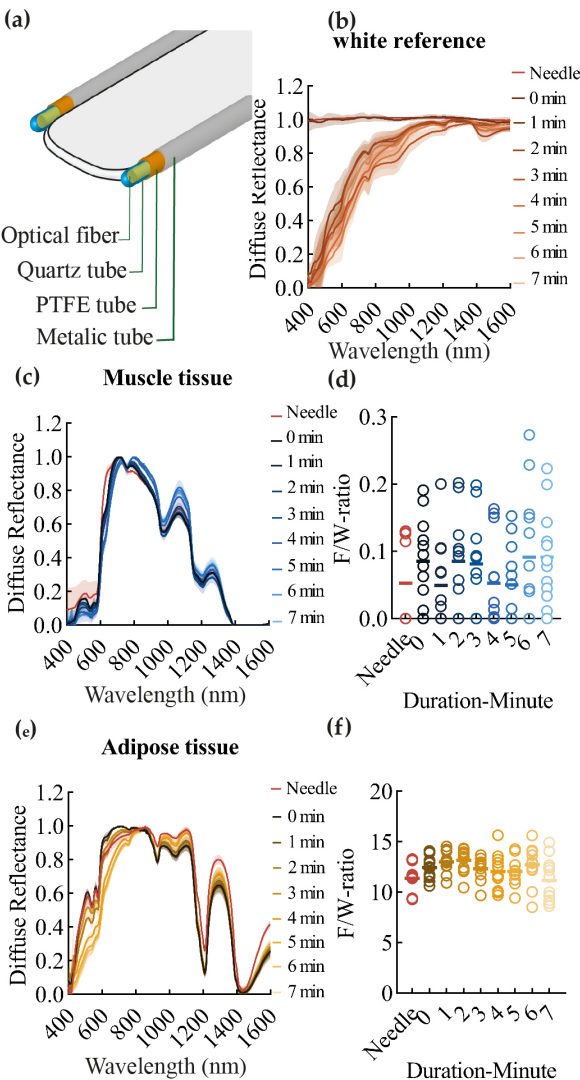


**Figure 4.5.** Tissue detection results after interrupted electrosurgery using Design 2. Durations of electrosurgery mentioned in minutes are the total activation time during 2 minutes of interrupted electrosurgery (2 seconds on-2 seconds off). Hence, 7 minutes duration means 14 minutes of interrupted electrosurgery. (a) Sketch of the Design 2. (b) Spectrum of the needle probe and then the smart electrosurgical knife in front of the white reference before and after each 2 minutes of interrupted electrosurgery. After each 2 minutes of electrosurgery, the smart electrosurgical knife was used to measure the DRS response of (c) the muscle and (e) adipose tissue, and to calculate the F/W-ratio for (d) muscle and (f) for adipose tissue.

In Figure 4.6(b) the average of the measured spectrum using a needle probe, and the smart electrosurgical knife before and after electrosurgery for each tissue were displayed. Although there are some deviations between the measured spectra, these alterations had no significant effect on the measured F/W-ratio of the tissues.

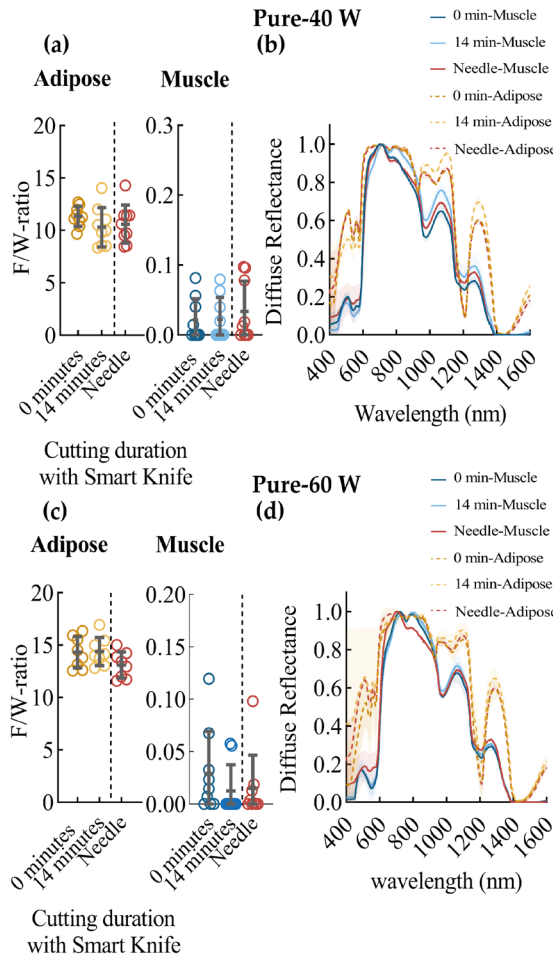


**Figure 4.6.** Results of the smart electrosurgical knife (Design 2) after 14 minutes of electrosurgery in interrupted mode (2 seconds on-2 seconds off). (a) and (c) the measured F/W-ratio after the electrosurgery with power of 40 W (a) and 60 W (c) are shown for each tissue. (b) and (d) the average of the measured spectra of each tissue using the DRS needle probe, and the smart electrosurgical knife before and after the electrosurgery with power of 40 W (b) and 60 W (d).

After the electrosurgery with 60 W the average spectra of the tissues (shown in Figure 4.6(d)), mainly the adipose tissue, showed more fluctuation, with larger SD, mostly

at the visible wavelengths. In summary, electrosurgery did not have a negative impact on the results, demonstrating that even after 14 minutes of interrupted electrosurgery, the smart electrosurgical knife can still correctly measure the spectral response and F/W-ratio of the tissue.

#### *4.3.2.4 Fat and water content estimation in phantoms using Design 2*

The results of DRS measurements on phantoms are shown in Figure 4.7(a). Two-Way ANOVA was used for static analysis of the data. The results of the tests showed only a significant difference between the F/F+W of the Phantom 60% measured with a needle probe and the knife with  $p < 0.0001$ .

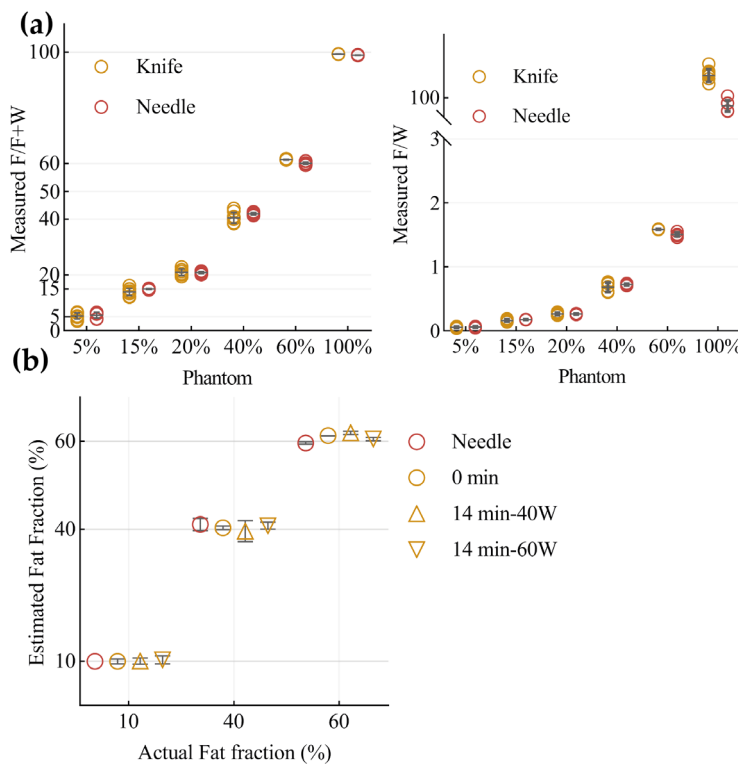
The mean F/F+W of the Phantom 60% measured with needle probe was 60.1% and with the knife was 61.38%. Moreover, significant differences between the F/W-ratio of the Phantom 60% measured using the probe (1.506) and the knife (1.587) were seen with a p-value of  $< 0.0001$ . Furthermore, the test results showed a significant difference between the measured F/F+W and F/W-ratio of Phantom 100% using the probe (mean F/F+W of 98.86%, mean F/W-ratio of 87.3) and the knife (mean F/F+W of 99.26%, mean F/W-ratio of 135.5). There were no other statistical differences between other measurements and the calculated parameters related to the fat content of the phantoms measured using a smart electrosurgical knife or needle probe.

Figure 4.7(b) shows the F/F+W of the phantoms measured using a needle probe, an unused smart electrosurgical knife, and then the smart electrosurgical knives used for electrosurgery with different powers. The results of statistical analysis on the F/F+W showed no significant differences between the fat content of the phantoms measured before and after the electrosurgery using the smart electrosurgical knife.

#### *4.3.2.5 Real-time measurement during cutting layered tissue and phantom*

Layered porcine tissue (Figure 4.8(a)) and phantom (Figure 4.8(c)) were cut and measured using a smart electrosurgical knife from top to bottom. The graph in Figure 4.8(b) presents the measured F/F+W and F/W-ratio of the locations with a 2 mm distance from each other on the layered tissue, which shows a clear transition between the layers. Since there was no control over the tissue in front of the knife, the experiment was also redone on a layered phantom in which each phantom had a specific depth and known concentration of fat and water.

The numbers on the layers in Figure 4.8(c) show the F/F+W of that layer. The measured F/F+W and F/W-ratio of the phantom at each point (steps of 2 mm) are shown in Figure 4.8(d). In this graph, the transition between layers is clearly visible. Interestingly, when transitioning from the top of one layer to the top of the next layer, both parameters, F/F+W and F/W-ratio, first reach the F/F+W and F/W-ratio of the layer that the blade is currently inside, and then, as the transition progresses, the parameter either decreases or increases based on the fat content of the next layer before reaching that layer. This shows that the smart electrosurgical knife can detect the layers of the phantom from a few millimeters before reaching the layer.



**Figure 4.7.** Phantom measurements with the DRS optical needle and the clean and unused smart electrosurgical knife used on the different Phantoms X% (Table 4.1). (a) Fat fraction, F/F+W, (b) F/W-ratio , and (c) F/F+W of the phantoms measured using needle probe, and the smart electrosurgical knife before and after using the knives for electrosurgery on animal tissue with different powers.

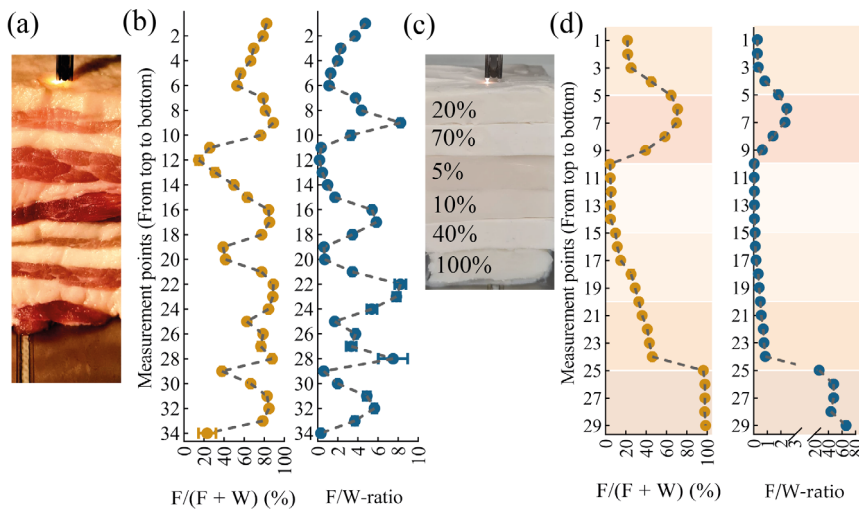


**Figure 4.8.** Tissue detection results of the smart electrosurgical knife while cutting a layered tissue or phantom. (a) The layered tissue with layers of the adipose and muscle tissue. (b) Measured  $F/(F+W)$  and  $F/W$ -ratio of the layered tissue from top to bottom after each 2 mm of electrosurgery in this direction. (c) Layered phantom consisting of layers with different amount of fat. The number on the layers indicates the  $F/(F+W)$  of each layer. (d) Measured  $F/(F+W)$  and  $F/W$ -ratio of the layered phantom from top to bottom after each 2 mm of electrosurgery in this direction.

#### 4.4 Discussion

The main In the pursuit of advancing the field, our study introduces substantial design modifications to elevate the capabilities of a smart electrosurgical knife. In this study, our primary goal was to address challenges related to heat-induced optical changes and debris attachment. Through the implementation of design enhancements, particularly the incorporation of quartz and PTFE tubes, we achieved promising results. This refined design was subsequently employed in a realistic setup, demonstrating its efficacy in providing reliable DRS measurements on porcine tissue and tissue-mimicking phantoms, even during prolonged electrosurgery sessions lasting up to fourteen minutes. Notably, the smart electrosurgical knife's improved design facilitated real-time measurements in the dynamic context of electrosurgery on layered porcine tissue and a layered phantom.

Difficulty in the detection of a safe tumor margin during cancer surgeries, such as breast lumpectomy, is an obstacle for surgeons which can result in a positive margin. In our previous research, we developed a smart electrosurgical knife with the goal of providing surgeons with real-time tissue feedback to guarantee a negative margin as a

result of cancer surgery [17, 18]. The initial iteration of the smart electrosurgical knife was made by integrating a normal electrosurgical knife with diffuse reflectance spectroscopy technology [17, 18]. In the current research, we aimed to further enhance the design of the smart electrosurgical knife and investigate its functionality during electrosurgery.

It has been shown that using DRS the composition of the tissue can be determined and therefore different tissues can be distinguished from each other. The application of the DRS in the detection of the tumor tissue from surrounding benign tissue for a variety of cancers has been studied in many research through the last decade, e.g. for breast cancer [3, 15], lung cancer [6], liver cancer [2, 10], skin cancer [11], cervical cancer [9], colorectal cancer [7] and oral cancer [8].

To measure the tissue using the DRS system, the optical fibers of the DRS setup (which are connected to a light source and the spectrometers) are required to be in close contact with the tissue. To do so, in the development of the smart electrosurgical knife, the optical fibers should be placed on the tip of the electrode of the knife such that they are positioned as much as possible close to the tissue during the electrosurgery. One of the main issues with this idea is the high temperature that the optical fibers can be exposed to during the electrosurgery which could destroy the fibers [17]. The other side effect of the heat is the tissue carbonization and debris attachment upon the electrosurgery which could affect the DRS measurements and tissue read-out [18].

Screening the thermal behavior of the electrode of the knife during the electrosurgery showed that the maximum temperature during electrosurgery in Pure-60W mode would be  $\approx 438^{\circ}\text{C}$ , while usually in a breast cancer surgery the temperature (in a normal setting, 40 W) the maximum temperature would be between 200-300 $^{\circ}\text{C}$ .

One of the limitations of the heat measurement experiment was the attachment of debris (burned or unburned tissue) to the electrode of the electrosurgical knife during the electrosurgery. This phenomenon, along with the subsequent alterations in thermal emissivity dynamics, presents a significant consideration in the context of temperature measurement during electrosurgical procedures. In the future, it's important to improve the methodology of measuring temperatures during electrosurgery. This will involve using more controlled methods to better account for debris attachment and emissivity changes. These improvements are essential to ensure accurate temperature measurements.

Besides the exposure to the high temperature, the debris attachment [17] and mechanical damages (while using the knife and also during cleaning cycles) could affect the optical fibers that were placed close to the tip of the electrode of the electrosurgical knife. Therefore, the encapsulation of the optical fiber inside quartz was used as an approach to protect those from destructive conditions. Among the different investigated designs in this research, Design 2, in which an extra PTFE tube was used around the quartz tubes, showed the most promising results. In Designs 1 and 3, considerable spectra and F/W-ratio alterations were seen after only one minute of electrosurgery, indicating that the optical fibers could be damaged and that the housings could not protect the fibers completely. Besides, in Design 3, the variation of the average spectrum in each electrosurgery duration was large which could be due to the PTFE tube around the optical fiber. It is noteworthy to emphasize that throughout all experiments, a clear distinction was maintained between the tissues utilized for the electrosurgery procedures and those designated for measurements. Measurements were consistently performed at predefined, fixed locations on separate tissue pieces, which remained intact throughout each experiment's duration. This approach established a constant reference point for measurements, ensuring that any observed variations primarily stemmed from differences in the electrosurgical knife design rather than potential changes in the tissue itself.

During the continuous electrosurgery in Pure-60W mode, the smart electrosurgical knife with Design 2 could still measure the tissue accurately. After 4 or 5 minutes of electrosurgery in this mode, some changes in the overall shape of the spectra of the tissue were noticeable, mostly in the visible wavelengths. However, continuous electrosurgery in 60 W and pure mode is an uncommon setting for cancer surgery. During a normal lumpectomy surgery, the common electrosurgery setting is 35-40 W in the blend or pure cutting mode [20] which can result in lower temperatures and a less distractive environment. Moreover, the measurement of the electrosurgical unit activation time during lumpectomy surgery showed that each time activation of the knife lasts on average for 2 seconds (0.6-3.8 s) [20]. Accordingly, in the next experiments, the smart electrosurgical knife with Design 2 was used in a more realistic setting and in interrupted electrosurgery mode with cycles of 2 seconds on - 2 seconds off. The spectrum taken by the smart electrosurgical knife in front of the white reference after the electrosurgery was not the same as the spectra of the knife before surgery and the needle probe. These

alterations in the spectra were due to the tissue contamination mostly with blood and fat. These results are in line with what is reported in [17], in which the same alternation on the spectrum was seen and chemical analysis of the contamination on the tip of the optical fibers showed that the contamination is mostly carbonized tissue along with traces of biological components such as Na and Mg [17].

Although the contamination was seen in front of the optical fiber (on the outer side quartz tube) which also altered slightly the spectra of the adipose and muscle tissue in some wavelengths, these contaminations could not affect the measured F/W-ratio of the tissue significantly in comparison to the F/W-ratio measured with the clean/unused smart electrosurgical knife before electrosurgery. The same results were also achieved when the smart electrosurgical knife was used for 14 minutes of electrosurgery in interrupted mode (2 seconds on - 2 seconds off) with different powers (40 W and 60 W). Despite some variations that occurred in the spectrum of each tissue measured after electrosurgery, the measured F/W-ratio did not fluctuate largely. Indicating that even after 14 minutes of electrosurgery with a power of 60 W in an interrupted setting, the type of the tissue is detectable, and tissues can be distinguished from each other. There were some statistically non-significant but noticeable deviations between the F/W-ratio of the tissues measured using the smart electrosurgical knife and needle probe. The source of these variations could be due to the different optical fibers that have been used to produce the probes or the small difference between the fiber distance of the needle probe (3.8 mm) and the smart electrosurgical knife (3.87 mm).

A tissue-mimicking phantom with known composition was used in this research to investigate the tissue detection power of the smart electrosurgical knife in a more controlled approach. The phantoms were created using the formulation originally introduced in our previous study [21]. In this chapter, we showed that a phantom with different fat content can be produced to closely represent the DRS profile of real human breast tissue as well as porcine tissue [21]. Similarly, in this research phantoms with a fat content from 5% to 100% were produced. The DRS measurement using the DRS needle probe and then the unused smart electrosurgical knife from these phantoms showed that using both devices results in the same measurements. Although a statistically significant difference was seen between the F/F+W of the Phantom 60% measured with needle probe and the measured with the smart electrosurgical knife, the difference was too small (60.10% and 61/38%) that would not affect the tissue discrimination. Usually, tissue

classification is more difficult in the border area or location with mixed tissues that contain both connective and malignant tissue. In those areas, the fat content of the tissues is more similar which complicates the tumor margin detection [5]. The extent to which these small variations, such as the one detected between the F/F+W of the Phantom 60% or other disparities between the F/W-ratio measured with a needle probe and the smart electrosurgical knife, could affect human breast tissue classification is a subject that may be explored in future studies using an ex vivo lumpectomy sample experiment.

The considerable difference between the F/W-ratio of the Phantom 100% measured with a smart electrosurgical knife and the probe are due to the fact that in higher fat percentages small deviations in F/F+W results in large deviations in F/W-ratios. However, in reality, the effect of this variation on tissue detection could be insignificant, since the difference between the fat content and the F/W-ratio of the breast malignant tissue and adipose tissue is very large [16].

The results of DRS measurement using the smart electrosurgical knife from the phantoms (Phantom 10%, Phantom 40%, and Phantom 60%) before and after electrosurgery indicated that even 14 minutes of electrosurgery with the high powers of 40 W and 60 W did not affect the accuracy of the prototype in detecting the F/W-ratio of the phantoms. These results showed that the encapsulation of the optical fibers in Design 2 can protect the fibers for at least 14 minutes of electrosurgery. While the results were statistically stable, and the differences in the numbers were negligible in this research, more investigation is required in the future on human tissue samples to analyze the magnitude of the effect of these small variations on the tissue discrimination power of the smart electrosurgical knife.

The experiment on the layered tissue and layered phantom showed the potential of the smart electrosurgical in detecting each layer based on its fat and water content. Besides, more remarkably, the results of these experiments revealed that the smart electrosurgical knife can predict the presence of the next layer before reaching it. Based on the F/F+W and F/W-ratio graph shown in Figure 4.8, it is perceptible that from 4 mm before the tip of the knife reaches the next layer, the measured fat content of the tissue increases or decreases depending on the fat content of the next layer. Based on the literature, the penetration depth of the light in the DRS probe increases by increasing the fiber distance [26, 27]. The results of the experiment on layered phantom showed that the smart electrosurgical knife renders detecting the changes in layers of the phantom from 4

mm ahead. Determining the maximum margin that the smart electrosurgical knife with the current design can detect before reaching the next layer can be an interesting topic for future research. During cancer surgery, the surgeon aims to achieve more than 2 mm of margin around the tumor to decrease the rate of positive margin and the recurrence rate [28, 29]. In 2019 Baltussen *et al.* investigated the effect of the tumor distance from the top surface on the accuracy of the tissue classification and showed that when an FD of 2 mm is used, the accuracy decreases when the distance of the tumor from the surface goes beyond 1.5 mm [30]. Hence, in this research, the large fiber distance of the smart electrosurgical knife has become beneficial in the scene that can accomplish the 4 mm detection depth. However, while all these assumptions are practical in a homogenous tissue or phantom, in reality, surgeons mostly face complex and heterogenous compositions of tissue in which the usability of the smart electrosurgical knife has not been tested yet. In future, the smart electrosurgical knife accuracy and detection depth need to be investigated on more complex tissue composition, either on ex vivo or in vivo breast tissue in locations where multiple tissues are present or on heterogeneous phantoms. Ultimately, in the next steps, tissue classification methods and algorithms can be developed to find the correlation between the changes in the F/W-ratio or the specific features on the spectrum to the type of specific tissue and the distance of the tip of the knife from it.

## 4.5 Conclusions

Our investigation revealed that, under various electrosurgery settings, the generated heat can reach temperatures exceeding 400 degrees. This study aimed to mitigate the associated challenges, particularly heat-induced optical changes and debris attachment, through the implementation of design enhancements in the smart electrosurgical knife. Design 2, distinguished by its incorporation of quartz and PTFE tubes, emerged as the most promising iteration and underwent further examination under realistic setups, including interrupted electrosurgery modes. The results underscored the remarkable resilience of Design 2, demonstrating its ability to provide reliable diffuse reflectance spectroscopy (DRS) measurements on porcine tissue and tissue-mimicking phantoms, even after prolonged electrosurgery sessions lasting up to fourteen minutes. Furthermore, the smart electrosurgical knife's design facilitated real-time measurements during electrosurgery on layered porcine tissue and a layered phantom. This capability, evident in detecting transitions between tissue/phantom layers with varying fat and water content

and predicting the fat content of the next layer from a distance of 4 mm ahead, holds significant promise for precise intraoperative margin assessment.

Our findings not only confirm the resilience and reliability of the smart electrosurgical knife in challenging surgical conditions but also underscore its potential significance for future applications. Particularly in surgeries where precise tissue discrimination is essential, the successful real-time measurements during electrosurgery and the predictive capabilities for tissue characteristics highlight the device's promising role in enhancing surgical precision and ultimately contributing to optimal clinical outcomes.

## Bibliography

- [1] J. Heidkamp *et al.*, “Novel imaging techniques for intraoperative margin assessment in surgical oncology: A systematic review,” *International journal of cancer*, vol. 149, no. 3, pp. 635-645, 2021.
- [2] J. W. Spliethoff *et al.*, “In vivo characterization of colorectal metastases in human liver using diffuse reflectance spectroscopy: toward guidance in oncological procedures,” *Journal of biomedical optics*, vol. 21, no. 9, pp. 097004, 2016.
- [3] R. Nachabé *et al.*, “Diagnosis of breast cancer using diffuse optical spectroscopy from 500 to 1600 nm: comparison of classification methods,” *Journal of biomedical optics*, vol. 16, no. 8, pp. 087010, 2011.
- [4] R. Nachabé *et al.*, “Effect of bile absorption coefficients on the estimation of liver tissue optical properties and related implications in discriminating healthy and tumorous samples,” *Biomedical optics express*, vol. 2, no. 3, pp. 600-614, 2011.
- [5] L. L. de Boer, “Detecting breast cancer tissue with diffuse reflectance spectroscopy,” University of Twente, University of Twente, 2019.
- [6] J. W. Spliethoff *et al.*, “Spectral sensing for tissue diagnosis during lung biopsy procedures: The importance of an adequate internal reference and real-time feedback,” *Lung Cancer*, vol. 98, pp. 62-68, 2016.
- [7] M. S. Nogueira *et al.*, “Evaluation of wavelength ranges and tissue depth probed by diffuse reflectance spectroscopy for colorectal cancer detection,” *Scientific Reports*, vol. 11, no. 1, pp. 1-17, 2021.
- [8] G. Einstein *et al.*, “Diffuse reflectance spectroscopy for monitoring physiological and morphological changes in oral cancer,” *Optik*, vol. 127, no. 3, pp. 1479-1485, 2016.
- [9] V. G. Prabitha *et al.*, “Detection of cervical lesions by multivariate analysis of diffuse reflectance spectra: a clinical study,” *Lasers in medical science*, vol. 31, no. 1, pp. 67-75, 2016.
- [10] A. Keller *et al.*, “Diffuse reflectance spectroscopy of human liver tumor specimens—towards a tissue differentiating optical biopsy needle using light emitting diodes,” *Biomedical optics express*, vol. 9, no. 3, pp. 1069-1081, 2018.
- [11] Y. Zhang *et al.*, “Diffuse reflectance spectroscopy as a potential method for nonmelanoma skin cancer margin assessment,” *Translational Biophotonics*, vol. 2, no. 3, pp. e20200001, 2020.
- [12] A. Garcia-Uribe *et al.*, “In vivo diagnosis of melanoma and nonmelanoma skin cancer using oblique incidence diffuse reflectance spectrometry,” *Cancer research*, vol. 72, no. 11, pp. 2738-2745, 2012.
- [13] R. Nachabé, “Diagnosis with near infrared spectroscopy during minimally invasive procedures,” Erasmus University Rotterdam, 2012.
- [14] R. Nachabé *et al.*, “Estimation of biological chromophores using diffuse optical spectroscopy: benefit of extending the UV-VIS wavelength range to include 1000 to 1600 nm,” *Biomedical optics express*, vol. 1, no. 5, pp. 1432-1442, 2010.
- [15] L. L. De Boer *et al.*, “Towards the use of diffuse reflectance spectroscopy for real-time in vivo detection of breast cancer during surgery,” *Journal of translational medicine*, vol. 16, no. 1, pp. 1-14, 2018.

[16] L. L. de Boer *et al.*, "Fat/water ratios measured with diffuse reflectance spectroscopy to detect breast tumor boundaries," *Breast Cancer Res Treat*, vol. 152, no. 3, pp. 509-18, Aug, 2015.

[17] S. A. Amiri *et al.*, "Intraoperative tumor margin assessment using diffuse reflectance spectroscopy: the effect of electrosurgery on tissue discrimination using ex vivo animal tissue models," *Biomedical optics express*, vol. 11, no. 5, pp. 2402-2415, 2020.

[18] M. W. Adank *et al.*, "Real-time oncological guidance using diffuse reflectance spectroscopy in electrosurgery: the effect of coagulation on tissue discrimination," *Journal of biomedical optics*, vol. 23, no. 11, pp. 115004, 2018.

[19] S. A. Amiri *et al.*, "Electrosurgical knife equipped with diffused reflectance spectroscopy sensing for tumor margin detection during breast conserving surgery: a phantom study," in Proc. SPIE 11631, Year, pp. 49-57.

[20] F. C. Meeuwesen, "Safe surgical signatures," Mechanical, Maritime and Materials Engineering, Delft University of Technology, 2019.

[21] S. A. Amiri *et al.*, "Tissue-mimicking phantom materials with tunable optical properties suitable for assessment of diffuse reflectance spectroscopy during electrosurgery," *Biomedical optics express*, vol. 13, no. 5, pp. 2616-2643, 2022.

[22] R. Nachabe *et al.*, "Estimation of lipid and water concentrations in scattering media with diffuse optical spectroscopy from 900 to 1600 nm," *Journal of biomedical optics*, vol. 15, no. 3, pp. 037015, 2010.

[23] T. J. Farrell *et al.*, "A diffusion theory model of spatially resolved, steady-state diffuse reflectance for the noninvasive determination of tissue optical properties in vivo," *Medical physics*, vol. 19, no. 4, pp. 879-888, 1992.

[24] T. M. Bydlon *et al.*, "Chromophore based analyses of steady-state diffuse reflectance spectroscopy: current status and perspectives for clinical adoption," *Journal of biophotonics*, vol. 8, no. 1-2, pp. 9-24, 2015.

[25] F. Mollerus, "The integration of diffuse reflectance spectroscopy into the electrosurgical knife used during breast-conserving surgery," Mechanical, Maritime and Materials Engineering, Delft University of Technology, 2018.

[26] H. Arimoto *et al.*, "Depth profile of diffuse reflectance near-infrared spectroscopy for measurement of water content in skin," *Skin Research Technology*, vol. 11, no. 1, pp. 27-35, 2005.

[27] R. Hennessy *et al.*, "Effect of probe geometry and optical properties on the sampling depth for diffuse reflectance spectroscopy," *Journal of biomedical optics*, vol. 19, no. 10, pp. 107002, 2014.

[28] C. Kunos *et al.*, "Breast Conservation Surgery Achieving  $\geq$  2 mm Tumor-Free Margins Results in Decreased Local-Regional Recurrence Rates," *The Breast Journal*, vol. 12, no. 1, pp. 28-36, 2006.

[29] N. Houssami *et al.*, "The association of surgical margins and local recurrence in women with early-stage invasive breast cancer treated with breast-conserving therapy: a meta-analysis," *Annals of surgical oncology*, vol. 21, no. 3, pp. 717-730, 2014.

[30] E. Baltussen *et al.*, "Tissue diagnosis during colorectal cancer surgery using optical sensing: an in vivo study," *Journal of translational medicine*, vol. 17, no. 1, pp. 1-10, 2019.



# 5

## Pre-Clinical evaluation of Smart electrosurgical knife

Despite advancements in margin assessment technologies, the challenge of unsuccessful tumor border detection and incomplete resection during tissue-sparing cancer surgery persists without a satisfactory solution. This chapter outlines initial validation steps for the smart electrosurgical knife in a pre-clinical setting, divided into two parts. Part 1 evaluated different designs of the smart electrosurgical knife using animal tissues. Seven surgeons (experts and trainees) provided feedback on the designed electrodes and the performance of the smart electrosurgical knife during electrosurgery on ex-vivo animal tissue. In Part 2, a surgeon assessed the knife's effectiveness in tumor resection using four phantoms with simulated tumors. The surgeon performed tissue-sparing surgeries on two phantoms with the smart electrosurgical knife, which provides real-time feedback, and on two phantoms with a conventional knife guided only by pre-operative images. The smart electrosurgical knife used indocyanine green (ICG) to detect tumor tissue, aiding the surgeon in making precise incisions. Results from Part 1 indicated a preference among surgeons for a narrower electrode width with a sharper, yet not excessively sharp, and more defined edge for the smart electrosurgical knife. In Part 2, the smart electrosurgical knife achieved complete tumor resection in one phantom and left a small residue in the second. In contrast, conventional knife surgeries resulted in incomplete resections with significant tumor residues. The experiments demonstrated that the smart electrosurgical knife offers real-time feedback, improving precision and aiding in achieving negative margins during cancer surgeries.

## 5.1 Introduction

One of the challenges faced by surgeons during tissue-sparing cancer surgery is the thorough detection of the tumor margin to ensure complete tumor resection and achieve negative margins while minimizing collateral damage to surrounding tissue. In case of positive margin diagnosis, the surgery is not fully successful, requiring reoperation or a more robust treatment approach to eliminate the cancer progression. This can lead to increased rate of local recurrence, decreased patient satisfaction and an increased rate of morbidity and mortality. The increasing number of patients diagnosed with cancer who are eligible for tissue sparing surgery demands the adoption of new technologies and approaches to improve the outcome of the surgery [1].

An accurate margin detection technique can greatly assist the surgeon in identifying the border of the cancerous growth, distinguishing healthy or negative margins, and guiding them in achieving a complete tumor resection. Several intraoperative margin assessment techniques, including gross histology, frozen section and imprint cytology, have been tested and shown promising results in reducing the positive margin rate [2].

New emerging techniques for intraoperative tumor margin assessment, such as micro-computed tomography [3], fluorescence imaging [4], Raman spectroscopy [5], optical coherence micro-elastography [6], specimen mammography [7], edge illumination x-ray phase contrast [8], ultrasound imaging [9], impedance spectroscopy [10], and mass spectroscopy [11, 12], are showing remarkable promise and potential. Ongoing research is continually exploring their effectiveness and applications. These cutting-edge methods may have the potential to offer improved efficiency and accuracy, minimized tissue destruction, and enhanced ease of use compared to traditional approaches. As the field of intraoperative tumor margin assessment continues to evolve, one particularly promising technique that has attracted significant attention is Diffuse Reflectance Spectroscopy (DRS). DRS is an optical based technique that can assess the characteristics of the tissue real-time and non-invasively. DRS has been used to identify and measure the main distinguishing factors between healthy and tumor tissues for different types of cancer [13, 14]. As a result, it has proven effective in recognizing the differences between healthy and malignant tissues across different types of cancers. For instance, studies have demonstrated that the main discriminative factor between malignant and healthy breast tissue is the difference between fat and water content. By measuring the Fat/Water-ratio of the tissue, DRS is capable of accurately identifying the

cancerous growth in breast [15]. In another study, researchers have shown that DRS can effectively detect tumor tissue from healthy tissue in the liver by measuring the bile content of the tissue [16]. DRS has found application in detecting malignant growth in various organs including lung [17], colorectal cancer [18], oral cancer [19], melanoma [20] and cervix [21].

Recently, we have made significant progress in developing a smart electrosurgical knife with the aim of incorporating DRS into the standard workflow of cancer surgery [22-24]. In this innovative device, the DRS technique has been integrated into a regular electrosurgical knife. The advantage of the smart electrosurgical knife lies in its ability to provide the user with rapid, real-time tissue feedback during electrosurgery. DRS not only enables discrimination between tumor and healthy tissue but also shows promise in identifying various types of healthy tissue, thereby also serving for safeguarding delicate structures such as nerves that surgeons aim to protect from damage (although this is beyond the scope of this thesis, it suggests a potential direction for future device enhancements) [25]. Unlike the invasive techniques that diagnose tissue only after it has been damaged such as frozen section [23], DRS can detect tissue characteristics beforehand, thus preventing unnecessary damage. Our previous experiments have demonstrated that the smart electrosurgical knife can sense tissue changes up to 4 mm ahead, rendering it an invaluable tool for anticipatory tissue assessment [24]. With the smart electrosurgical knife, users can identify tissue in depth prior to incision, empowering them to make informed decisions about tissue manipulation toward tumor tissue. Moreover, we have shown that the design of the smart electrosurgical knife ensures that the electrosurgery does not interfere with the performance of DRS in tissue recognition [22, 24]. The smart electrosurgical knife represents a cost-effective and straightforward solution, eliminating the need for additional tissue/patient preparation. This non-invasive and non-destructive technique provides real-time and rapid tissue feedback, making it a promising candidate for intraoperative margin assessment in tissue-sparing cancer surgery [22, 24].

The smart electrosurgical knife consists of a standard electrosurgical knife modified with a specially designed electrode to integrate optical fibers inside it. These optical fibers connect to a DRS console, allowing for tissue measurements during surgery. So far, we have conducted extensive research to demonstrate the effectiveness of the smart electrosurgical knife as a real-time tissue detection technique. However, it's important to

note that, to date, there has been no clinical research or feedback from surgeons to validate the performance of this technique in a more realistic surgical setting.

To take the first step towards validation of the device in a clinical setting, experiments were conducted in two parts in collaboration with surgeons.

In Part 1, various designs of the smart electrosurgical knife were developed and produced. In our previous work, we successfully integrated the optical fibers of DRS into an electrosurgical knife, creating a smart electrosurgical knife with tissue recognition capabilities. We demonstrated that the smart electrosurgical knife, with its specific design, ensures the reliable performance of DRS during electrosurgery across various modes and power settings [22, 24]. In this chapter, we will employ the same combinations of components as the previous design of the smart electrosurgical knives. However, we have devised different structural designs for the knife's electrode and alternative approaches to the placement of these components. The purpose of these modifications is to explore the knife's cutting effectiveness from the perspective of clinicians, evaluating its practical usefulness in surgical procedures. Subsequently, we sought to gather feedback from surgeons regarding the electrosurgical performance of different probe designs on animal tissue.

In Part 2, a surgeon were asked to perform tissue-sparing cancer surgery on tissue phantoms. Tissue-mimicking phantoms were specifically produced for this experiment. Subsequently, a platform was developed prior to the surgery to provide feedback to the surgeon during the procedure. The surgeon used both regular electrosurgical knives (without feedback) and the smart electrosurgical knives (with feedback) to obtain a preliminary assessment of the effectiveness of the smart electrosurgical knife in achieving negative margins. This study bridges the gap between laboratory research and real-world surgical settings, providing more insights for the future development and implementation of the smart electrosurgical knife in cancer surgery.

## 5.2 Materials and Methods

### 5.2.1 Part 1: Evaluating the usability of the smart electrosurgical knife by surgeons

#### 5.2.1.2 Design and develop the new electrodes

In our previous work, the design of the blade of the smart electrosurgical knife incorporates quartz tubes (Hengshui Yuanbo Import And Export Co, China) to encase

the optical fibers of the DRS console near the electrode tip, safeguarding them from debris attachment and contamination. Additionally, Polytetrafluoroethylene (PTFE) tubes (Zeus Industrial Products, Inc., United States) are employed around the quartz to shield the optical fibers from high temperatures during electrosurgery. Finally, metallic tubes are utilized to securely position this combination onto the electrode.

To explore the cutting effectiveness from the surgeon's perspective, electrosurgical knives with three different electrodes were developed and tested (EL1, EL2, and EL3) (see Figure 5.1). EL1 was designed with the optical fiber configured on the sides of a blade-shaped electrode. This new electrode featured a rounded tip. In EL2, the combination of optical fibers was positioned on the top side of a blade-shaped electrode. As a result, the sides of the electrode became thinner while the electrode itself became thicker. While EL1 and EL2 designs necessitate the creation of entirely new types of electrodes for the electrosurgical knife, EL3 was designed to serve as an add-on to the regular blade shape electrode. EL3 has two distinct pieces. The first piece resembles a clip-on part, featuring the optical fibers configured on its sides and a 'tail' used for attachment. The second piece is a regular blade-shaped electrode typically found in the electrosurgical knife, but featuring a recess in the middle of the blade. The first piece can be slid over the second piece. The tail can then be placed in the recess for fixation.

All electrodes (for EL3 only the first piece) were crafted from a solid piece of stainless steel. The holes required for the placement of the optical fibers were created using a 1.1 mm drill. Subsequently, the body of the electrodes underwent shaping using wire-based electrical discharge machining (EDM). Once the electrodes were prepared, the optical fibers were carefully inserted into the quartz tubes, and both were then enclosed within the PTFE tubes. Subsequently, this assembly was placed into the holes of the electrodes.

#### *5.2.1.2 Evaluation during the electrosurgery*

To assess the practicality of the new concepts, surgeons and surgical trainees from the Department of Surgical Oncology, Erasmus MC, University Medical Center Rotterdam, were invited to perform electrosurgery on animal tissue using the newly developed tools. The evaluation process involved attaching the electrodes to the regular electrosurgical knife (WEIDE, Hangzhou Valued Medtech Co.,Ltd, China). Subsequently, the electrosurgical knife was connected to an electrosurgical unit (Force FX, Valleylab, Medtronic plc, USA), with the electrosurgery setting set to 35 W.

Porcine belly tissue on room temperature (sourced from a local supermarket) was placed on the top surface of the back electrode of the electrosurgical unit. The surgeons were instructed to perform electrosurgery on the animal tissue using two different types of knives. Firstly, they used a regular electrosurgical knife with a normal blade-shaped electrode. Subsequently, they cut the animal tissue using the smart electrosurgical knives with the new electrodes, once in "Cut" mode (intended for cutting the tissue) and once in "Coagulate" mode (used for coagulating the tissue).

After completing the procedure, the clinicians filled out a questionnaire to rate the performance of the smart electrosurgical knife designs for both modes. The ratings were converted to a scale ranging from -3 to 3, where 3 indicates that the new design performs similarly or better to a standard electrode, 0 suggests that it is good enough for use in electrosurgery, and -3 implies that the design is unusable.

## 5.2.2 Tissue sparing surgery on the phantom

To assess the effectiveness of the smart electrosurgical knife, a surgeon was assigned the task of performing tissue sparing surgery on tumor-containing phantoms using the device. The following sections provide detailed information about the materials and methods employed in conducting this experiment.

### 5.2.2.1 *Phantom production*

To evaluate the effectiveness of the smart electrosurgical knife in a practical scenario, a tumor-containing tissue phantom was developed. In this setup, Indocyanine green (ICG) was utilized as the primary distinguishing factor between the tumor and the surrounding tissue. ICG has a strong absorption around 800 nm wavelength which can be detected using the DRS but is invisible for the human eye. For the phantom to be suitable for electrosurgery, it must have electroconductive properties. Additionally, the material needs to withstand the heat generated during electrosurgery without excessive melting.

To produce the phantom, semi-skimmed milk was heated to 50°C and 15 wt% gelatin powder (ES1477, Natural Spices) was added while stirring on a heater-stirrer. The temperature was raised to 80°C before turning off the heater. Then 0.1 wt% Sodium Benzoate (Sigma-Aldrich, USA) as a preservative agent and 2 wt% Transglutaminase (Unique Products Schuurman, Netherlands) as a cross-linker were added, forming a homogeneous emulsion [26]. This mixture represented the healthy tissue surrounding the

tumors (healthy tissue-mimicking material). Next, the healthy tissue material was poured into a mold, and tumor pieces were randomly placed inside. The phantom stayed an hour in the freezer and then 12 hours in the fridge. The tumor component was created using a similar mixture, but with 2 wt% Barium sulfate (Hinmeijer, Netherlands) as a contrast agent for X-ray imaging and ICG-dye with concentration of 2  $\mu$ M. The amounts of ICG and barium sulfate were carefully selected to ensure that adding them to the phantom material would not alter its color. This way, the distinction between healthy and tumor material remains invisible to the naked eye.

The tumor material was poured into small molds of various shapes and solidified in the freezer for an hour before removing the tumor pieces to place them inside the phantom. On the day of the experiment, the phantoms were removed from the molds and utilized for conducting the experiment.

#### *5.2.2.2 Pre-surgery: Preparing feedback platform*

SCFS The aim of this part of the method was to develop a feedback platform to assist the surgeon, a task undertaken by the operators (not the surgeon) prior to the surgery in the hospital. This involved several steps. Firstly, a look-up chart was created containing the spectral responses of the tissue-mimicking materials representing both healthy and tumor tissues. This chart can be used to provide the surgeon with information about the distance of the probe from the tumor tissue, aiding in guided surgery using the smart electrosurgical knife. Secondly, preoperative images of the phantom were taken to provide the surgeon with approximate location and shape information regarding the tumor insertions.

##### *Look-up chart*

To create the look-up chart of spectra, a two-layer phantom was constructed. The base layer was made of tumor material, and on top of it, a layer of healthy tissue-mimicking material with a precise depth of 8 mm was created. Moreover, a smart electrosurgical knife connected to a DRS console was used. The custom-designed Diffuse Reflectance Spectroscopy (DRS) setup (Philips Research, Eindhoven) comprises a light source (Avantes, The Netherlands) that emits light to the tissue through an optical fiber. Spectrometers (one spectrometer to collect the light in the wavelength range of 900 nm-1700 nm (NIRQuest 512, Ocean Optics, United States) and one to collect the light in the wavelength range of 400 nm-100 nm (Maya2000 Pro, Ocean Optics, United States)) then

collect the light from the tissue using another optical fiber, positioned at a distance from the emitting fiber. Through DRS, the spectral response of the tissue can be measured across a wide wavelength range (500 nm - 1600 nm in this case). The custom-designed DRS console by Philips, which was utilized in this research, features a screen that displays the measured spectrum in real-time. For more detailed information about the DRS console, refer to [22, 26, 27].

The smart electrosurgical knife was fixed on a vertical translation stage to adjust its height and horizontal movement, facilitating measurements from the top layer of the phantom. The process involved using the smart electrosurgical knife to take measurements on the top layer of the phantom. The knife was then moved down into the phantom by 1 mm increments, followed by DRS measurements. This procedure was repeated until the tip of the knife reached the top surface of the tumor-mimicking phantom. By following this method, a chart was created, displaying the DRS spectrum of the phantom for different distances from the tumor, ranging from 8 mm to 0 mm. This chart was made to enable the user to determine the distance of the tumor from the knife by comparing the real-time spectral response of the measured tissue shown on the screen of the DRS console with the data in the look-up chart.

#### *Pre-Operative images*

Furthermore, to provide the surgeon with pre-operative images of the phantoms, X-ray images from different angles, along with 3D views, were generated using a “Siemens® Somatom Volume Zoom CT scanner”.

#### *5.2.2.3 During the surgery: on the phantom*

The phantom surgery was conducted at the University Medical Center Rotterdam, using an electrosurgical unit and DRS console as previously described. A phantom surgery setup was arranged, comprising all necessary elements for the experiments, including the DRS console, the smart electrosurgical knife, electrosurgery setup, the back electrode, the phantoms, the look-up chart, and pre-operative images. The tumor-containing phantom was positioned on the back electrode of the electrosurgical unit. The smart electrosurgical knife, featuring the EL1 design, was connected to both the electrosurgical unit and the DRS console. The EL1 electrode was chosen for this experiment because it received an acceptable score in the previous experiment (Part 1) and also because of its greater fiber distance, which allowed for deeper tissue scanning.

Prior to initiating the surgery, the DRS setup with the connected electrosurgical knife was calibrated following the steps mentioned in reference [26, 27].

An experienced oncological surgeon, with ten years of electrosurgery experience, participated in the experiment. The surgeon was first familiarized with the DRS console and smart electrosurgical knife, along with the reference look-up chart. The relationship between the spectral response and the distance of the knife from the tumor was explained. During the surgery, the surgeon was given the freedom to electrosurgically remove the tumor piece from the phantoms, using pre-operative X-ray images for tumor location estimation. For the guided surgeries using the electrosurgical knife, the DRS console was set up to conduct optical measurements automatically every 0.4 seconds. An operator announced the distance of the knife from the tumor loudly, providing real-time feedback by comparing the surgeon's measured spectrum with the look-up chart. The surgery concluded once the surgeon excised the tumor specimen from the phantom and checked for any residue in the formed cavity using the smart electrosurgical knife. Additionally, the surgeon performed the same surgeries on other phantoms using a regular electrosurgical knife (without DRS console and optical feedback), relying solely on pre-operative X-ray images for guidance.

In this experiment, four phantoms (Phantom 1, Phantom 2, Phantom 3, and Phantom 4) were utilized. Surgeries on Phantom 1 and Phantom 4 were conducted using a smart electrosurgical knife, with the surgeon receiving feedback from the operator (guided surgery). Surgeries on Phantom 2 and Phantom 3 were performed using a normal electrosurgical knife without any feedback from the operator (unguided surgery).

#### *5.2.2.4 Post-surgery: margin detection*

Following the surgeries, the excised specimens and phantoms from each experiment underwent visual inspection to determine the results of the surgeries. The previously mentioned X-ray imaging system was employed to capture images of both the phantoms and the extracted specimens. Additionally, since the ICG can be detected through fluorescence imaging, a fluorescence imaging system (Pearl Trilogy, LI-COR Biosciences) was utilized to examine the phantoms and specimens, providing visual representation of the tumor margin and searching for any residue of the tumor inside the phantoms.

## 5.3 Results

### 5.3.1 Part 1: Evaluating the usability of the smart electrosurgical knife by surgeons

#### 5.3.1.1 Design and develop the new electrodes

Figure 5.1 presents the design of the electrodes and a visual representation of the final developed electrodes. In Figure 5.1, the small visible pieces extending from the holes of the electrodes correspond to the enclosed tips of the quartz tubes, where the optical fibers are securely placed. The fiber distance (FD) varied in each electrode depending on the design, with FDs of 3.5 mm, 2.1 mm, and 4.3 mm for EL1, EL2, and EL3, respectively.

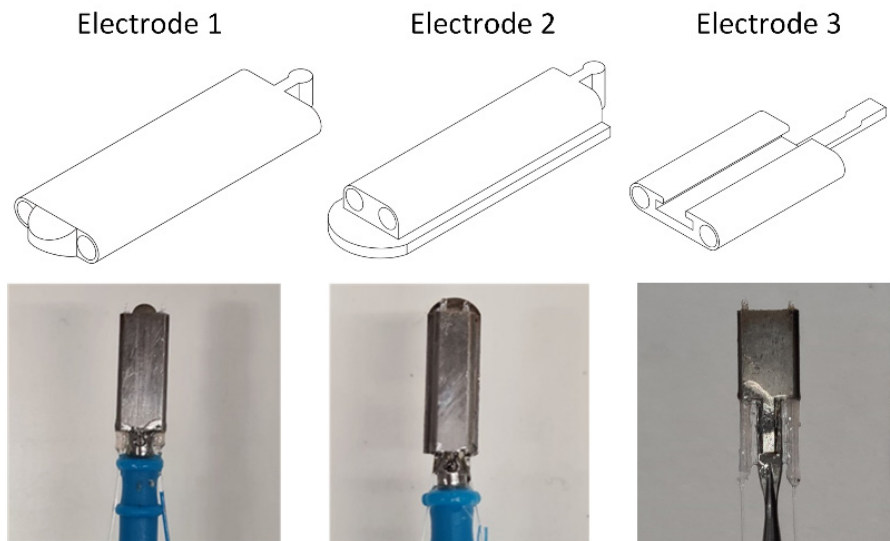


**Figure 5.1.** Illustration of the design of the electrodes and the final developed electrodes ready for validation.

#### 5.3.1.2 Evaluation during the electrosurgery

The results of the quantified rating of electrodes tested by surgeon on their electrosurgery performance is reported in Table 5.1. The test group consisted of seven individuals, including four experienced surgeons and three surgeons in training. The surgeons in training had 3, 3, and 5 years of experience with the electrosurgical knife, while the experienced surgeons had 7, 10, 18, and 18 years of experience. EL2 received the highest scores for both electrosurgery modes, followed by EL1, indicating that both

electrodes are well-suited for electrosurgery. On the other hand, EL3 showed the lowest results among the three electrodes, rendering it unsuitable for further investigations.

**Table 5.1.** Testing the design by surgeons

	CUT			COAG		
	EL1	EL2	EL3	EL1	EL2	EL3
<b>Surgeon 1</b>	-1	1	-2	0	0	-2
<b>Surgeon 2</b>	0	-1	-2	0	-1	-1
<b>Surgeon 3</b>	0	2	0	0	2	0
<b>Surgeon 4</b>	0	2	1	1	3	2
<b>Surgeon 5</b>	0	1	-3	0	0	-1
<b>Surgeon 6</b>	-2	-1	-3	-1	-1	-3
<b>Surgeon 7</b>	1	1	-2	1	1	-1
<b>Averaged Score</b>	-0.29	0.71	-1.57	0.14	0.57	-0.86

All the surgeons scored the performance of EL1 and EL3 with either no improvement or a higher score when using "Coag" (coagulation mode) mode compared to "Cut" mode during electrosurgery. This improvement is also evident in the averaged scores of these two blades in different modes. EL2 did not exhibit a consistent pattern of score changes when switching from "Cut" to "Coag" mode.

Overall, the surgeons emphasized that the performance of a blade depends on the dimensions and edges of the blade and the final cut on tissue. A blade with a thinner and narrower tip and a sharper edge (without being excessively sharp to prevent accidental cutting when not in use) allowed for more precise cuts, making wider blades and ones with thick edges less practical in comparison. Furthermore, users also noted that evaluating the electrodes in coagulation mode might not be entirely accurate, as the ex-vivo animal tissue lacked blood perfusion and active bleeding.

### 5.3.2 Part 2: Tissue sparing surgery on the phantom

#### 5.3.2.1 Phantom production

The developed tumor-containing tissue phantoms, utilizing Indocyanine green (ICG) as the primary distinguishing factor, were successfully prepared. In Figure 5.2 the produced tumor containing phantom is shown.



**Figure 5.2.** The tumor containing phantoms

#### 5.3.2.2 Pre-surgery: Preparing feedback platform

To produce the look-up chart, a two-layered phantom was produced (as shown in Figure 5.3(A)), where the border between the tumor and healthy tissue mimicking material was not visible to the naked eye.

Following the measurements on the layered phantom with 1 mm increment steps, the look-up (reference) chart was created, as shown in Figure 5.3(B). The DRS spectrum at 8 mm in this figure represents the optical response of the healthy tissue mimicking material. Indeed, the dents around 800 nm and 1000 nm correspond to the wavelength range of the main absorption of fat (at 760 nm, 930 nm, and 1042 nm) and water (755 nm and 972 nm) [28] – the main components of the milk, which serves as the base material

for the phantom. The spectral responses displayed in the chart demonstrate a clear trend: as the electrosurgical knife approaches the tumor tissue, the dent around 800 nm (representing the absorption peak of the ICG) becomes more pronounced and narrower, particularly starting from a distance of 5 mm. By analyzing the intensity and position of this dent in relation to the one close to 1000 nm, it becomes possible to estimate the depth at which the tumor border begins.

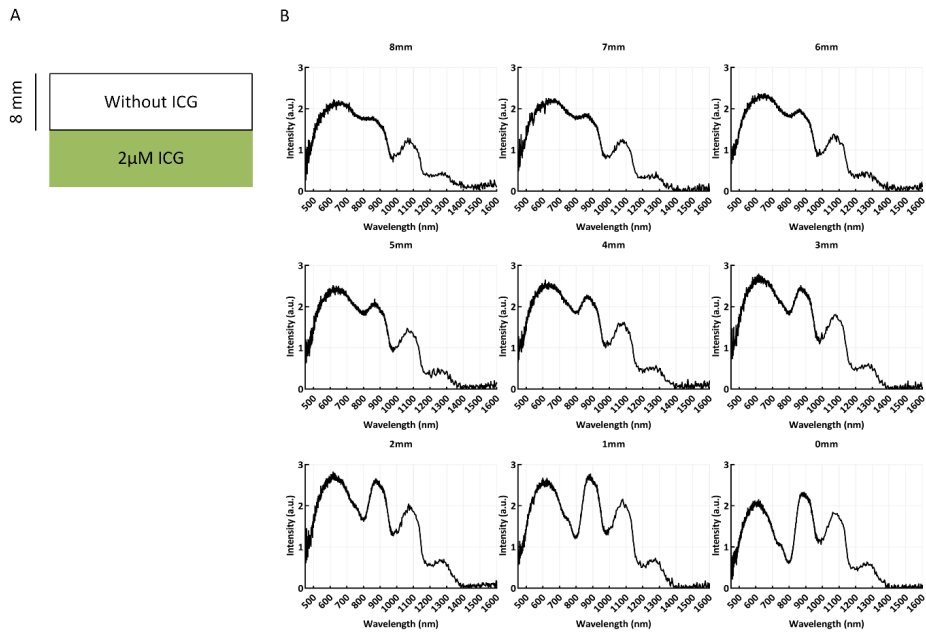


**Figure 5.3.** (A) Illustration of the two-layered phantom, with the tumor layer located at the base and an 8 mm healthy tissue mimicking material placed on top (the green color is for illustrative purposes only, as there was no visible color difference between the layers to the naked eye) . (B) Look-up chart with DRS spectra obtained from the layered phantom at 1 mm increment steps from top to bottom.

Additionally, pre-operative X-ray images from various angles of the phantom were made available to the surgeon, as illustrated in Figure 5.4. The incorporation of Barium Sulfate in the tumor mimicking material enhanced the visibility of the tumors in X-ray images, creating a contrast between the tumor and the surrounding tissue without altering the visibility for the human eye. This contrast X-ray image enabled the surgeon to estimate the location of the tumors inside the phantom.

### 5.3.2.3 During the surgery: on the phantom

To commence the tissue sparing surgery on the phantom, the setup depicted in Figure 5.5 was assembled.

During the surgery, the surgeon chose to halve the phantom shown in Figure 5.2 and 4 and perform two surgeries on the resulting pieces. This decision was made because the phantom's higher stiffness and density made it challenging for surgeons to maneuver as freely as they would in real surgery. Another observation noted during the surgery was the slight melting of the phantom material due to the heat generated during electrosurgery. To manage this, any excess melted material was promptly wiped away from the surgical site by a resident who assisted the surgeon throughout the procedure.

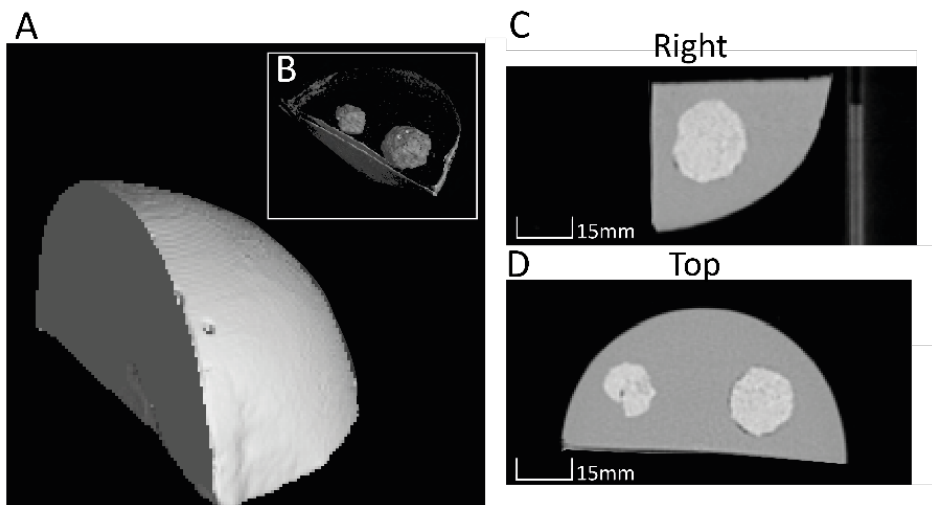
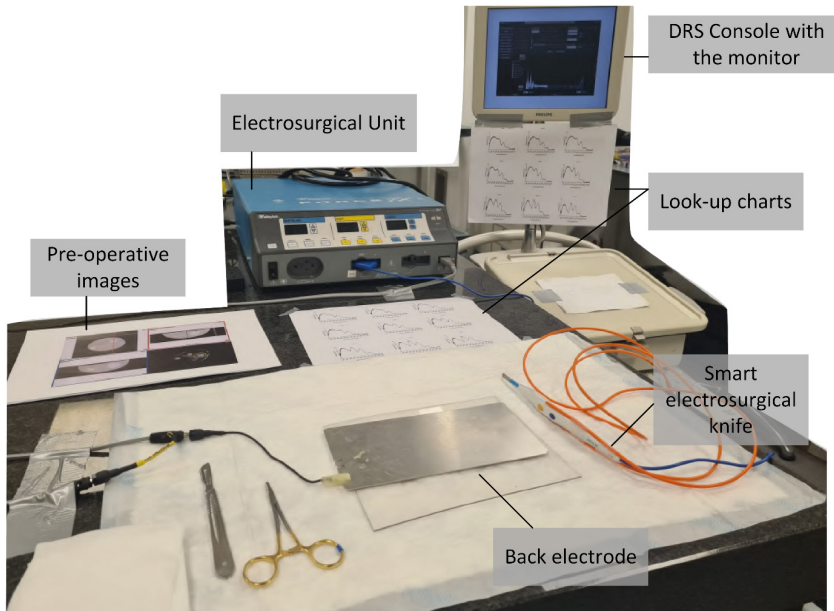


**Figure 5.4.** Pre-operative X-ray images from multiple angles of the phantoms. (A) Illustrating the phantom. (B) 3D positioning of the tumor insertions inside the phantom. (C) and (D) Top and side views of the phantom. The light grey insertions indicate the locations of the tumor mimicking material inside the phantom.

### 5.3.3.4 Post-surgery: margin detection

In Figure 5.6 and Figure 5.7, the results of post-operative imaging from the phantoms are presented. Tumor excision from the phantoms shown in Figure 5.7 were accomplished using the smart electrosurgical knife with tissue feedbacks from the DRS operator, while the surgery on the phantoms in Figure 5.6 was carried out using a regular electrosurgical knife without any optical feedback. In both figures (A and B), the first rows display the post-operative images from the phantoms using the CT scanner, once without

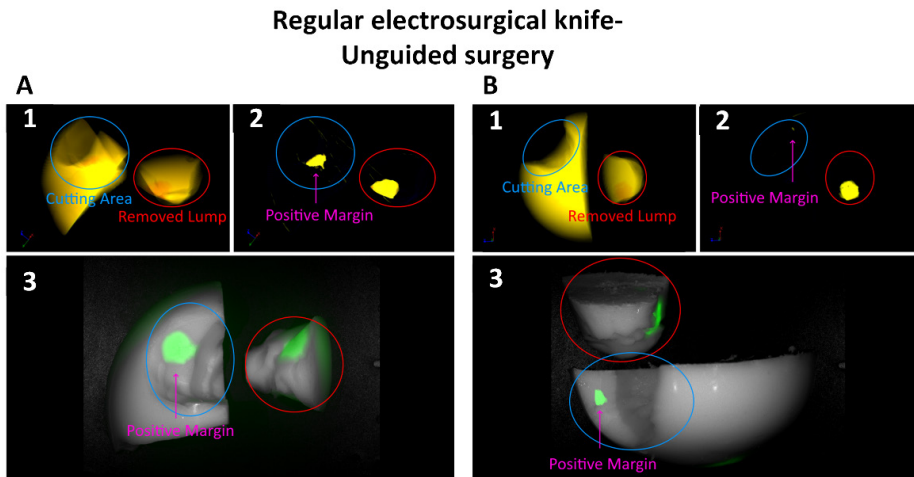
filtering (1) and once with the healthy tissue filtered out (2), while the bottom row (3) shows the images obtained from the fluorescence imaging system.



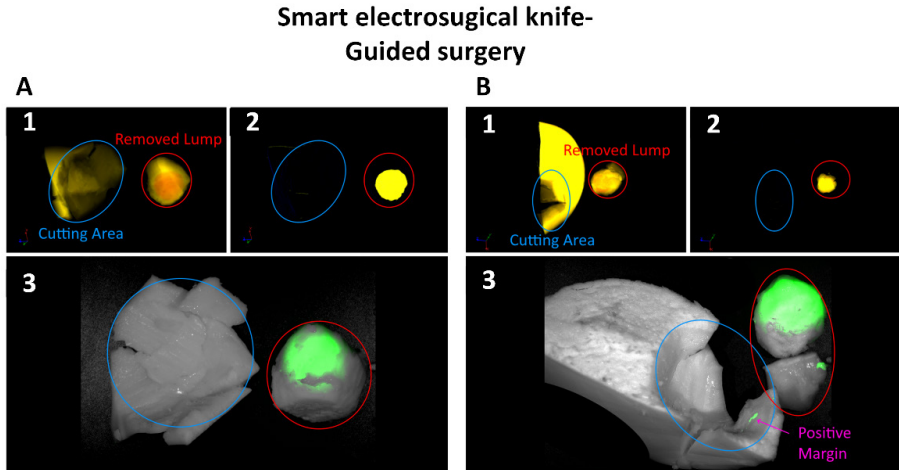
**Figure 5.5.** Setup for performing tissue sparing surgery on the phantom

Figure 5.6(A3) and 5.6(B3) reveals the presence of green residue from the tumor inside the Phantom 2 and Phantom 3, indicating a positive margin incident when a regular electrosurgical knife was used for surgeries. This is further evident in Figure 5.6 (A1&2) and 5.6(B1&2), where a small part of the tumor (orange in 5.6(B1) and yellow in 5.6(B2)) remained inside the phantom after the surgery.

When the surgeon utilized the smart electrosurgical knife with optical feedback, complete tumor extraction from the Phantom 1 was achieved (Figure 5.7(A)). There was no evidence of tumor tissue remaining (in orange in Figure 5.7(A1) or yellow in 5.6(A2)) in the CT scans. The tumor contains ICG, causing the tumor mimicking material to fluoresce green in the fluorescence images (Figure 5.7(A3)). As shown in Figure 5.7(A3), no residue of the tumor (green) was observed inside the phantom after the surgery using the smart electrosurgical knife.



**Figure 5.6.** Post-operative images from the phantoms used in unguided surgery (without smart electrosurgical knife) (A) Phantom 2 (B) Phantom 3. Top row (1, 2) shows CT scanner images, with (2) showing filtered healthy tissue. Bottom row (3) displays fluorescence imaging system images. In (1) the orange part indicates the tumor tissue, and the yellow material represents the healthy tissue. In (2) the healthy tissue is filtered out, and the tumor is shown in yellow. In (3) the green parts represent the tumor mimicking material inside the healthy tissue mimicking material (white).



**Figure 5.7.** Post-operative images from the phantoms used in guided surgery (using smart electrosurgical knife) (A) Phantom 1 (B) Phantom 4. Top row (1, 2) shows CT scanner images, with (2) showing filtered healthy tissue. Bottom row (3) displays fluorescence imaging system images. In (1) the orange part indicates the tumor tissue, and the yellow material represents the healthy tissue. In (2) the healthy tissue is filtered out, and the tumor is shown in yellow. In (3) the green parts represent the tumor mimicking material inside the healthy tissue mimicking material (white).

Figure 5.7(B) shows the pre-operative images of the Phantom 4 used in guided surgery. The tumor in Phantom 4 was located on the surface of the breast phantom and measured approximately 20 mm in diameter. While comparison of the CT scan images, as depicted in Figure 5.7(B1) and 5.6(B2), did not indicate the presence of any residual tumor phantom, fluorescence imaging revealed two contaminated areas. The green spot, found near the lump inside the red circle, was part of a small patch of phantom part removed after further inspection of the excised lump with the DRS device. Therefore, it should not be considered contamination but rather as error correction. The second green spot in the cutting area (blue circle) indicates a very small tumor residue that remained within the cutting area.

From Figure 5.6 and Figure 5.7 it is apparent that in most cases the tumor excised with the smart electrosurgical knife exhibits a margin of healthy tissue around it, while in the lump extracted using a regular electrosurgical knife, the tumor tissue is visible at the edges.

## 5.4 Discussion

While research on using diffuse reflectance spectroscopy for real-time tissue recognition is ongoing, this chapter explores the applicability of a DRS-integrated electrosurgical knife (smart electrosurgical knife) as an approach to incorporate DRS into the normal workflow of cancer surgery.

During DRS measurements, optical fibers, which are connected to the light source and spectrometers, need to be positioned close to the tissue to ensure a reliable optical response from the local tissue. As a result, positioning the optical fibers at the tip of the electrosurgical knife becomes essential. However, placing the optical fibers unprotected on the electrode tip of the electrosurgical knife presents a challenge, as the high heat generated during electrosurgery, coupled with debris accumulation, can rapidly degrade the optical fibers, rendering them unusable in less than a second [27]. Previously, we developed the smart electrosurgical knife design in a way that ensures electrosurgery does not compromise the effectiveness of DRS tissue recognition. In our previous works, we developed the smart electrosurgical knife design in a way that ensures electrosurgery does not compromise the effectiveness of DRS tissue recognition [22, 24]. In the first part of this chapter, we examined the design from a different perspective (clinical perspective). The integration of optical fibers into the electrosurgical knife introduces additional

material and bulk to the knife's electrode, which could potentially interfere with the electrosurgical treatment of the tissue. Initially, various designs for the electrode of the smart electrosurgical knife were developed. Subsequently, clinicians were tasked with utilizing these electrodes (EL1, EL2, and EL3) during electrosurgery. The feedback from the surgeons has clarified that a blade with a narrower width and a sharper edge is preferred. This design can lead to precise cuts with minimal tissue damage, as it creates narrower incisions and reduces the risk of tissue destruction. The study's limitation of encountering lack of blood perfusion and active bleeding in animal tissue during electrode evaluation in coagulation mode underscores a crucial consideration for future clinical studies involving the smart electrosurgical knife, whether applied on perfused phantoms or animal models.

For the subsequent iterations of the smart electrosurgical knife, EL1 was chosen for surgery on the phantom, whereas EL2 received slightly higher scores from the surgeons. This preference can be attributed to the distinct fiber distances of these electrodes. It is recognized that a greater fiber distance in DRS can lead to a deeper penetration of light, enabling the tissue read-out from greater depths within the tissue [29, 30]. Furthermore, we demonstrated that the smart electrosurgical knife with a fiber distance of 3.87 mm is capable of detecting changes in the underlying tissue as far as 4 mm ahead of its position [24]. This larger fiber distance can prove advantageous for surgeons during cancer surgery, as they often target a margin larger than 2 mm to ensure a negative margin [31, 32]. This phenomenon is also apparent in the spectrum response illustrated in the lookup chart. As observed with the electrosurgical knife, the alteration in the spectra at the 800 nm wavelength becomes more pronounced within a distance of 4-5 mm from the tumor-mimicking layer containing ICG.

One significant limitation of the tissue-sparing surgery performed on the phantom in this study was the lack of realistic mechanical properties in the chosen phantom material. The tissue-mimicking material used in the phantom exhibited greater stiffness and density than actual human tissue, such as breast tissue. Consequently, it became impractical for the surgeon to maneuver the tissue as they would typically do in a real surgical scenario. This variation led the surgeon to opt for a different approach: cutting the main phantom, containing two tumor insertions, in half and conducting separate surgeries on each half. Despite this challenge, the characteristics of the phantom prompted the surgeon to perform tumor excisions using the electrosurgical knife.

Guided surgery on Phantom 1 resulted in complete tumor resection. However, fluorescence images of Phantom 2 (Figure 5.7(B3)), after guided surgery, revealed a small green spot in the cutting area, indicating residual tumor remaining inside the phantom. While this spot is very small and not visible in X-ray images, unlike the tumor residues in Phantoms 2 and 3 used for unguided surgery, it can still be considered a positive margin.

The time error during the surgery might explain the presence of a small tumor residue in Phantom 4. One limitation of this experiment was the time delay between the surgeon's movements and receiving feedback from the operator. Measurements were taken every 0.4 seconds. After each measurement, the spectral response was displayed on the screen, and the operator compared it with the reference look-up chart to determine the distance of the probe from the tumor tissue. Consequently, the signal from the device was not directly translated into a distance but required interpretation by the operator, leading to increased error and time delay. As a result, measurement times were longer than preferred by the surgeon, leaving less time for reaction. This delay may have contributed to the inadvertent contact of the electrode of the smart electrosurgical knife with tumor tissue in Phantom 4 during the procedure. As mentioned before, the melting of the phantom material during electrosurgery, could result in contamination of the tumor material when the electrosurgery is done on the tumor material. Inspection using the smart electrosurgical knife after the excision of the first lump in this phantom revealed a small amount of remaining tumor tissue inside the cutting cavity. Aware of this, the surgeon proceeded to remove a second lump (depicted in Figure 5.7 within the red circle). This close incision to the tumor may have led to the melting of the tumor residue, causing it to remain inside the cavity.

These issues can be addressed in the future by enhancing the DRS setup and refining the properties of the phantom materials. The approach to providing the surgeon with feedback can be enhanced by automating the tasks performed by the operator in this experiment, thereby minimizing time delays and providing the surgeon with faster feedback, allowing for more informed decision-making. Additionally, increasing the heat resistance of the phantom materials can reduce the likelihood of tumor material melting. Moreover, using a blade with a sharper edge, such as EL2 in this experiment, could result in cleaner cuts and less tumor material melting. While using EL2 with a smaller fiber distance may lead to shallower tissue read-outs, future blade design could focus on

combining the sharp edges of EL2 with a larger fiber distance akin to EL1 for improved performance.

With the successful preliminary validation of the smart electrosurgical knife employing these specific electrodes, our attention turns towards envisioning the potential form of the final product. One option involves integrating the optical fibers within the body of the knife itself, as shown in Figure 5.8(A), transforming the entire knife into a cohesive, singular product. Alternatively, we could explore an approach where the DRS functionality functions as an add-on to the existing electrosurgical knife (Figure 5.8(B)). In this scenario, the add-on would feature an electrode equipped with optical fibers, allowing it to be attached to various electrosurgical knives through a wearable sleeve or clip-on mechanism, enhancing their capabilities. These possibilities open the door to innovative designs that align with both surgical precision and practicality.

An important aspect to take into account is the surgeon's routine practice of periodically cleaning the electrode's tip using gauze during surgery, as required. This practice becomes particularly relevant when certain segments of the optical fibers, as depicted in the design showcased in Figure 5.8(B), become exposed. Such exposure can lead to potential damage and dysfunctionality of the optical fibers. To address this concern, we must explore design iterations that ensure complete coverage of the entire length of the optical fibers on the electrosurgical knife. Furthermore, we observed that this cleaning process might accidentally lead to damage to the tip of the quartz tubes protruding from the electrode's tip. Based on the feedback received from the surgeons, beside design modifications, this issue also can be effectively resolved by providing comprehensive training to surgeons on the proper handling of the entire knife, alongside establishing specific cleaning protocols tailored for the smart electrosurgical knife.

Prior to the surgery, the surgeon was presented with two options: either to personally estimate the distance to the tumor by examining the monitor of the DRS console and comparing the measured spectrum with the look-up chart, or to have an operator perform this task and announce the tumor's distance whenever a change was detected. Curiously, the surgeon opted for the second choice, citing that adding extra tasks might distract her. The feedback from the surgeon persuaded the authors that future enhancements in the design of the smart electrosurgical knife should prioritize ease of use for surgeons. This could potentially involve incorporating audio guidance into the setup or integrating visual guidance directly into the body of the knife. This way, when surgeons

use the smart electrosurgical knife, they wouldn't need to shift their attention to the monitor of the DRS console by moving their heads.

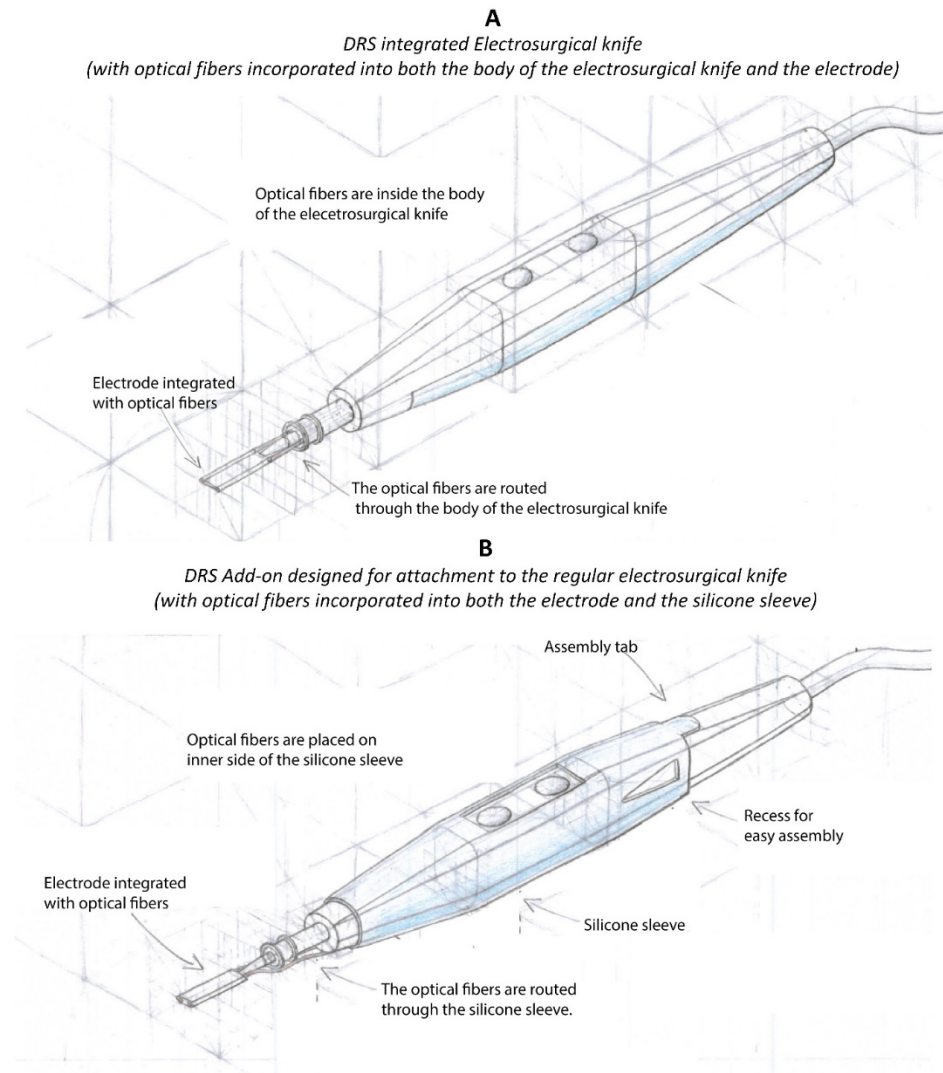


**Figure 5.8.** Conceptual Illustration of potential design directions for the Smart Electrosurgical Knife. (A) Integration of optical fibers within the body of the electrosurgical knife, presenting a unified and self-contained product. (B) DRS combined with the electrode in the form of an add-on module, attaching to different electrosurgical knives to enhance their capabilities. The design of the electrode is subject to modification.

While the outcomes of our prior research and the experiments conducted in this chapter showcase the significant potential of the smart electrosurgical knife to evolve into a standard margin assessment technique for tissue-sparing surgeries, further extensive clinical research on a larger scale are necessary to validate this proposition. Further clinical research can be directed towards conducting additional validation assessments for the usage of the electrosurgical knife, particularly in more realistic settings, such as a perfused phantom, *ex-vivo* tissue model or even *in-vivo* studies on animal tissues. Collaborative efforts with a broader range of surgeons across multiple hospitals could also contribute to a more comprehensive understanding of the smart electrosurgical knife's efficacy and potential applicability.

## 5.4 Conclusions

This study presents the pre-clinical application of a smart electrosurgical knife, achieved by integrating diffuse reflectance spectroscopy into a conventional electrosurgical knife, and incorporating feedback from its end-users. Two out of three prototypes were good enough to support a transition into clinical practice. Furthermore, this smart electrosurgical knife has the ability to accurately identify tissue variations in real time during surgery. This extra feedback enabled the surgeon to achieve a radical resection on a phantom model. This tool holds potential for transforming many types of surgeries, equipping the surgeon with real-time insights and therefore an enormous potential for improved patient care. However, the journey to establish this concept as a standard surgical practice mandates a continuous commitment to research, enhancement, and active engagement within the surgical community.

## Bibliography

- [1] J. Heidkamp *et al.*, "Novel imaging techniques for intraoperative margin assessment in surgical oncology: A systematic review," *Int J Cancer*, vol. 149, no. 3, pp. 635-645, Aug 1, 2021.
- [2] R. J. Gray *et al.*, "Intraoperative Margin Management in Breast-Conserving Surgery: A Systematic Review of the Literature," *Ann Surg Oncol*, vol. 25, no. 1, pp. 18-27, Jan, 2018.
- [3] R. Tang *et al.*, "Intraoperative micro-computed tomography (micro-CT): a novel method for determination of primary tumour dimensions in breast cancer specimens," *Br J Radiol*, vol. 89, no. 1058, pp. 20150581, 2016.
- [4] Y. Wang *et al.*, "Application of near-infrared fluorescence imaging in the accurate assessment of surgical margins during breast-conserving surgery," *World J Surg Oncol*, vol. 20, no. 1, pp. 357, Nov 9, 2022.
- [5] W. C. Zuniga *et al.*, "Raman Spectroscopy for Rapid Evaluation of Surgical Margins during Breast Cancer Lumpectomy," *Sci Rep*, vol. 9, no. 1, pp. 14639, Oct 10, 2019.
- [6] A. M. Zysk *et al.*, "Intraoperative Assessment of Final Margins with a Handheld Optical Imaging Probe During Breast-Conserving Surgery May Reduce the Reoperation Rate: Results of a Multicenter Study," *Ann Surg Oncol*, vol. 22, no. 10, pp. 3356-62, Oct, 2015.
- [7] M. Jin *et al.*, "Intraoperative Specimen Mammography for Margin Assessment in Breast-Conserving Surgery," *J Breast Cancer*, vol. 22, no. 4, pp. 635-640, Dec, 2019.
- [8] G. Havariyoun *et al.*, "A compact system for intraoperative specimen imaging based on edge illumination x-ray phase contrast," *Phys Med Biol*, vol. 64, no. 23, pp. 235005, Nov 26, 2019.
- [9] K. J. de Koning *et al.*, "Application and accuracy of ultrasound-guided resections of tongue cancer," *Oral Oncol*, vol. 133, pp. 106023, Oct, 2022.
- [10] J. M. Dixon *et al.*, "Intra-operative assessment of excised breast tumour margins using ClearEdge imaging device," vol. 42, no. 12, pp. 1834-1840, 2016.
- [11] E. R. St John *et al.*, "Rapid evaporative ionisation mass spectrometry of electrosurgical vapours for the identification of breast pathology: towards an intelligent knife for breast cancer surgery," *Breast Cancer Res*, vol. 19, no. 1, pp. 59, May 23, 2017.
- [12] J. Zhang *et al.*, "Nondestructive tissue analysis for ex vivo and in vivo cancer diagnosis using a handheld mass spectrometry system," vol. 9, no. 406, pp. eaan3968, 2017.
- [13] R. Nachabé *et al.*, "Diagnosis of breast cancer using diffuse optical spectroscopy from 500 to 1600 nm: comparison of classification methods," vol. 16, no. 8, pp. 087010-087010-12, 2011.
- [14] R. Nachabé, "Diagnosis with near infrared spectroscopy during minimally invasive procedures," Erasmus University Rotterdam, 2012.
- [15] L. L. de Boer *et al.*, "Fat/water ratios measured with diffuse reflectance spectroscopy to detect breast tumor boundaries," *Breast Cancer Res Treat*, vol. 152, no. 3, pp. 509-18, Aug, 2015.
- [16] J. W. Spliethoff *et al.*, "In vivo characterization of colorectal metastases in human liver using diffuse reflectance spectroscopy: toward guidance in oncological procedures," *J Biomed Opt*, vol. 21, no. 9, pp. 97004, Sep 1, 2016.

- [17] J. W. Spliethoff *et al.*, "Spectral sensing for tissue diagnosis during lung biopsy procedures: The importance of an adequate internal reference and real-time feedback," vol. 98, pp. 62-68, 2016.
- [18] M. S. Nogueira *et al.*, "Evaluation of wavelength ranges and tissue depth probed by diffuse reflectance spectroscopy for colorectal cancer detection," vol. 11, no. 1, pp. 798, 2021.
- [19] G. Einstein *et al.*, "Diffuse reflectance spectroscopy for monitoring physiological and morphological changes in oral cancer," vol. 127, no. 3, pp. 1479-1485, 2016.
- [20] A. Garcia-Uribe *et al.*, "In vivo diagnosis of melanoma and nonmelanoma skin cancer using oblique incidence diffuse reflectance spectrometry," vol. 72, no. 11, pp. 2738-2745, 2012.
- [21] V. G. Prabitha *et al.*, "Detection of cervical lesions by multivariate analysis of diffuse reflectance spectra: a clinical study," vol. 31, pp. 67-75, 2016.
- [22] S. A. Amiri *et al.*, "Electrosurgical knife equipped with diffused reflectance spectroscopy sensing for tumor margin detection during breast conserving surgery: a phantom study," in Advanced Biomedical and Clinical Diagnostic and Surgical Guidance Systems XIX, Year, pp. 49-57.
- [23] S. A. Amiri *et al.*, "Intraoperative tumor margin assessment using diffuse reflectance spectroscopy: the effect of electrosurgery on tissue discrimination using ex vivo animal tissue models," *Biomedical optics express*, vol. 11, no. 5, pp. 2402-2415, 2020.
- [24] S. A. Amiri *et al.*, "Enhancing Intraoperative Tissue Identification: Investigating a Smart Electrosurgical Knife's Functionality During Electrosurgery," *IEEE Transactions on Biomedical Engineering*, 2024.
- [25] G. C. Langhout *et al.*, "Nerve detection during surgery: optical spectroscopy for peripheral nerve localization," *Lasers in medical science*, vol. 33, pp. 619-625, 2018.
- [26] S. A. Amiri *et al.*, "Tissue-mimicking phantom materials with tunable optical properties suitable for assessment of diffuse reflectance spectroscopy during electrosurgery," *Biomed Opt Express*, vol. 13, no. 5, pp. 2616-2643, May 1, 2022.
- [27] S. A. Amiri *et al.*, "Intraoperative tumor margin assessment using diffuse reflectance spectroscopy: the effect of electrosurgery on tissue discrimination using ex vivo animal tissue models," *Biomed Opt Express*, vol. 11, no. 5, pp. 2402-2415, May 1, 2020.
- [28] T. M. Bydlon *et al.*, "Chromophore based analyses of steady-state diffuse reflectance spectroscopy: current status and perspectives for clinical adoption," *Journal of biophotonics*, vol. 8, no. 1-2, pp. 9-24, 2015.
- [29] H. Arimoto *et al.*, "Depth profile of diffuse reflectance near-infrared spectroscopy for measurement of water content in skin," vol. 11, no. 1, pp. 27-35, 2005.
- [30] R. Hennessy *et al.*, "Effect of probe geometry and optical properties on the sampling depth for diffuse reflectance spectroscopy," *J Biomed Opt*, vol. 19, no. 10, pp. 107002, 2014.
- [31] C. Kunos *et al.*, "Breast Conservation Surgery Achieving  $\geq$  2 mm Tumor-Free Margins Results in Decreased Local-Regional Recurrence Rates," vol. 12, no. 1, pp. 28-36, 2006.
- [32] N. Houssami *et al.*, "The association of surgical margins and local recurrence in women with early-stage invasive breast cancer treated with breast-conserving therapy: a meta-analysis," *Ann Surg Oncol*, vol. 21, no. 3, pp. 717-30, Mar, 2014.

# 6

## **Multi-wavelength probe for fat content detection: Toward LED-based real-time tissue diagnosis**

Diffuse reflectance spectroscopy (DRS) has been widely employed in medical diagnosis, involving the study of tissue response to broadband light. This study investigates the feasibility of simplifying the DRS console and its application in tissue detection by analyzing the response of tissue-mimicking materials to specific wavelengths. Specifically, the study focuses on detecting the chromophores of interest, namely fat and water. Various phantom materials with different fat and water content were developed for experimentation. A prototype probe comprising an electronic board, LEDs, and a photodetector was designed to measure these phantom materials. Additionally, DRS was utilized to confirm the fat percentage of these phantoms. The results demonstrate a significant correlation between the fat percentage of the phantoms and the detected intensity of LEDs at 1300 nm and 970 nm when scaled to the intensity at 1200 nm, in the transmission mode. This finding suggests that, depending on the chromophore of interest and appropriate wavelength selection, the content of the chromophore and the tissue type could be estimated using this prototype, showcasing its potential for future incorporation into diagnostic applications.

## 6.1 Introduction

As optical technologies, including advancements in fiber optics, optoelectronics, and optical microelectromechanical systems, continually progress, the miniaturization of optical-imaging platforms opens avenues for widespread application not only in point-of-care settings but also in operating rooms and diverse clinical environments. The development of compact optical devices allows for enhanced versatility, enabling their integration into various medical settings to support precise diagnostics and real-time imaging during surgeries or other clinical procedures [1-4].

Miniaturization holds the potential to streamline and simplify diffuse reflectance spectroscopy (DRS) techniques. These methods involve emitting a wideband light onto the tissue and collecting the reflected light, using the light diffusion theory to discern both the chemical components and the type of tissue [5].

Miniaturizing the technique becomes feasible when tissue diagnosis relies on information derived from a few specific wavelengths. This implies that, depending on the tissue type, the optical response within specific wavelengths or a defined range showcases unique characteristics, enabling differentiation from other wavelengths. Furthermore, simplification is enhanced when the miniaturized device is applied to detect a specific component, characterized by a distinct absorption or scattering profile in a specific wavelength [6].

There have been ongoing efforts to miniaturize and simplify optical techniques. The diversity of applications is notable, ranging from wearable probes for breast and cerebral hemodynamic monitoring [7-9] to devices for glucose detection [10], neonatal jaundice detection [11], and even tumor detection in kidneys and gastrointestinal cancer [12, 13]. These applications show the versatility of miniaturized optical devices in monitoring blood-derived parameters, bilirubin concentration, tissue chromophores, and more, reflecting the broad scope of optical technology applications in healthcare and diagnostics.

Given the primary objective of this thesis, which is the development of a smart electrosurgical tool for real-time margin assessment during breast cancer surgery, the pursuit of a miniaturized tissue detection device aligns seamlessly with the main goal. Introducing a miniaturized version of the DRS setting, capable of tissue detection through measurements on a selection of wavelengths, would enhance the feasibility of integrating this device into the surgical instrument, further optimizing its application.

In the present research, the primary objective was to establish a device utilizing LEDs to emit light at specific wavelengths and a single photodetector to capture the light from the material of interest. The research emphasis is on the real-time detection of breast cancerous tissue, with a specific focus on the chromophores of interest being fat and water. These chromophores play a crucial role in differentiating malignant tissue from benign tissue in the breast using DRS [14].

The selection of wavelengths was initially guided by existing literature and later refined based on the outcomes of experiments conducted by R. Breda using the same device on phantom materials [15]. Subsequently, the research delved into exploring the potential of the device for estimating the fat content of tissue-mimicking materials.

## 6.2 Materials and Methods

### 6.2.1 Device design

The device design process involved the design of the electronic board and the selection of suitable optical components for its primary application, which focused on detecting the fat content of tissue-mimicking materials in transmission mode. The subsequent subsections provide detailed descriptions of these processes.

#### 6.2.1.1 Electronics

Controlled by a Teensy 3.6 microcontroller (PJRC, USA)—the core of the circuit—programmed via the open-source Arduino software (Arduino IDE 1.8.19, Arduino, Italy), the prototype board is divided into two main functional modules: the light source driver and the signal acquisition module. The light source drive module is utilized for the independent control and power supply of two light sources. Meanwhile, the signal acquisition module is responsible for managing the timing and control of a photodetector, as well as processing the sensor signal for recording and transmission to a computer through the microcontroller. Figure 6.1(A) illustrates the general block diagram of the device.

Two autonomous voltage-controlled current sources are integrated within the light source drive module, generating distinct constant current levels to power the light sources. The circuit configuration of one such current source is shown in Figure 6.1(B). For both sources, the Teensy's 5 V output voltage undergoes conversion into the targeted current level, facilitated by a general-purpose operational amplifier (TLV2372, Texas

Instruments, USA) and an N-channel enhancement MOSFET (NDT451AN, Onsemi, USA). Subsequently, the signal is transmitted to the light source via a coaxial cable. The amplifier's input voltage is determined by a voltage divider (R1, R2), while the current level is established by a source resistor, named Rsource. Additionally, a second MOSFET, positioned in series with Rsource, functions as a light switch, the activation of which is controlled programmatically through a Teensy digital output pin.

The signal acquisition module (Figure 6.1(B)) consists primarily of an InGaAs photodiode (FGA01, Thorlabs, USA), linked to the board through a coaxial cable, and a precision switch integrator transimpedance amplifier (IVC102, Burr-Brown, USA). The photodiode generates a current corresponding to the detected light, which is then converted into voltage and amplified by the transimpedance amplifier (TIA). Following inversion by a unity-gain inverting amplifier (TL071CP, Texas Instruments, USA) for obtaining a positive signal, the Teensy reads the signal after a voltage-limiting step, providing input pin protection, and converts it into a digital signal via the integrated ADC. A DC/DC converter is utilized to power the TIA by stepping up the input voltage of the Teensy to obtain a 15 V power line. The entire circuit schematics are illustrated in Figure 6.1(B). The TIA integrates low-level input currents over a user-defined period, reducing noise and allowing for adaptable high gain levels. The TIA operates through a four-phase measurement cycle, resulting in a stable output voltage that can be measured to represent the effective output.

In the measurement cycle, the sensor becomes active during the integration period (Tint), determined by the TIA, which integrates low-level input currents for a user-defined period. The resulting output voltage is stored in an internal capacitor, contributing to noise reduction by averaging input noise from the sensor, amplifier, and external sources. Simultaneously, Tint allows for adjustable high gain levels via software. The measurement cycle comprises four phases controlled by digital signals from the Teensy, including a reset phase to reset the integrator, a pre-integration hold period to change the switch state, an integration period connecting the sensor to the amplifier, and a post-integration hold period yielding a stable output voltage. The Teensy ADC records this effective sensor output during the hold period, ultimately yielding a single voltage value at the conclusion of each cycle .

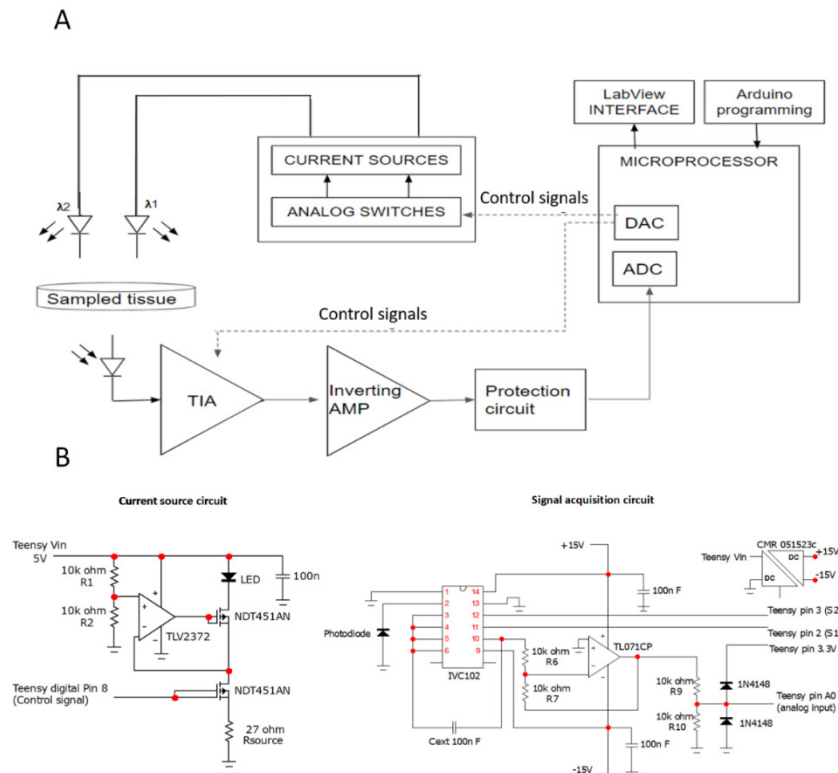


**Figure 6.1.** A) General block diagram of the device. B) Electronic design of the current source circuit and signal acquisition circuit

### 6.2.1.2 Wavelength selection

To accurately determine the fat content in tissues or tissue-mimicking materials, a broadband wavelength range proves effective [16, 17]. Tissues comprise various chromophores, each exhibiting a distinct absorption and scattering profile across different wavelengths. Notably, key absorbing chromophores in tissues, such as fat and water, primarily absorb in the visible light wavelength and Near-Infrared. Utilizing wavelengths within this range for fat or water content detection aligns logically with the prevalent absorbing elements in tissues, as illustrated by the absorption profile of water and fat shown in Figure 6.2, spanning from 900 nm to 1600 nm. Interestingly as shown in the figure, fat and water have very close absorption coefficient at two wavelengths close to 1200nm (1150.5 nm and 1251 nm) [5, 6]. Table 6.1 reports the main absorption peaks of fat and water within these wavelength bands.

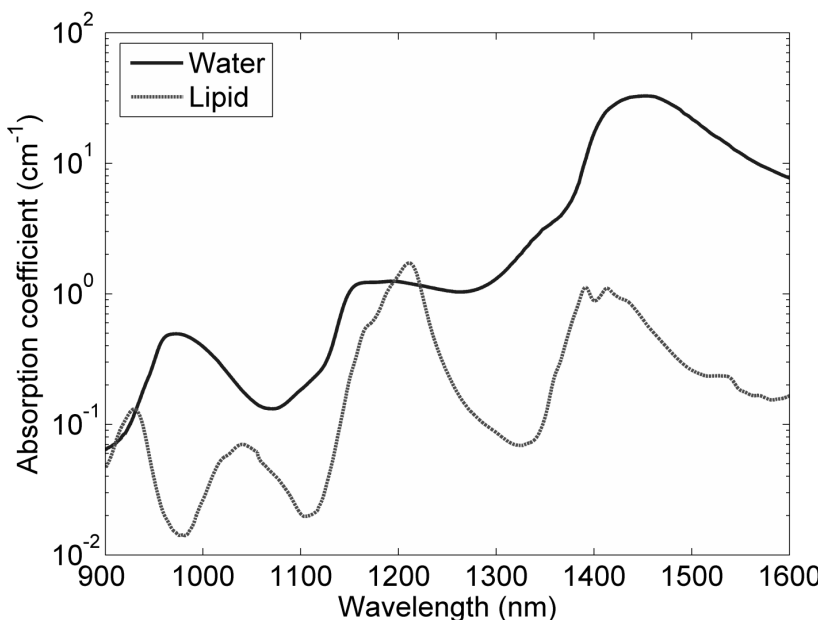


**Figure 6.2.** The absorption coefficient of fat and water [6]

**Table 6.1.** The main absorption peaks of fat and water [6].

Material	Wavelengths (nm)
Water	755, 972, 1192, 1453, 1932
Lipid	760, 930, 1042, 1211, 1393, 1414, 1720, 1760, 2142

One limitation regarding the wavelength selection was the availability of the LED with the specific wavelength. Since LEDs are characterized as incoherent light sources, their emission is dispersed over a spectrum of adjacent wavelengths, typically with a half-peak width spanning 20-50 nm. This range surpasses the majority of spectral absorption features. Consequently, LEDs producing output in proximity to the desired wavelengths were deemed satisfactory.

Considering the availability of LEDs in specific wavelengths and insights from literature and a primary study by R. Breda, the chosen wavelengths were 970 nm, 1200 nm, and 1300 nm [15]. The selection criteria include 1200 nm for its proximity to the isosbestic point of fat and water which can be used as reference point. Furthermore, 1300 nm was selected due to its proximity to a wavelength demonstrated in studies by de Boer [18] and Bogomolov [12, 19] to be useful in detecting tissue with varying fat content.

Additionally, 1300 nm is in a region with less densely "populated" characteristics, as highlighted by Bogomolov [12, 19], indicating its potential utility for scattering correction. The use of two wavelengths in the 1200-1300nm region is advantageous due to the nearly identical absorption coefficients of water in this area. This characteristic holds the potential for yielding meaningful results in the analysis. Additionally, 970 nm was chosen for its alignment with a water absorption peak, where fat exhibits significantly lower absorption.

### 6.2.2 Phantom production

To produce the tissue mimicking materials with varying fat and water content lard or pure porcine fat (BEEF&STEAK (<https://beefensteak.nl/>), Netherlands), distilled water, gelatin (250 Bloom, ES1477, Natural Spices, Netherlands), Transglutaminase (TG) (Unique Products Schuurman, Netherlands) and sodium benzoate (SB) (Natural Spices, Netherlands) were used. Table 6.2 specifies the role of each component and the respective quantities required to produce 100 ml of a phantom with a specific fat content (X%). The formulation was employed to create phantoms with fat contents of 20% (Phantom20), 30% (Phantom30), 40% (Phantom40), 50% (Phantom50), 60% (Phantom60), and 65% (Phantom65). The production of the phantom was as described in previous papers [16]. Initially, the blend of water and SB underwent heating in a beaker on a heater stirrer until the temperature reached 50 °C, depending on the desired fat content for the phantom. Subsequently, gelatin powder was gradually introduced into the mixture, and the entire liquid was heated further. Upon reaching a temperature of 90 °C, lard was incorporated into the mixture, and the beaker continued to be stirred for a few additional minutes. The TG was then added gradually. After a 10-minute interval, the contents of the beaker were poured into molds and placed in the freezer. After an hour, the molds were taken out of the freezer, and were placed in the fridge overnight.

Since the measurements were done with the LEDs and a photodetector in the transmission mode, it is crucial to acknowledge that the thickness of the phantom under consideration during the measurement process could substantially impact the recorded measurements. In order to ensure uniformity in phantom composition and maintain a consistent thickness of 2 mm, specialized molds were created using 3D printed supports and optically clear Precision Cover Glasses slides (170  $\mu\text{m} \pm 5 \mu\text{m}$ , Thorlabs). The inclusion of the 0.17 mm thick glass serves a dual purpose – enhancing the intensity of

the detected signal and providing protection to the phantoms against exposure to air and LEDs.

**Table 6.2.** The materials and their corresponding concentrations utilized in creating phantoms with different compositions of fat and water.

Material	Role	Amount for 100 ml PhantomX (X%)
Lard (ml)	To simulate the fat	X (ml)
Water (distilled) (ml)	To simulate the water	100-X (ml)
Gelatin (g)	Gelling agent and fat-water emulsifier	15% of water volume
Transglutaminase (g)	Cross linker of gelatin to increase the thermal stability	10% of Gelatin weight
Sodium Benzoate (g)	Preservative agent	0.1% of water volume

### 6.2.3 DRS measurement

To verify the fat content of the produced phantoms, DRS measurements were performed on each of the tissue mimicking materials, before further measurement were taken using the device. The DRS device and the optical probe used in this research is vastly described and used in our previous research [20-22]. Briefly, the DRS setup integrates a measurement console, measurement processing software, and a custom-designed DRS needle probe. For DRS measurements, a Philips custom-designed console was utilized, equipped with a halogen broadband light source (Avantes, The Netherlands) and two spectrometers. These spectrometers covered the 900–1700nm (NIRQuest 512, Ocean Optics, United States) and 400–1000 nm (Maya2000 Pro, Ocean Optics, United States) spectral ranges. Optical fibers were connected to the light source and spectrometers, with the other ends inserted into the needle probe. Before measuring each phantom, the optical console underwent thorough calibration, following the process outlined in previous papers [20-22]. Calibration involved placing the needle probe at a fixed distance above a white reference standard (Spectralon, Labsphere Inc., United States) to ensure the optical fibers' distal ends were parallel to the standard's surface. The DRS system outputs were processed using Philips custom-developed software (MatLab-based), employing a nonlinear Levenberg–Marquardt inversion algorithm based on an analytical model by Farrell et al [23]. The software facilitated fitting a curve on the input spectrum, enabling the calculation of chromophore concentration from the fitted data. The processed spectra

provided outputs such as fat fraction (Fat/Fat+water) and total fat and water content (Fat+Water). Additional details on the DRS method and model can be found in previous works. This software and methodology have been applied in healthcare, as explored in various publications [5, 14, 22].

### 6.2.4 Experimental setup

For the experimental setup, the slides of the phantoms were used (Figure 6.3(A)). The sensor board was used to interconnect the photodetector and a single LED via coaxial cables, arranged in a transmission-based configuration. The photodetector was securely attached to a manual vertical microstage (Thorlabs, USA) through the assistance of a 3D printed support, while the LED was affixed to a motorized linear stage (Aerotech, USA) with the aid of a second 3D printed component, as depicted in Figure 6.3(B). In the context of transmission-based measurements, the distance between the LED and the detector significantly influences the sensor output. Consequently, the microstage played a crucial role at the experiment's outset, allowing the adjustment of the distance between the LED and the sensor. The use of glass slides as sample holders facilitated easy phantom replacement by sliding them between the LED and sensor, establishing the source-to-detector separation (SDS) at the test's commencement, which remained constant throughout the experiment (Figure 6.3(A)).

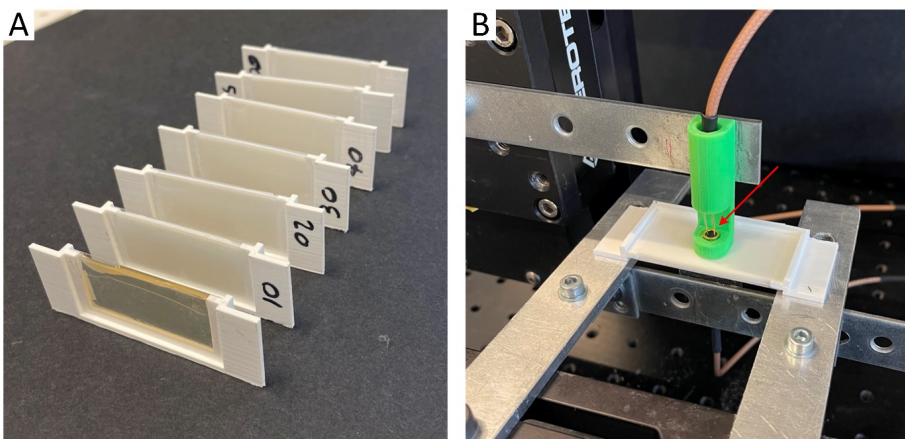


**Figure 6.3.** Illustration of the experimental setup for measuring the phantom materials using the prototype. A) Phantom material slides with varying fat content. B) The 3D-printed green part (one positioned on top and one below the slide) that holds the LED or photodetector (indicated by the red arrow), connected to the board via coaxial cable.

The sensor board, crucial for power and data acquisition, was connected to a computer via a USB cable. Signal recording was accomplished through a LabVIEW interface (LabVIEW 2018, National Instruments, USA). Integration times of 50 ms were configured for the reference measurement (measurement done with an unobstructed path between the light source and the sensor needed to calibrate the system), while 300 ms was applied to other measurements. Hold and reset periods of 100 ms were implemented to passively cool the LEDs, mitigating temperature drift. The phantom slides, extracted from the fridge two hours before measurements, were allowed to reach room temperature. For each measurement, LabView data acquisition was activated for ten seconds, generating approximately twenty samples. A standard procedure included four reference measurements for each LED, followed by four measurements for each phantom at different locations.

### 6.2.3 Data analysis

Matlab (MathWorks vR2021a, USA) was employed for data analysis, involving initial pre-processing steps. Raw data was visualized to identify unexpected values and outliers. Mean and standard deviation were calculated for each measurement, resulting in a total of 28 data points (4 measurements x (6 phantoms + 1 reference) for each wavelength). The mean and standard deviation were computed for each LED-phantom combination and applied across all replicates for descriptive analysis. To facilitate a comparison of responses at various wavelengths, the intensity (I) for each phantom-LED combination was normalized based on the mean reference of the LED. This normalization resulted in a normalized intensity ( $I_{\text{normalized}}$ ) within the 0-1 range, calculated using the formula:

$$I_{\text{normalized}, \lambda}^{\text{fat\%}} = \frac{I_{\lambda}^{\text{fat\%}}}{I_{\lambda}^{\text{ref}}}$$

To derive fat-intensity curves at 970 nm and 1300 nm, the acquired measurements underwent calibration against the reference signal and scaling at 1200 nm.

The scaled intensity ( $S_{\lambda}^{\text{fat\%}}$ ) for each phantom data was obtained by dividing all values by the reference wavelength value ( $I_{\text{normalized}, \lambda_{\text{ref}}}^{\text{fat\%}}$ ). To facilitate comparison, the scaled intensity value at the reference wavelength (= 1) was subtracted from the others. By undergoing this transformation, the scaled intensity now reflects the ratio between

intensities measured at two distinct wavelengths (measured wavelength (970 or 1300 nm) and reference wavelength (1200 nm)).

$$S_{normalized, \lambda}^{fat\%} = \frac{I_{normalized, \lambda}^{fat\%}}{I_{normalized, \lambda_{ref}}^{fat\%}} - S_{\lambda_{ref}}^{fat\%}$$

Subsequently, a least-square linear regression was conducted on the scaled intensity values to assess the linear relationship with lipid content.

## 6.3 Results

### 6.3.1 DRS measurement

The tissue-mimicking phantom materials with varying fat and water content were initially produced and measured using the DRS setup to validate the accurate fat concentration (Fat%). The estimated Fat% for each phantom is presented in Table 6.3. In the case of Phantom60 (phantom with 60% fat), the estimated Fat% is marginally lower than the anticipated amount, possibly resulting from an error in production, such as using a lesser amount of fat than intended. For the remaining phantoms, the estimated Fat% closely corresponds to the anticipated values, and the offsets are relatively small.

**Table 6.3.** The estimated mean fat concentration (Fat%)  $\pm$  the standard deviation of each phantom using the DRS in the Near-Infrared (NIR) bandwidth.

Expected Fat%	20	30	40	50	60	65
Estimated Fat%	18.7 $\pm$ 0.3	28.3 $\pm$ 1.0	39.9 $\pm$ 0.5	50.2 $\pm$ 0.5	56.1 $\pm$ 0.9	64.5 $\pm$ 0.4

### 6.3.2 Measurement using the device

The device prototype, manufactured according to the electronic circuit, is depicted in Figure 6.4. The figure shows both the device board and housing. The two coaxial cables extending from the device can be linked to the LEDs output and the photodetector input on the board, connecting on the other ends to the LEDs and photodiode, respectively. To power the board and facilitate data acquisition, the device was additionally connected to the computer through a USB cable.

Measuring the slides of the phantoms with the device was carried out in accordance with the procedures outlined in section 1.2.4 and depicted in Figure 6.3. The measurements of the phantoms were conducted using LEDs at 970 nm, 1300 nm, and 1200 nm. Figure 6.5 illustrates the measured intensity of each phantom at 970 nm and 1300 nm after scaling at 1200 nm.

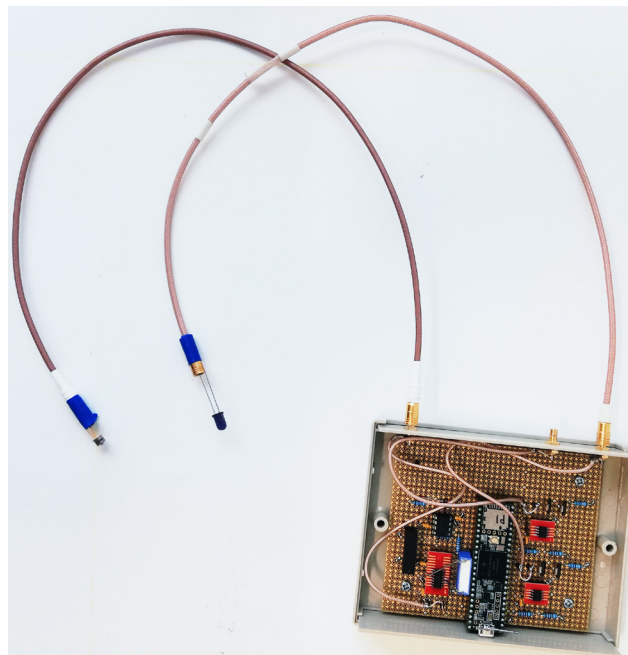


**Figure 6.4.** The electronics of the final prototype

In the context of regression analysis, the analysis depicted in Figure 6.5 reveals a distinct linear relationship between the fat content of the phantom and the scaled intensity at 1200 nm for both 970 nm and 1300 nm LEDs. The linear fitting curves, visually represented in pink, are characterized by the equations  $Y = 0.035X + 0.058$  ( $R^2 = 0.915$ ) for 970 nm and  $Y = 0.012X + 0.201$  ( $R^2 = 0.924$ ) for 1300 nm.

To assess the quality of the fit, the  $R^2$  values provide a measure of how well the linear models capture the variability in the data. The high  $R^2$  values for both LEDs (91.5% for 970 nm and 92.4% for 1300 nm) indicate strong correlations between fat content and scaled intensity, validating the reliability of the linear models.

In this research, initial steps have been taken toward simplifying a DRS console by utilizing a photodetector and a few LEDs. A device was developed to map the optical characteristics of phantom materials at a few specific wavelengths, rather than across a wide band of wavelengths. This can lead to a handheld probe that can be used for tissue identification, as opposed to a bulky setup, which could be utilized in various clinical settings, ranging from point-of-care settings to operating rooms.

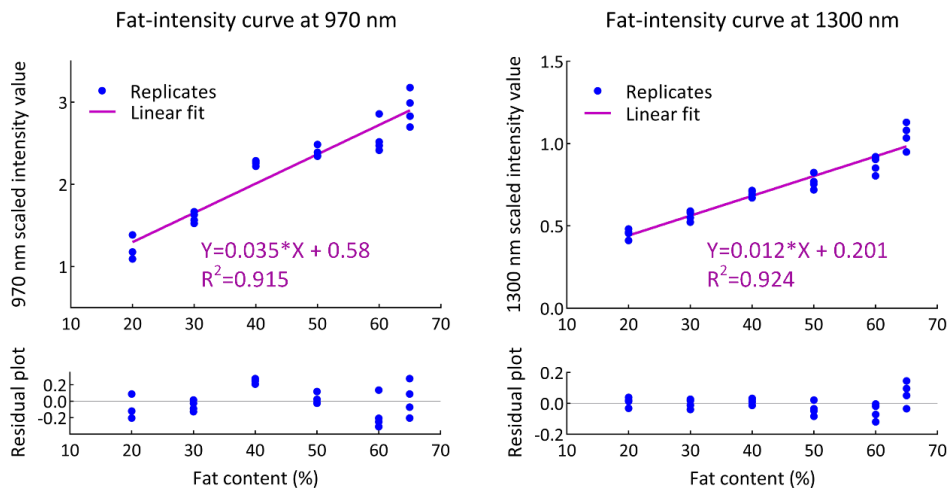


**Figure 6.5.** Scaled Intensities at 970 nm and 1300 nm for each phantom. Blue dots depict replicate measurements (4 repeated measurements per phantom), while the pink lines represent linear fitting models. The residual distribution around zero is displayed below each graph.

While DRS measurements can typically be conducted in reflectance mode, the developed setup in this study only allowed for measurement in transmission mode. Initial tests using LEDs in reflectance mode revealed that detecting a reflectance signal with the current LEDs was not feasible due to their low power output, suggesting that a transmission configuration might result in less light loss. Further investigation by R. Breda demonstrated that using laser diodes with high injection power could successfully measure a reliable signal from tissue-mimicking materials in reflectance configuration [15]. However, in the present research, the transmission mode was employed to demonstrate the concept, with the intention of utilizing reflectance mode with laser diodes in future studies, which is preferred for clinical applications.

One challenge associated with the transmission configuration is its sensitivity to sample thickness. Using slides of phantom materials helped maintain a consistent sensor-to-detector distance across all measurements.

A limitation concerning the use of either LEDs or laser diodes is their limited availability in all wavelengths. Therefore, the choice of wavelengths was constrained by both the wavelengths relevant to the chromophores of interest, namely fat and water in this study, and the wavelengths commercially available in the market.

In optical measurements, the interplay between transmission and scattering is pivotal in determining the intensity of light detected by a sensor. Increased scattering levels diminish the light reaching the sensor opposite the light source, resulting in an apparent decrease in detected intensity. This effect is particularly pronounced when analyzing the intensity gradient observed with rising fat content in samples, where scattering supersedes chromophore composition as the primary influencer of detected intensity. Conversely, the spectral data shape reflects the varying absorption and scattering properties of chromophores at different wavelengths within the light spectrum. By comparing values at distinct wavelengths, a more robust optical detection method can be established, facilitating a comprehensive analysis of spectral shapes. The primary experiment conducted by R. Breda suggested a potential correlation between specific wavelengths and the fat content of tissue-mimicking phantoms [15]. This correlation became apparent when the intensities were scaled to 1200 nm. The calculation of scaled intensity, achieved by comparing intensities at specific wavelengths to a reference wavelength, proves invaluable for spectral shape comparisons. While this method is commonly employed, it is essential to recognize that alternative transformations may also yield relevant results, underscoring the adaptability and potential for further enhancement in optical detection methodologies.

The result of this research showed that there is actually a linear relation between the scaled measurement at 970 nm or 1300 nm with the fat content of the phantoms. The robust R<sup>2</sup> values for both LEDs (91.5% for 970 nm and 92.4% for 1300 nm) signify strong correlations, affirming the predictive capacity of the linear regression models. Importantly, in assessing the residuals of both regression models, it was observed that they are evenly distributed around 0. This characteristic of residuals indicates a good fit, suggesting that the linear models effectively capture the variability in the data. The normality and symmetry of the residuals further underscore the reliability of the

---

regression analysis, supporting the models' ability to explain the relationship between fat content and scaled intensity at 1200 nm.

When it comes to the application of the device for detecting breast benign tissue from malignant tissue, it has been shown that each tissue has some distinct response to some of wavelengths so these wavelengths can be used to distinguish the tissues from each other. For instance, by comparing the DRS spectrum of the tumor and healthy breast tissue, De Boer et al, showed that at eight specific wavelengths, the response of these tissues is significantly different. Based on the result of this research and classification based on these wavelengths a predictive model was developed that could distinguish the breast malignant tissue from healthy tissue with high specificity and sensitivity. Remarkably, several of these wavelengths fall within the range associated with the absorption peaks of water or fat [18].

The 1200 nm wavelength plays a crucial role in estimating the fat-to-water ratio in optical measurements due to the presence of a significant lipid absorption peak at 1211 nm [6], as well as adjacent isosbestic points, underscoring the importance of this specific wavelength range. A study by Kho et al. showcased a method to gauge fat content in breast tissue by analyzing the slope around 1197 nm within a 10 nm span [24]. In scenarios where significant scattering is absent and water and fat are the primary absorbers in the optical spectrum, variations in measured signals predominantly signify changes in lipid content. Noteworthy is the scaled intensity gradient observed between 1300 nm and 1200 nm, alongside absorption characteristics at 970 nm, which reveal correlations between fat and water absorption peaks. Exploring isosbestic points, where water and fat exhibit identical absorption patterns, adds an additional layer of interest to the analysis. Kho et al. used the fat and water isosbestic points (931 nm and 1197 nm) to minimize variations in penetration depth and effectively distinguish between tumor and healthy breast tissue. The study focuses on the optical properties of breast tissue, emphasizing the higher water and lower fat content in tumors compared to healthy tissue, particularly in the NIR wavelength range [24].

Hendriks et al. also suggested comparable isosbestic points for fat and water. These points could be further employed to estimate the lipid-water ratio by determining scattering parameters at these specific points, where the absorption of fat and water remains constant regardless of their concentration [25].

More wavelengths have been reported by different research groups that could be valuable for detecting healthy and tumor tissue in the breast, as summarized in Table 6.4.

Following the primary objective of this thesis, which is to introduce a smart electrosurgical knife with real-time tissue recognition capabilities for intraoperative settings, the introduction of such a simplified device can significantly enhance the knife's usability for specific applications. As illustrated in the Figure 6.6, the developed simplified version of DRS using photodetectors and LEDs, along with its electronic circuit, can be seamlessly integrated into the design of a surgical knife.

**Table 6.4.** Summary of wavelengths identified in various studies, indicating their potential to discriminate between tumor and healthy breast tissue [15].

Reference	ref	Wavelengths (nm)
De Boer	[18]	501, 916, 973, 1145, 1211, 1371, 1424, 1597
Bogomolov	[19]	940, 1200, 1300, 1450
Lam	[26]	930, 976
Kamal e Pal	[27]	850, 940, 1050
Hendriks	[25]	1150.5, 1251, two wavelengths in the 1260-1400 range
Kho	[24]	910, 931, 1197, 1222, 1699, 1735

The electronic components in this design include the electronic board, LEDs with the desired wavelengths, and photodetectors connected to optical fibers, with their other ends embedded in the electrode tip of the electrosurgical knife. Furthermore, to align with surgeon preferences, the design can feature a DRS button so instead of continuous optical measurement, this button can be pressed whenever the surgeon intends to measure a specific location on the tissue.

Based on feedback gathered from surgeons in the previous study, it is evident that the simpler the application of the knife, the more practical it becomes in a surgical setting. For example, surgeons prefer straightforward feedback systems, such as sound or light indicators on the knife, to indicate tissue type (cancerous vs. benign) rather than relying on spectral responses or information displayed on a DRS console screen, such as Fat% or

tissue type. This functionality can be easily incorporated into the design of the smart electrosurgical knife using LED lights or speakers on the device to alert the user about the detection of specific tissue types or the distance of the knife tip from them.

Crucially, this design could operate independently of the need for a DRS console or connection to it with optical fibers, resulting in saving space in the operation room and eliminating the inconvenience of wires and cables that can impede the surgeon's movement and flexibility in different directions and spaces. This efficient approach enhances the usability and versatility of the smart electrosurgical knife, facilitating more efficient and targeted tissue recognition during surgical procedures.

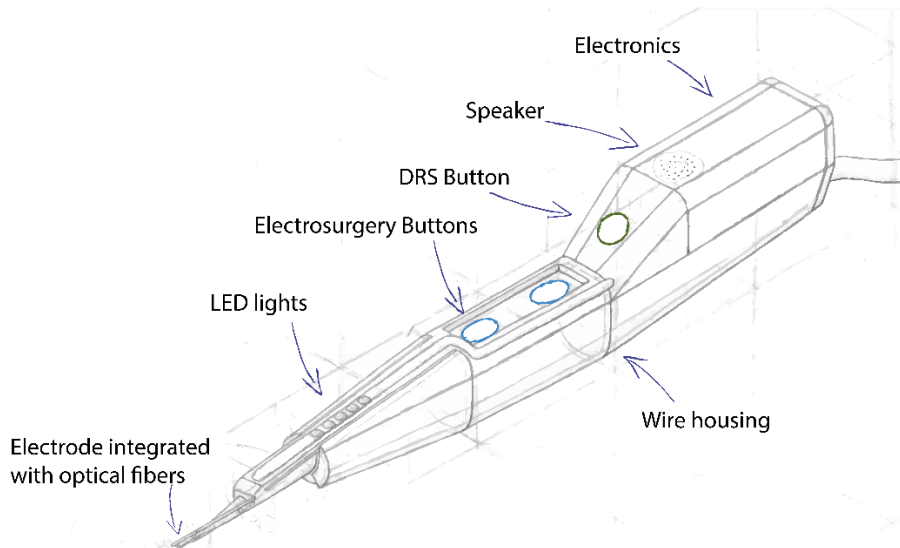


**Figure 6.6.** A design concept of a smart electrosurgical knife integrated with electronic components, including LEDs and photodetectors, that can be utilized as an alternative to the DRS console for real-time tissue detection during surgery. Illustrated by P.Callert [28].

While the initial findings provide promising insights in development of a LED-based probe for fat content detection, there are several factors that must be addressed before transitioning to clinical application. For instance, variations in LED performance and their impact on measurement accuracy need to be thoroughly understood and mitigated. Additionally, the complexity of real tissue composition introduces challenges that are not present in homogeneous phantom materials. These challenges include accurately detecting and distinguishing different tissue types within a sample, as well as accounting for variations in chromophore concentrations at tissue boundaries.

Addressing these issues will require extensive experimentation and refinement of the proposed prototype before it can be reliably deployed in clinical settings.

## 6.5 Conclusions

In conclusion, this study highlights the feasibility of simplifying diffuse reflectance spectroscopy for specific chromophore detection through the use of a photodetector and a few LEDs emitting at precise wavelengths in tissue phantoms. Particularly within fat and water-based phantoms, the scaled intensity of LEDs at 970 nm and 1300 nm, relative to the 1200 nm LED in transmission mode, displayed a significant correlation with the fat content of the phantoms. These findings suggest the promising potential of this method for identifying tissue types based on their fat content.

Further development and investigation are essential to expand the device's applicability for reflectance measurement and tissue analysis. Looking ahead, integrating the device into a probe or a smart electrosurgical knife could profoundly simplify the application of optics for real-time tissue detection across diverse clinical settings. This advancement indeed serves as a proof-of-concept step towards enhancing surgical precision through the utilization of bio-optics and the simplification of diffuse reflectance spectroscopy (DRS) application into an LED-based tissue diagnosis device.

## Bibliography

- [1] B. W. Pogue, "Perspective on the optics of medical imaging," *Journal of Biomedical Optics*, vol. 28, no. 12, pp. 121208-121208, 2023.
- [2] J. A. Kim *et al.*, "Optical spectroscopy for in vivo medical diagnosis—a review of the state of the art and future perspectives," *J Progress in Biomedical Engineering*, vol. 2, no. 4, pp. 042001, 2020.
- [3] M. Ochoa *et al.*, "Recent advances in biomedical photonic sensors: A focus on optical-fibre-based sensing," *Sensors*, vol. 21, no. 19, pp. 6469, 2021.
- [4] D. Lee *et al.*, "Next-generation imaging techniques: functional and miniaturized optical lenses based on metamaterials and metasurfaces," *Micromachines*, vol. 12, no. 10, pp. 1142, 2021.
- [5] R. Nachabé, "Diagnosis with near infrared spectroscopy during minimally invasive procedures," Erasmus University Rotterdam, 2012.
- [6] T. M. Bydlon *et al.*, "Chromophore based analyses of steady-state diffuse reflectance spectroscopy: current status and perspectives for clinical adoption," *Journal of biophotonics*, vol. 8, no. 1-2, pp. 9-24, 2015.
- [7] F. Teng *et al.*, "Wearable near-infrared optical probe for continuous monitoring during breast cancer neoadjuvant chemotherapy infusions," *Journal of Biomedical Optics*, vol. 22, no. 1, pp. 014001-014001, 2017.
- [8] S. S. Spink *et al.*, "High optode-density wearable diffuse optical probe for monitoring paced breathing hemodynamics in breast tissue," *Journal of Biomedical Optics*, vol. 26, no. 6, pp. 062708-062708, 2021.
- [9] A. Y. Rwei *et al.*, "A wireless, skin-interfaced biosensor for cerebral hemodynamic monitoring in pediatric care," *Proceedings of the national academy of sciences*, vol. 117, no. 50, pp. 31674-31684, 2020.
- [10] V. P. Rachim, and W.-Y. Chung, "Wearable-band type visible-near infrared optical biosensor for non-invasive blood glucose monitoring," *Sensors Actuators B: Chemical*, vol. 286, pp. 173-180, 2019.
- [11] C. Wu *et al.*, "Research and Design of Neonatal Jaundice Detector Based on Color Sensor," in 4th International Conference on Digital Medicine and Image Processing, Year, pp. 77-82.
- [12] A. Bogomolov *et al.*, "Development and testing of an LED-based near-infrared sensor for human kidney tumor diagnostics," *Sensors*, vol. 17, no. 8, pp. 1914, 2017.
- [13] S. Pimenta *et al.*, "Towards an on-chip optical microsystem for spectroscopic detection of gastrointestinal dysplasia," *Sensors Actuators B: Chemical*, vol. 281, pp. 751-756, 2019.
- [14] L. L. de Boer *et al.*, "Fat/water ratios measured with diffuse reflectance spectroscopy to detect breast tumor boundaries," *Breast Cancer Res Treat*, vol. 152, no. 3, pp. 509-18, Aug, 2015.
- [15] R. Breda, "Multi-wavelength probe for tumor margin detection during breast conserving surgery: A proof of concept study," Master Thesis, Mechanical, Maritime and Materials Engineering, Delft University of Technology, 2022; <http://resolver.tudelft.nl/uuid:0a828fa5-82eb-47a6-a0b5-ff0f9516c1cf>.

- [16] S. A. Amiri *et al.*, "Tissue-mimicking phantom materials with tunable optical properties suitable for assessment of diffuse reflectance spectroscopy during electrosurgery," *Biomed Opt Express*, vol. 13, no. 5, pp. 2616-2643, May 1, 2022.
- [17] R. Nachabé *et al.*, "Diagnosis of breast cancer using diffuse optical spectroscopy from 500 to 1600 nm: comparison of classification methods," *Journal of Biomedical Optics*, vol. 16, no. 8, pp. 087010-087010-12, 2011.
- [18] L. L. De Boer *et al.*, "Towards the use of diffuse reflectance spectroscopy for real-time in vivo detection of breast cancer during surgery," *Journal of translational medicine*, vol. 16, pp. 1-14, 2018.
- [19] A. Bogomolov *et al.*, "LED-based near infrared sensor for cancer diagnostics," in Optical Diagnostics and Sensing XVI: Toward Point-of-Care Diagnostics, Year, pp. 167-175.
- [20] S. A. Amiri *et al.*, "Electrosurgical knife equipped with diffused reflectance spectroscopy sensing for tumor margin detection during breast conserving surgery: a phantom study," in Advanced Biomedical and Clinical Diagnostic and Surgical Guidance Systems XIX, Year, pp. 49-57.
- [21] S. A. Amiri *et al.*, "Intraoperative tumor margin assessment using diffuse reflectance spectroscopy: the effect of electrosurgery on tissue discrimination using ex vivo animal tissue models," *Biomed Opt Express*, vol. 11, no. 5, pp. 2402-2415, May 1, 2020.
- [22] S. A. Amiri *et al.*, "Enhancing Intraoperative Tissue Identification: Investigating a Smart Electrosurgical Knife's Functionality During Electrosurgery," *IEEE Transactions on Biomedical Engineering*, 2024.
- [23] T. J. Farrell *et al.*, "A diffusion theory model of spatially resolved, steady-state diffuse reflectance for the noninvasive determination of tissue optical properties in vivo," *Medical physics*, vol. 19, no. 4, pp. 879-888, 1992.
- [24] E. Kho *et al.*, "Imaging depth variations in hyperspectral imaging: Development of a method to detect tumor up to the required tumor-free margin width," *Journal of biophotonics*, vol. 12, no. 11, pp. e201900086, 2019.
- [25] B. H. W. Hendriks *et al.*, "Determination of a lipid water ratio," Google Patents, 2016.
- [26] J. H. Lam *et al.*, "Narrowband diffuse reflectance spectroscopy in the 900–1000 nm wavelength region to quantify water and lipid content of turbid media," *Biomedical Optics Express*, vol. 12, no. 6, pp. 3091-3102, 2021.
- [27] A. M. Kamal *et al.*, "Towards the Development of an Intraoperative Probe for Breast Cancer Margin Assessment," in Optical Tomography and Spectroscopy, Year, pp. JM3A. 2.
- [28] P. Callaert, "Design of a Smart Electrosurgical Knife for Breast Conserving Surgery," TU Delft Mechanical, Maritime and Materials Engineering, Delft University of Technology, 2022; <http://resolver.tudelft.nl/uuid:d28699de-c693-4a0a-ad75-b9e2cd7ccb00>.

# 7

## Concluding remarks

## 7.1 Main findings of this thesis

In this thesis, we developed a smart electrosurgical knife integrated with a spectral sensing system (DRS) that provides real-time tissue feedback during surgery. The main aim was **to bring the smart electrosurgical knife as close to clinical use as possible**. The work explores the challenges of combining this optical system with the electrosurgical knife and assesses its applicability in clinical settings and realistic surgical scenarios. Here, we summarize the main findings pertaining to the research objectives of this thesis, as outlined in the Introduction chapter.

Main findings:

***Identify challenges - To identify challenges associated with integrating an electrosurgical knife with Diffuse Reflectance Spectroscopy (DRS)***

The integration of Diffuse Reflectance Spectroscopy (DRS) into a smart electrosurgical knife poses significant design challenges, particularly due to the necessity of placing the optical fibers in direct contact with the tissue during active measurement. This proximity is crucial for minimizing light loss and ensuring the full functionality of spectral measurements. However, our findings indicate that the thermal energy generated during even short electrosurgical sessions (e.g., 30 seconds) can damage unprotected optical fibers, leading to compromised optical measurements and tissue detection [1].

Furthermore, during electrosurgery, debris containing biological components from burned tissue can adhere to the optical fibers, compromising their effectiveness. Our findings confirm that this debris originates from the tissue being cauterized [1].

To address this, it is essential to protect the optical fibers not only from the high temperatures of up to 300°C generated during prolonged electrosurgery but also from the accumulation of this debris. This protection is crucial for maintaining the accuracy and reliability of optical measurements throughout the procedure [2, 3].

Design modifications intended to protect the optical fibers must withstand both thermal energy and debris attachment while ensuring that they do not significantly impact the accuracy of optical measurements or the functionality of the electrosurgical knife.

The protective housing or material must not significantly alter the light pathway or the tissue-light interaction, as this could lead to inaccurate optical readings. Our research

---

has shown that certain design changes can negatively impact optical measurements, either due to the properties of the protective material or the construction of the housing [3].

At the same time, from a clinician's perspective, any modifications to the blade electrode must have minimal impact on the knife's cutting and coagulating performance. Based on feedback from clinicians, to maintain precise, clean cuts and ensure usability, the design must avoid bulkiness, preserve sharp knife edges, and ensure that the overall structure remains compact and ergonomically acceptable for the user. Furthermore, it is essential that the blade retains its electrical conductivity to ensure optimal performance during surgery.

***Develop Test Platforms - To develop material formulation that can mimic breast tissue optics and conductivity for validating the smart electrosurgical knife***

One significant challenge in developing new medical devices is the absence of a platform that accurately simulates the real-world conditions in which the final product will be used. Such platform is required to test the prototype with the new ideas to determine the effectiveness of it during the development process.

The smart electrosurgical knife developed in this thesis was specifically designed for breast-conserving surgery. The female breast is a complex structure with multiple layers, each possessing unique optical and physical characteristics. Malignant growths further add to this complexity [4]. For the smart electrosurgical knife to be effective as an intraoperative margin detection tool, it must be capable of detecting these various layers, each with distinct optical properties, before actually reaching them.

To investigate and validate the smart electrosurgical knife, it is crucial to create a platform that accurately simulates the breast's layered structure, with each layer replicating the optical properties of the different tissue types. Additionally, the material used to construct this tissue phantom must be electrically conductive, allowing the electrosurgical knife to perform its function. The material also needs to withstand the thermal energy generated during electrosurgery without melting or degrading.

In this work, we have developed several innovative fat-water-based formulations for creating tissue phantoms, where the primary determinants of optical properties are the concentrations of fat and water. When compared to human tissue, the Diffuse Reflectance Spectroscopy (DRS) measurements from these developed tissue-mimicking materials

closely resemble the optical absorption and scattering profiles of the breast's different layers in the near-infrared wavelength range [5].

The selected materials also demonstrated the ability to endure electrosurgery, facilitating the assessment of various smart electrosurgical knife designs in further development stages. Each of these newly developed formulations has broad applicability, particularly in scenarios requiring the simulation of the optical properties of different breast tissue layers—adipose, fibroglandular, and malignant tissue—to validate diagnostic techniques based on tissue optical properties. Furthermore, the optical properties of these tissue-mimicking materials can be easily tuned by adjusting the fat and water content in the formulation, allowing for versatility based on the specific application.

Finally, we successfully constructed a breast phantom with a realistic appearance, incorporating different layers in their natural shapes along with tumor insertions. Importantly, the layers and boundaries are not visually distinguishable from each other, accurately simulating the clinical challenge of differentiating tissue types during surgery. This phantom can be utilized in future applications, such as validating the smart electrosurgical knife during simulated breast-conserving surgeries [5].

***Design and Develop - To design and validate a smart electrosurgical knife that addresses key challenges and assess its diagnostic ability in a complex phantom***

The primary requirements for making the smart electrosurgical knife functional include protecting the DRS optical fibers from thermal energy and debris attachment during electrosurgery. In this thesis, we achieved this by employing a combination of quartz tubes and PTFE heat-resistant tubes. The quartz tubes, with their closed, hemispherical ends, offer high transparency within the intended wavelength range and exceptional heat resistance, serving as a protective housing for the optical fibers against debris attachment and physical damage during the electrosurgery. Additionally, PTFE tubes, known for their low heat transmission, were used as insulators around the quartz tubes to shield the optical fibers from thermal energy during electrosurgery.

This design combination successfully protected the optical fibers during an interrupted electrosurgery session, even under exaggerated conditions exceeding those typically used in breast cancer surgery, for at least 14 minutes. Moreover, we demonstrated that this design does not significantly affect the diagnostic capabilities of

---

the DRS, as it effectively detected and distinguished between various tissue-mimicking materials as well as porcine adipose and muscle tissue [3].

After determining which design could ensure the functionality of the smart electrosurgical knife remains intact following prolonged use in electrosurgery, the design was employed to assess the knife's diagnostic capabilities in an *in situ* animal tissue model and a complex phantom.

Our findings demonstrated that the smart electrosurgical knife can detect changes in tissue composition and type while cutting through layered porcine tissue consisting of fat and muscle layers, with real-time measurements. Additionally, during electrosurgery on a phantom containing tissue-mimicking materials with varying fat percentages, we showed that the knife could identify changes in tissue layers before reaching the new layer. Real-time diffuse reflectance spectroscopy (DRS) measurements revealed that the knife can detect changes in tissue composition and type, indicating a boundary at least 4 mm ahead of the knife, where the new layer begins [3].

This ability highlights the smart electrosurgical knife's potential as an effective margin assessment tool. It can diagnose tissue boundaries, such as malignant growth, from 4 mm before contact, helping the surgeon achieve a negative margin with at least 2 mm of healthy tissue surrounding the tumor on the excised specimen. This feature enhances the surgeon's precision, allowing for greater freedom of movement. Furthermore, since the device can be used to examine both the wound cavity and the excised specimen post-removal, the surgeon can correct any margin positivity if an incorrect cut is made.

### ***Clinician Insights – To incorporate clinician feedback into the smart electrosurgical knife design***

To make the smart electrosurgical knife more functional for clinicians, particularly in terms of the blade design for electrosurgery, we incorporated feedback from clinicians, which indicated a preference for a smaller, less bulky blade with a sharper edge, resulting in a more favorable cutting experience. While it is desirable to keep the blade as thin and compact as possible to ensure precise and clean cuts, we also needed to consider the distance between the optical fibers, as this plays a crucial role in the accuracy of DRS measurements.

The distance between the fibers directly affects the amount and depth of tissue scanned. A larger fiber distance allows for the detection of tissue at greater depths, which can be advantageous during surgery by providing the surgeon with greater flexibility in movement and enabling the detection of negative margins. However, a larger distance also increases the risk of light loss within the tissue due to multiple scattering and absorption events, reducing the amount of light reaching the collecting fiber and potentially compromising diagnostic accuracy.

Therefore, a key design challenge was balancing fiber distance, ensuring accurate tissue recognition at sufficient depths, while maintaining a compact, sharp blade for effective electrosurgery. This balance was successfully achieved with the design presented as "Design 1" in Chapter 5.

***Performance Testing- Toward showcase the potential of the smart electrosurgical knife as an intraoperative margin assessment technique in a simulated lumpectomy procedure***

To evaluate the potential of the smart electrosurgical knife in a realistic surgical scenario, we engaged a surgeon to perform tumor extraction procedures on fat-water-based phantoms with tumor insertions. The tumors in this experiment contained a small amount of indocyanine green (ICG), detectable by diffuse reflectance spectroscopy (DRS) but invisible to the naked eye, as well as barium sulfate for contrast in X-ray imaging.

The surgeon used the smart electrosurgical knife with real-time DRS measurements on two phantoms, while on two additional phantoms, a standard electrosurgical knife was used without feedback, relying solely on preoperative X-ray images of the phantoms and tumor insertions. During the surgeries with the smart electrosurgical knife, we provided real-time feedback to the surgeon regarding the distance from the tumor insertion, based on the DRS measurements.

The results showed that both unguided surgeries resulted in positive margins, whereas the guided surgeries yielded better outcomes. In one guided surgery on phantom, a clear negative margin was achieved. In the second guided surgery, a small amount of tumor-mimicking tissue remained in the phantom cavity after extraction, likely due to either melting of the phantom tissue from the electrosurgery or a delay between the measurement and feedback. Nevertheless, the use of the smart electrosurgical knife significantly improved surgical outcomes compared to the unguided surgeries, particularly in detecting and completely removing the tumor in this phantom study.

---

While this experiment marks the first step toward validating the device as an intraoperative assessment tool in clinical setup, further investigation is required to fully demonstrate its capabilities.

### ***Simplify Design - To proof the concept of using a LED-based prob in place of a DRS console for tissue recognition***

It has been demonstrated that malignant and benign breast tissues can be distinguished by comparing the diffuse reflectance spectroscopy (DRS) outputs at specific wavelengths [6]. This method has also been proven effective for malignancy detection in other organs and tissues where differentiating between two types of tissue is required [7-11].

Building on this concept, we initiated the development of a handheld probe utilizing a few selected LEDs and a photodetector, as we targeted measurements at only a few specific wavelengths. This approach eliminates the need for a broadband light source and spectrometers, typically required to produce a full spectral response from tissue.

In this thesis, after developing a prototype with the necessary electronics, we identified the wavelengths capable of detecting changes in the fat content of the measurement substrate, which, in this case, was fat-water-based phantoms. We demonstrated that, with the appropriate wavelength selection in transmittance mode, the output can effectively differentiate between phantoms with varying fat content. Furthermore, we envisioned integrating this miniaturized optical probe into a smart electrosurgical knife, which would simplify the final product.

While we have made the first steps toward using LEDs and photodetectors for diagnostic purposes, further research is required to enhance the prototype and investigate its functionality in *ex vivo* or *in situ* conditions, where tissue composition is more complex.

## **7.2 Concluding remarks and future directions:**

### *On the application of DRS for cancer treatment*

In recent decades, the diagnostic applications of diffuse reflectance spectroscopy (DRS) have been extensively explored [6-11]. Its non-invasive nature, simplicity, affordability, and rapid output make DRS particularly advantageous for clinical use. As

DRS forms the diagnostic foundation of the smart electrosurgical knife, advancements in its application can directly enhance the knife's effectiveness.

In the context of breast cancer diagnosis, considerable effort has been dedicated to uncovering the potential of DRS in detecting tissue boundaries, especially in complex sites with heterogeneous tissue composition, such as ductal carcinoma in situ (DCIS), where malignancies are not easily visible.

Numerous machine learning models have been developed for tissue calcification detection, using parameters such as fitted data, estimated concentrations, and spectral responses—whether across a broad bandwidth or at selected wavelengths [12]. As machine learning and artificial intelligence continue to advance, we can anticipate the development of more sophisticated models, leading to more accurate tissue recognition.

Additionally, mechanical innovations, such as adjusting the number [13] or angulation of optical fibers [14], can further enhance the DRS's ability to distinguish between different tissue types.

### *On the design*

In our work, many design considerations for the smart electrosurgical knife were addressed and thoroughly discussed. In addition to the aspects already mentioned, other factors may also be applicable.

#### **Calibration Process**

Calibration of the smart electrosurgical knife, particularly the DRS system, is essential before each measurement session. This process is necessary to adjust system responses, compensate for ambient light, integrate the design, and correct the spectral output of the light source, as well as any wavelength-dependent sensitivity in the detector or optics.

How to seamlessly integrate the calibration process into the knife's design or its clinical workflow is a question for future research. For instance, a calibration cap could be designed to replace the standard blade cover provided in the original packaging. This cap could incorporate calibration materials, such as Spectralon (WS-1-SL, Labsphere Inc., USA), allowing the user to perform calibration effortlessly without any additional setup.

#### **Calibration Accuracy During Surgery**

A further issue to consider is whether the calibration remains accurate throughout surgery, as the tip of the device may become contaminated or damaged. If recalibration is

---

required during the procedure, the design must allow for this to be done as quickly and simply as possible. Future design considerations should explore how recalibration can be performed in a streamlined manner to avoid disrupting the surgery.

### **Durability and Cleaning**

Another design aspect, which was not a primary focus of this thesis but remains critical, is the device's robustness during cleaning, especially during surgery. As mentioned earlier, surgeons frequently clean the electrode of the electrosurgical knife to remove debris and maintain cutting efficiency. This cleaning process can involve wiping with gauze or scraping with sharp objects, which could easily damage the tip of the knife, the housing of the optical fibers, or the fibers themselves if the design is not sufficiently durable.

One potential solution is to adjust the sterilization and cleaning instructions so that surgeons adopt methods that will not damage the device. However, the preferred approach would be to improve the device's robustness to withstand harsher cleaning methods. While this may be challenging, especially since certain components, such as quartz tubes, must remain exposed for optimal performance, a combination of design improvements and adjusted cleaning procedures may be the most appropriate solution.

### **Sterilization**

Regarding sterilization, the current standard for electrosurgical knives is steam sterilization (autoclaving) at 134°C for 3-18 minutes, in accordance with ISO 17665 [15], NEN-EN 13060:2014 [16]. While most components of the smart electrosurgical knife, such as metallic parts and the quartz tube, can withstand this temperature for prolonged periods, the durability of other components—such as the optical fibers, PTFE tubes, and any adhesive materials used in manufacturing—remains uncertain.

Exploring whether these components can be replaced with more heat-resistant alternatives should be a focus for future development. Alternatively, the sterilization process itself could be adjusted for this prototype. For example, chemical or radiation sterilization methods could be validated as suitable alternatives for this design, reducing the risk of damage to sensitive components.

### **Sustainability Considerations**

As sustainability becomes a central topic in medical device innovation, it is essential to extend this consideration to the design of smart electrosurgical knives. Some key areas of focus include:

*Sustainable Materials:* The use of eco-friendly, recyclable, and biocompatible materials can significantly improve the environmental impact of the device. While materials like stainless steel and quartz tubes are already sustainable, exploring alternatives for other components can lead to more efficient recycling and waste reduction.

*Reusable Components:* Incorporating reusable components into the design, such as modular diagnostic units (sensors, cables, optical fibers), can significantly reduce medical waste. A modular design allows individual components to be replaced or upgraded without discarding the entire device, enhancing its sustainability. For instance, the smart electrosurgical knife can be designed so that the handheld part is reusable while the blade is disposable or recyclable.

*Energy Efficiency:* Manufacturers are continually working to improve the energy efficiency of electrosurgical units. This includes using more efficient power sources and optimizing energy consumption during procedures, contributing to a reduced environmental footprint.

*Modularity:* The knife's design can encourage repairability by allowing individual parts, such as blades, sensors, or electronic units, to be easily replaced. This reduces electronic waste and extends the device's life cycle.

*Minimizing Medical Waste:* The knife's diagnostic technology offers an opportunity to reduce medical waste by improving the precision of surgical cuts. This could lead to fewer secondary surgeries, less tissue damage, and reduced use of resources—thereby indirectly reducing the healthcare system's overall resource consumption.

### **End-of-Life Considerations**

End-of-life considerations are crucial for the sustainability of the smart electrosurgical knife:

*Recycling:* At the end of the device's life cycle, the materials should be recyclable or biodegradable to minimize landfill waste. Manufacturers could offer take-back programs or recycling options to ensure proper disposal of the device and its components.

---

*Disassembly for Recycling:* Designing the smart electrosurgical knife for easy disassembly ensures that different materials (metals, plastics, electronics) can be separated and recycled appropriately, further reducing the device's environmental impact.

### *On the clinical application*

**Feedback system:** Another critical challenge in designing the smart electrosurgical knife is the user interface. During the clinical investigation, we noticed that surgeons prefer to receive feedback in the quickest possible way. During surgery, the surgeon must move quickly to excise malignant tissue, requiring a feedback system that is both rapid and precise enough to serve as an effective real-time margin assessment tool. The final result could be either the distance of the knife from the tumor or the type of tissue in front of the knife. To achieve this, a safe margin needs to be set with the surgeon before surgery or a general safe margin should be agreed upon. Feedback can be communicated in simple and quick ways, such as an LED turning red or green when the safe margin is reached or passed, or through an auditory signal where the frequency indicates the proximity to malignancy.

Although using a monitor to communicate the result in detail can provide more comprehensive output to the surgeon, the quick pace of surgery to avoid time waste requires the simplest and fastest feedback system. However, a monitor can still be used to display additional information if needed. This could include the estimated main composition of the tissue, diagnostic results, tissue classification, and the estimated distance of the diagnosed tissue from the knife. In the future, if more design elements are incorporated, such as additional optical fibers, the monitor could provide even more detailed information for the operator.

**Safety:** The current design of the smart electrosurgical knife ensures functionality against thermal energy and debris attachment for up to 14 minutes of electrosurgery. However, several safety considerations have not been fully addressed in our current work. For example, one potential issue is related to hazardous byproducts. If the PTFE tubes or adhesive used in the design are exposed to high temperatures, they could release harmful substances. This raises a concern about whether such byproducts could pose risks to the patient or the surgical team. Another example is the risk of impact damage. If a surgical instrument accidentally strikes the quartz glass tubes within the knife, it could cause

damage to the device. This impact might affect the knife's functionality or even result in harm to the tissue being operated on.

Additionally, the cleaning process is an area of concern. For instance, if the cleaning procedures are too harsh, they could damage the smart electrosurgical knife. This damage might compromise the knife's performance and safety during surgery, potentially leading to complications.

Furthermore, if the device is used in an inappropriate setting, such as during prolonged surgeries beyond its recommended duration or at higher electrosurgery settings, the extent of potential damage needs to be evaluated, and solutions need to be investigated. Potential solutions could include incorporating automated features that switch off the device when the maximum application duration is reached or designing the device to detect damage and alert the user.

To address these concerns, further in-depth studies are needed. Additionally, clear and comprehensive instructions for use are essential to ensure the device is used safely and effectively during surgical procedures.

**Extended Application:** In the current work, we studied the use of the smart electrosurgical knife specifically for breast cancer treatment. However, the potential applications of the device extend beyond this context. The smart electrosurgical knife could prove useful in any surgery where DRS (Diffuse Reflectance Spectroscopy) is employed for tissue diagnosis and electrosurgical tools are used for surgery [7-11, 17].

Moreover, during surgeries, while surgeons aim to remove malignancies, they also strive to avoid inadvertent damage to critical structures such as blood vessels, nerves, or muscles [18]. In this regard, the smart electrosurgical knife could offer real-time tissue feedback, enhancing safety by helping surgeons avoid cutting too close to these critical structures, provided that DRS is validated for detecting such tissues.

### *Towards commercialization: current status and future outlook*

#### **Verification: Are we building the product right?**

In this thesis, the primary focus was on the verification of the smart electrosurgical knife to ensure that the device meets its design specifications and requirements. We began by identifying the main challenges involved in integrating diffuse reflectance spectroscopy (DRS) with the electrosurgical knife. Following this, we assessed compliance with the design specifications to verify that the smart electrosurgical knife adheres to the

---

criteria established during its development. This process involved confirming that the device's components, such as the DRS system, electrosurgical elements, and user interface, function as intended.

After the components were validated, the entire system was evaluated to ensure seamless integration, with tests conducted under controlled conditions. These tests assessed the device's reliability within specified parameters, including thermal tolerance and the ability to manage debris during extended use in *ex vivo* conditions (with animal tissue) and on phantoms (system integration and performance testing). Through this thorough verification process, we have verified that the smart electrosurgical knife is being built correctly in accordance with its design specifications, confirming that we are indeed building the product right.

### **Validation: Are we building the right product?**

Validation ensures that the smart electrosurgical knife meets its intended purpose in real-world clinical settings. It involves a thorough process of clinical trials, user feedback, safety and efficacy testing, long-term studies, and compliance with regulatory standards.

In this thesis, an initial step has been made toward the clinical trial phase to evaluate the performance of the smart electrosurgical knife in surgical settings, assessing its effectiveness under real-world conditions. These trials are essential to confirm that the device provides accurate feedback for tissue diagnosis and electrosurgery, ensuring it functions as expected during clinical use. Comprehensive feedback from surgeons using the device is critical, as their insights help determine whether the knife is intuitive, practical, and suitable for the demands of various surgical procedures.

The validation process must also confirm that the device is safe for patients and effective in delivering the intended clinical outcomes. This includes evaluating whether the knife accurately identifies tissue types, provides reliable real-time feedback, and minimizes the risk of adverse effects or complications during surgery. By ensuring the device performs effectively in real-world clinical settings, we can confidently determine whether we are building the right product. As the device progresses, validation becomes increasingly important, especially as it moves through the **Technology Readiness Levels (TRLs)**.

#### ***TRL 1-3: Ideation, Early Development, and Proof of Concept***

*Ideation (TRL 1):* At this stage, scientific research begins. For the smart electrosurgical knife, this involved early-stage research into integrating diffuse reflectance spectroscopy (DRS) with electrosurgical techniques. This research had already commenced when the overall project was initiated. Prior to the work presented in this thesis, MSc student F. Mollerus investigated the application of the electrosurgical knife in breast cancer surgery, identifying challenges and issues related to its use, with an eye toward combining DRS with the electrosurgical knife [19]. Additionally, MSc students from TU Delft, M.W. Adank, conducted research on the effects of electrosurgery on tissue and how it alters optical properties, aiming to determine whether DRS could accurately detect affected tissue [20].

*Early Development (TRL 2):* At this stage, initial concepts and feasibility studies were conducted. We explored how the DRS system could be integrated into a surgical knife, identifying both the potential benefits and challenges. Chapter 2 of this thesis represents the first attempt to integrate DRS into the electrosurgical knife, highlighting the challenges encountered during the development of the smart electrosurgical knife.

*Proof of Concept (TRL 3):* At the proof-of-concept stage, testing is conducted to demonstrate that the idea works in practical scenarios. For the smart electrosurgical knife, this involved bench testing and developing initial prototypes, which showed promising results in realistic conditions. Chapter 4 discusses the testing of the best design on ex vivo animal tissue and phantom models, while Chapter 5 presents the investigation of the device's clinical application in collaboration with clinicians.

At present, the device has successfully passed TRL 1 and TRL 2, and the findings from this research can serve as a proof of concept, indicating that the device is ready for further investigation toward clinical application. Thus, it can be confidently stated that TRL 3 has also been reached. Advancing through the next TRL levels will be the focus of future work, with the recommended progression outlined as follows:

#### ***TRL 4-6: Preclinical Validation***

*Lab Testing of Prototype (TRL 4):* Early prototypes of the smart electrosurgical knife can be created and tested in a controlled lab environment. This includes testing each component, such as the DRS and electrosurgical elements, to ensure proper functionality. GLP (Good Laboratory Practice) in vivo studies might begin here. Before clinical trials on humans, GLP-compliant preclinical studies can be conducted on animal models to test the safety and efficacy of the smart electrosurgical knife. In this thesis, initial steps toward

---

preclinical studies were taken in Chapters 4 and 5; however, further rigorous experimentation is required to ensure that the desired level of validation is achieved.

*System Validation in Lab (TRL 5):* The entire system is integrated, and testing continues in a simulated environment. This involves further preclinical testing on animal models (ex vivo or in vivo) to confirm safety and efficacy. GMP (Good Manufacturing Practice) manufacturing may also be initiated to ensure the device is being produced under controlled conditions. GMP ensures the product is consistent and reliable as it moves through the development stages and into clinical testing and commercialization. In this step the developers often begin detailed regulatory planning, including classification determination, to align the device with the correct regulatory pathway. A smart electrosurgical knife, which combines electrical and optical technologies, would likely fall under Class II or III, depending on its intended use and complexity.

#### ***TRL 6-8: Clinical Trials and Regulatory Approval***

*Pilot Clinical Studies (TRL 6):* The device can be tested in a pilot clinical study with a small group of human subjects to evaluate early safety, effectiveness, and usability in a controlled clinical setting. This can be done on patient going through either lumpectomy or mastectomy. If successful, the device moves to more comprehensive trials.

*Clinical Trials and System Prototype (TRL 7):* At this level, the smart electrosurgical knife would undergo a pivotal clinical study involving a larger group of patients to gather comprehensive data on its safety, effectiveness, and performance. This is a critical stage for preparing data to support regulatory submissions (e.g., FDA 510(k), PMA, or CE Marking). GMP manufacturing ensures that prototypes used in these trials are produced under regulatory-compliant conditions.

*Regulatory Dossier Preparation and Submission (TRL 8):* With successful results from clinical trials, the company compiles a technical dossier that is submitted to regulatory bodies such as the FDA or European authorities for review. This dossier will include all preclinical and clinical data, as well as risk analysis and manufacturing processes, to obtain necessary regulatory approvals. At TRL 8, the device is nearing commercialization, having undergone successful clinical trials and regulatory approval processes. This stage involves preparing for market entry by conducting market research, segmentation, and developing sales strategies. The market for the smart electrosurgical knife includes hospitals, clinics, and outpatient surgery centers that perform a wide range of surgical procedures. The target audience will primarily consist of:

- *Surgeons and medical professionals* who need enhanced precision in surgeries.
- *Hospital administrators* seeking cost-effective tools to improve patient outcomes.

Additionally, conducting market research on competitors (iKnife [21], MarginProbe [22], ClearEdge [23], UV-PAM [24], MUSE [25], MasSpec Pen [26], etc.) and identifying the unique selling points of the smart electrosurgical knife (e.g., advanced features like DRS integration) will help in positioning the product. For instance, the advantage of the smart electrosurgical knife lies in its ability to provide real-time tissue characterization. The data is gathered and analyzed almost instantaneously, often within a second. Moreover, since the light travels through the tissue, it allows for the collection of information from beneath the surface before cutting, enabling the surgeon to make an informed decision and limit the possibility of positive margins from the beginning. These are key advantages of the device over most intraoperative techniques, which typically involve chemical analysis, such as the MasSpec Pen (using ambient ionization mass spectrometry and a small water droplet to extract molecules from tissue surfaces) [26], or analysis of cutting byproducts, such as the iKnife (which analyzes the smoke produced during tissue cutting) [21]. These methods are not only more time-consuming and costly but also occur after the tissue has been cut, making them useful for correcting margins rather than predicting them. On the other hand, techniques like ClearEdge (based on bioimpedance) [23], MarginProbe (based on radiofrequency spectroscopy) [22], UV-PAM (Ultraviolet Photoacoustic Microscopy) [24], and MUSE (Microscopy with Ultraviolet Surface Excitation) [25] have proven effective in assessing tissue margins. However, compared to the smart electrosurgical knife, which aids surgeons in predicting and achieving negative margins, these techniques are generally limited to evaluating the tissue surface and are primarily used to examine excised specimens, focusing on correcting margins and facilitating re-excision.

*Product Launch and Commercial Use (TRL 9):* At this stage, the smart electrosurgical knife is fully approved for commercial use and is launched into the market. Post-market surveillance ensures continued safety and effectiveness as the device is used in real-world surgical settings. Training programs for healthcare providers and a robust distribution strategy are essential at this level.

### 7.3 Final words

In conclusion, the work presented in this thesis represents our efforts to develop a medical device that can assist surgeons in detecting cancerous tissue in real-time during surgery, with the hope of easing both the surgical procedure and the lives of patients. One lesson that has continually emerged throughout this project is that the successful creation of a medical device relies on the close collaboration between engineers and clinicians. It is only through the shared knowledge and expertise of countless individuals over centuries that we may one day find a transformative solution in our fight against cancer.

As Siddhartha Mukherjee, author of *The Emperor of All Maladies: A Biography of Cancer* [27], states:

"The oldest and simplest emotion known to mankind is fear, and the oldest and simplest kind of fear is fear of the unknown. But the conquest of cancer is not limited by fear, but by knowledge."

He further reminds us:

"To keep pace with cancer, you have to have the science constantly moving forward, and that's what gives us hope — the idea that science is not static but ever evolving in our fight against this disease."

Reflecting back on the opening of this thesis, I hope that one day, as a society, we will reach a point where the news of a cancer diagnosis will no longer be met with shock, disbelief, and the shattering of lives, as it was with Nil. Instead, it will be regarded as a manageable illness, one that can be easily cured.

## Bibliography

- [1] S. A. Amiri *et al.*, "Intraoperative tumor margin assessment using diffuse reflectance spectroscopy: the effect of electrosurgery on tissue discrimination using ex vivo animal tissue models," *Biomed Opt Express*, vol. 11, no. 5, pp. 2402-2415, May 1, 2020.
- [2] S. A. Amiri *et al.*, "Electrosurgical knife equipped with diffused reflectance spectroscopy sensing for tumor margin detection during breast conserving surgery: a phantom study," in Advanced Biomedical and Clinical Diagnostic and Surgical Guidance Systems XIX, Year, pp. 49-57.
- [3] S. A. Amiri *et al.*, "Enhancing Intraoperative Tissue Identification: Investigating a Smart Electrosurgical Knife's Functionality During Electrosurgery," *IEEE Transactions on Biomedical Engineering*, 2024.
- [4] R. Nachabé *et al.*, "Diagnosis of breast cancer using diffuse optical spectroscopy from 500 to 1600 nm: comparison of classification methods," *Journal of Biomedical Optics*, vol. 16, no. 8, pp. 087010-087010-12, 2011.
- [5] S. A. Amiri *et al.*, "Tissue-mimicking phantom materials with tunable optical properties suitable for assessment of diffuse reflectance spectroscopy during electrosurgery," *Biomed Opt Express*, vol. 13, no. 5, pp. 2616-2643, May 1, 2022.
- [6] L. L. De Boer *et al.*, "Towards the use of diffuse reflectance spectroscopy for real-time in vivo detection of breast cancer during surgery," *Journal of translational medicine*, vol. 16, pp. 1-14, 2018.
- [7] G. Einstein *et al.*, "Diffuse reflectance spectroscopy for monitoring physiological and morphological changes in oral cancer," vol. 127, no. 3, pp. 1479-1485, 2016.
- [8] A. Keller *et al.*, "Diffuse reflectance spectroscopy of human liver tumor specimens—towards a tissue differentiating optical biopsy needle using light emitting diodes," vol. 9, no. 3, pp. 1069-1081, 2018.
- [9] V. G. Prabitha *et al.*, "Detection of cervical lesions by multivariate analysis of diffuse reflectance spectra: a clinical study," vol. 31, pp. 67-75, 2016.
- [10] J. W. Spliethoff *et al.*, "Spectral sensing for tissue diagnosis during lung biopsy procedures: The importance of an adequate internal reference and real-time feedback," vol. 98, pp. 62-68, 2016.
- [11] J. W. Spliethoff *et al.*, "In vivo characterization of colorectal metastases in human liver using diffuse reflectance spectroscopy: toward guidance in oncological procedures," vol. 21, no. 9, pp. 097004-097004, 2016.
- [12] L. L. de Boer, "Detecting breast cancer tissue with diffuse reflectance spectroscopy," 2019.
- [13] D. Veluponnar *et al.*, "Diffuse reflectance spectroscopy for accurate margin assessment in breast-conserving surgeries: importance of an optimal number of fibers," vol. 14, no. 8, pp. 4017-4036, 2023.
- [14] M. S. Losch *et al.*, "Diffuse reflectance spectroscopy of the spine: improved breach detection with angulated fibers," vol. 14, no. 2, pp. 739-750, 2023.
- [15] T. I. O. f. Standardization, "ISO 17665:2024, Sterilization of health care products — Moist heat — Requirements for the development, validation and routine control of a sterilization process for medical devices," The International Organization for Standardization, 2024.
- [16] E. C. f. Standardization, "NEN-EN 13060:2014 en-Small steam sterilizers," 2014.

---

- [17] Y. Zhang *et al.*, “Diffuse reflectance spectroscopy as a potential method for nonmelanoma skin cancer margin assessment,” vol. 2, no. 3, pp. e202000001, 2020.
- [18] R. Mastronicola *et al.*, “Current approaches to salvage surgery for head and neck cancer: a comprehensive review,” vol. 15, no. 9, pp. 2625, 2023.
- [19] F. Mollerus, “The integration of diffuse reflectance spectroscopy into the electrosurgical knife used during breast-conserving surgery: Determining and overcoming the challenge of tissue debris adhering to the ‘smart’electrosurgical knife,” Master thesis, Mechanical Engineering, Delft University of Technology (TU Delft), 2018; <https://resolver.tudelft.nl/uuid:fd6cb68a-921c-4f6d-9df0-0710b4bfdb8f>.
- [20] M. Adank, “Evaluation of a smart electrosurgical knife: assessing the feasibility of tumour detection with Diffuse Reflectance Spectroscopy in breast conserving surgery,” Master thesis, Mechanical Engineering, Delft University of Technology (TU Delft), 2017; <https://resolver.tudelft.nl/uuid:8576284f-542a-401f-b62b-8d317e9af28e>.
- [21] M. Tzafetas *et al.*, “The intelligent knife (iKnife) and its intraoperative diagnostic advantage for the treatment of cervical disease,” vol. 117, no. 13, pp. 7338-7346, 2020.
- [22] M. J. E. r. o. m. d. Thill, “MarginProbe®: intraoperative margin assessment during breast conserving surgery by using radiofrequency spectroscopy,” vol. 10, no. 3, pp. 301-315, 2013.
- [23] J. M. Dixon *et al.*, “Intra-operative assessment of excised breast tumour margins using ClearEdge imaging device,” vol. 42, no. 12, pp. 1834-1840, 2016.
- [24] X. Li *et al.*, “Ultraviolet photoacoustic microscopy with tissue clearing for high-contrast histological imaging,” vol. 25, pp. 100313, 2022.
- [25] A. Qorbani *et al.*, “Microscopy with ultraviolet surface excitation (MUSE): A novel approach to real-time inexpensive slide-free dermatopathology,” vol. 45, no. 7, pp. 498-503, 2018.
- [26] K. Y. Garza *et al.*, “Intraoperative Evaluation of Breast Tissues During Breast Cancer Operations Using the MasSpec Pen,” vol. 7, no. 3, pp. e242684-e242684, 2024.
- [27] S. Mukherjee, *The emperor of all maladies: a biography of cancer*: Simon and Schuster, 2010.



# Acknowledgements

*“If I have seen further, it is by standing on the shoulders of giants.”*

*Isaac Newton*

As I am closing this chapter of my life, I would like to thank those who walked with me through the highs and lows, becoming a steady part of my life. This work wouldn't have been possible without each and every one of you. And while this may be goodbye for now, I hope it's only a pause—until our paths cross again.

**Jenny** and **Benno**, in a world where true mentors are rare, you became exactly that for me, and I'm deeply grateful for your wisdom and guidance. Thank you for your unwavering support, your patience, and the opportunity to learn and grow under your supervision. Saying goodbye to our collaboration has been one of the hardest parts of this journey. You have been wonderful supervisors, and I couldn't have asked for better mentors throughout my PhD journey.

**Jenny**, you're one of the few people I know who truly lives with purpose, always making a meaningful difference. You supported me every step of the way. During my PhD, I faced some challenging times regarding my personal life and the situation in my country. But you were always there, ready to listen. Whenever I came to you feeling tired and discouraged, you listened patiently and supported me with such care and compassion. Every time we talked, I left feeling calmer and more at ease.

**Benno**, every time we met, there was always something new to learn in your sentences; your wisdom spoke even between the lines. I learned a lot from you, and your steady support through the ups and downs, your belief in me, and your gentle encouragement gave me the freedom to explore, stay motivated, and grow throughout every stage of my work.

**Akash**, you were my first close colleague and friend at the start of my PhD journey. I learned a great deal from you, both about the project and the underlying concepts—and often looked to your work as a reference point. I truly enjoyed our conversations, and I'm grateful not only for your support as a colleague but also for your friendship along the way. **Merle**, I was truly happy when you joined our group—it meant having someone to explore new ideas with and grow alongside. I'm grateful that we had the chance to collaborate on different topics and learn from each other throughout. You've also been an

inspiring figure to me, especially in the way you embraced motherhood while continuing your PhD journey with such strength and grace.

My dear friends and colleagues at the MISIT lab—**Daniel, Tomas** (Lenssen), **Jan-Willem, Jonathan, Arjo, Nick** (van den Berg), **Robin, Tomas, Kim, Nick** (White), **Roos, Tonke, Marit, Hoda, Charlotte, and Linda**—you made my PhD journey truly enjoyable with your presence. Although COVID-19 kept us apart for a while, the time we shared in the office and beyond was always meaningful and fun. I truly appreciated the respectful and friendly atmosphere, and I always enjoyed our conversations—whether long or brief—as well as our lunches together. Thank you all for being such a supportive and memorable part of this chapter in my life.

I would like to extend my gratitude to the faculty members at TU Delft, **Prof. Amir Zadpoor, Prof. Paul Breedveld, DR. Tim Horeman-Franse, Prof. Maarten van der Elst, Dr. Lidy Fratila-Apachitei, and Dr. Julian Apachitei, and Prof. John van den Doppelsteen**, for their support and guidance throughout my journey. I would also like to thank the staff and secretaries at TU Delft for their kind support, assistance, and for keeping everything running smoothly behind the scenes.

I express my gratitude to all the peers, collaborators, and those who inspired me along the way. In particular, **Dr. Tessa van Ginhoven, Prof. Theo Ruers, Dr. Lisanne de Boer, Dr. Dinusha Veluponnarn, Dr. Marco Lai, and Dr. Hamed Abbasi**—thank you for your valuable insights and contributions that you brought to my work. **Pouya (Jelvehgaran) and Pierre (Ambrosini)**, it was a pleasure to collaborate with you. I am grateful for the insights I gained through our interactions.

I had the privilege of supervising and working with four amazing MSc students during their graduation projects—**Carlijn, Pieter, Pascal, and Rebecca**. Guiding your research and learning alongside you was a truly rewarding experience. Your contributions helped shape this thesis, and you were a great asset to my work.

I would also like to express my deepest gratitude to the friends who stood by me throughout this journey. To my friends in the Biomechanical Engineering Department, **Françoise, Mahya, Sébastien, Ingmar, Eline, Yageng, Costanza, Nazli, Niko, Jette, Lorenzo, Mahdiyeh, Vera, Kirsten, Esther, Vahid, Jiahui, Ebrahim, Shahram, Mauricio**, and all those with whom I shared meaningful moments, thank you for your friendship, your kindness, and the positive energy you brought into both work and life.

---

To my Alborz (Delft Iranian Student Association) buddies—**Nima, Sadaf, Ali, Amir, Bahareh, and Aram**—what we built together was truly special and deeply meaningful. It wasn’t easy, but it was full of purpose and heart, something we did for our country. Being part of it made the final year of my PhD so rich with experience, learning, and connection. I’m deeply grateful for the journey we shared and the unique friendship it created among us.

My dear colleagues and friends at **Sonian**—**Yan, Ashesh, Alwin, Joost, Chris, Yakup, Nienke, Daniel, Ad, Koen, Friso, and Raymond**—and all the others with whom I’ve had the pleasure of working: it has been great to work with you on such exciting projects over the past few years and thank you for encouraging me to push through and wrap up my thesis. My time at Sonian has taught me so much, and in many ways, it helped shape parts of my thesis.

To my friends who were there in the past years to create beautiful memories, share happy moments, or stay connected online—**Parisa and Mohsen, Arezoo and Saeid, Faezeh (Davari), Homa, Yasi, Mana and Naseh, Samira and Saleh, Aydin, , Mahya (Aminraya), Rik, Niloofar (Mosavat), Niloofar (Ghasemzaie), Aynaz, Shohreh, Niloofar and Bryan, Parisa and Rahim**, thank you for all the joy, warmth, and connection you brought into my life.

**Sadaf**, you came into my life recently, but it feels like I’ve known you for years. I’m sure you’ll be around for many decades to come! Thank you for being my super confident and loud Persian friend who never stops inspiring me, and for your amazing help with designing my thesis cover.

**Anahita**, thank you for supporting Khashayar and me through our immigration journey, your guidance and encouragement meant more than words can say.

**Tannaz**, you came into my life on a really tough day, but you’ve become one of the best parts of it. We’ve been through so many struggles over more than a decade, and honestly, I’m still surprised at how we’ve stayed so glued to each other. Thank you for all your support and for always cheering me up when I needed it most. You know the nickname we have for each other, right? That title will always be yours in my heart, forever.

**Hengameh**, you were my coffee partner throughout my PhD, and in so many ways, we were naturally connected. You brought joy and lightness to my journey, and you were

truly the cherry on top of my cupcake. **Hamid**, we argued a thousand times, but in the best way. After immigration, I deeply missed my day-to-day chats with my brothers, and you filled that space with warmth and energy. They say true friends are the ones you can talk to first and think later, and that's exactly what I had with both of you. **Hamid and Hengameh**, thank you, above all, for bringing **Homayoun** into our lives. From the very first news of his coming into our lives, the bitterness of life began to fade, and a new light of hope started to grow in our hearts. We've shared dark nights and some of the most joyful moments of our lives together, may our journey continue for decades to come.

To **Parisa Joon**, You had a heart that could hold the whole world in it, and I'm lucky to have felt its warmth. Your strength in fighting for your life taught me so much. I wish you could read this book and be there during my defense, as you promised—but the universe had other plans for you. Your memory will always stay with me.

To my loving and caring **DaiAli** and his wonderful family, **Nooshin joon, Paria, Sina, and Puria**, thank you for all the beautiful memories, your constant support, and the video calls that made the distance from home feel a little easier.

To all my **grandparents**, thank you for your unconditional love. Your memory will always live on in my heart. To **Mamani**, with whom I've shared a connection beyond words, you've inspired me in ways I can't fully explain, but deeply feel. Thank you for being the cool grandma in my life and for always giving me so much love.

To my **in-laws**, first of all, thank you for bringing Khashayar into this world, so I could fill my life with love. And second, thank you for your unconditional love and support throughout all these years.

**Isa**, you are a special part of my life. I've always had peace of mind knowing that you'll be there for me, no matter what. **Sobhan**, you've been with me since my very first cell came to existence, stay with me until the last. **Mohi**, thank you for completing our little gang and filling Sobhan's life with love. **Arash**, your calm nature and quiet wisdom have been a true inspiration. You've reminded me that strength doesn't always need to be loud. My dear siblings, thank you all for your ongoing support and for standing behind me like a mountain, strong and steady, through all these years.

To my lovely parents, **Maman** and **Baba**, you always believed in me, and that's the reason I am where I am today. The hardest thing I've ever done, and my biggest regret,

will always be leaving you behind. Now that I've become a mother myself, I understand that there is no love greater than a parent's love for their child. I would need pages to express everything I feel for you, so I'll keep it short: Thank you for everything.

**Dariush**, my sweet boy, becoming your mother has been the most beautiful, challenging, and emotional part of my life. You taught me to pause and truly enjoy every moment of life. I'm so grateful you joined me on this PhD journey.

**Khashayar**, my love, in a world that's always changing, in a life full of variables, you are my one constant. It wasn't easy—but we made it.



# List of publications

## A. Peer-reviewed journal publications

- **S. Azizian Amiri**, J. Dankelman, B.H.W. Hendriks, Enhancing Intraoperative Tissue Identification: Investigating a Smart Electrosurgical Knife's Functionality During Electrosurgery, IEEE Transactions on Biomedical Engineering, 2024.
- P. Ambrosini, **S. Azizian Amiri**, E. Zeestraten, T. van Ginhoven, R. Marroquim, T. van Walsum, 3D magnetic seed localization for augmented reality in surgery, International Journal of Computer Assisted Radiology and Surgery, 2024.
- **S. Azizian Amiri**, P. van Berckel, M. Lai, J. Dankelman, B.H.W. Hendriks, Tissue-mimicking phantom materials with tunable optical properties suitable for assessment of diffuse reflectance spectroscopy during electrosurgery, Biomedical Optics Express, 2022.
- **S. Azizian Amiri**, P. van Berckel, J. Dankelman, B.H.W. Hendriks, Electrosurgical knife equipped with diffused reflectance spectroscopy sensing for tumor margin detection during breast conserving surgery: a phantom study, Advanced Biomedical and Clinical Diagnostic and Surgical Guidance Systems, SPIE, 2021.
- **S. Azizian Amiri**, C.M. Van Gent, J. Dankelman, B.H.W. Hendriks, Intraoperative tumor margin assessment using diffuse reflectance spectroscopy: the effect of electrosurgery on tissue discrimination using ex vivo animal tissue models, Biomedical Optics Express, 2020.
- K. Modaresifar, **S. Azizian**, M. Ganjian, L. E. Fratila-Apachitei, A. A. Zadpoor, Bactericidal effects of nanopatterns: a systematic review, Acta Biomateriali, 2019.
- **S. Azizian**, A. Hadjizadeh, H. Niknejad, Chitosan-gelatin porous scaffold incorporated with Chitosan nanoparticles for growth factor delivery in tissue engineering, Carbohydrate polymers, 2018.
- **S. Azizian**, F. Khatami, K. Modaresifar, N. Mosaffa, H. Peirovi, L. Tayebi, S. Bahrami, H. Redl, H. Niknejad, Immunological compatibility status of placenta-

derived stem cells is mediated by scaffold 3D structure, *Artificial Cells, Nanomedicine, and Biotechnology*, 2018.

- F. A. Tehrani, **S. Azizian**, K. Modaresifar, H. Peirovi, H. Niknejad, The antibacterial effect of low temperature stored amnion on growth of *Escherichia coli*, *Staphylococcus aureus*, and *Pseudomonas aeruginosa*, *Journal of Babol University of Medical Sciences*, 2018.
- F. A. Tehrani, K. Modaresifar, **S. Azizian**, H. Niknejad, Induction of antimicrobial peptides secretion by IL-1 $\beta$  enhances human amniotic membrane for regenerative medicine, *Scientific Reports*, 2017.
- M. Mirmasoumi, **S. Azizian**, K. Modaresifar, H. Moravvej, H. Niknejad, Evaluation of the effect of amniotic membrane conditioned medium on the activity of Heat Shock protein 90 in cervical and breast cancer cells, *Journal of Advanced Medical and Biomedical Research*, 2017.
- K. Modaresifar, **S. Azizian**, M. Zolghadr, H. Moravvej, A. Ahmadiani, H. Niknejad, The effect of cryopreservation on anti-cancer activity of human amniotic membrane, *Cryobiology*, 2017.
- M. Zolghadr, K. Modaresifar, **S. Azizian**, H. Niknejad, Evaluating the effects of fresh and cryopreserved amniotic membrane on viability of HeLa and MDA-MB-231 cancer cells and angiogenesis of rat aorta ring, *Journal of Isfahan Medical School*, 35(424), 2017.
- K. Modaresifar, **S. Azizian**, A. Hadjizadeh, Nano/biomimetic tissue adhesives development: from research to clinical application, *Polymer Reviews*, 56(2), 2016.

## B. Selected conference presentations

- “Optical Knife for real-time tumor detection”, 33rd International Conference of the Society for Medical Innovation and Technology (SMIT), Oslo, Norway, March 30th-31st , 2022. *Awarded for the Best Oral Presentation*.
- “Smart electrosurgical knife for real-time tumor border detection during breast conserving surgery.” 8th Dutch Bio-Medical Engineering, Netherlands, January 28th -29th, 2021.

---

- “Electrosurgical knife equipped with diffused reflectance spectroscopy sensing for tumor margin detection during breast conserving surgery: a phantom study.” SPIE BiOS, California, USA, March 5th, 2021.
- “Smart electrosurgical knife for real-time tumor border detection during lumpectomy surgery on a realistic breast phantom” 32nd International Conference of the Society for Medical Innovation and Technology (SMIT), online conference, Chicago, USA, 26-28 September, 2020.
- “Smart Electrosurgical Knife with Diffuse Reflectance Spectroscopy for Real-time Oncological Guidance”, 31st International Conference of the Society for Medical Innovation and Technology (SMIT), Heilbronn, Germany, October 10th -11th, 2019.



# Curriculum Vitae

Sara Azizian Amiri was born on the 19th of March 1991 in Tehran, Iran. After receiving her high school diploma in Mathematics and Physics in 2009, she entered Tehran Polytechnic (Amirkabir University of Technology) to pursue a BSc in Biomedical Engineering with a specialization in Bioelectrical Engineering. She continued her education at Tehran Polytechnic with an MSc in Biomedical Engineering (Biomaterials) and graduated in 2017 with a thesis on the fabrication and characterization of tissue engineering scaffolds.

In September 2018, Sara started a new scientific chapter as a PhD Researcher at Delft University of Technology (TU Delft). Her research focused on developing a smart electrosurgical knife for intraoperative margin assessment under the supervision of Prof. Jenny Dankelman and Dr. Benno Hendriks at the MISIT Lab of TU Delft. Sara started working at Sonion as a Product Development Engineer in January 2023.

You can contact Sara via email at [sazizianamiri@gmail.com](mailto:sazizianamiri@gmail.com).



Cover image: Generated with Adobe Firefly and modified by the author.